University of California
Santa Barbara

Real-time measurement, analysis, and control in microfluidic systems for personalized medicine and designer materials

A dissertation submitted in partial satisfaction
of the requirements for the degree

Doctor of Philosophy

in

Materials

by

Peter L. Mage

Committee in charge:

Professor H. Tom Soh, Chair
Professor Francis J. Doyle III
Professor Craig Hawker
Professor Omar Saleh

March 2016

The Dissertation of Peter L. Mage is approved.

_____

Professor Francis J. Doyle III

_____

Professor Craig Hawker

_____

Professor Omar Saleh

_____

Professor H. Tom Soh, Committee Chair

December 2015

Real-time measurement, analysis, and control in microfluidic systems for personalized

medicine and designer materials

Copyright © 2016

by

Peter L. Mage

To my grandfather, Dr. David C. Ludington

Acknowledgements

I would first like to thank Prof. Tom Soh for giving me the opportunity to be involved in genuinely interesting and meaningful research over the course of my PhD. Over the past four years, I have been inspired by Tom's unique ability to bring together multiple fields of study toward solving compelling problems in medicine. His vision, guidance, and support made all of this work possible. I would also like to thank my committee members Prof. Frank Doyle, Prof. Craig Hawker, and Prof. Omar Saleh for their valuable time and advice over the course of my graduate studies. I am also indebted to the mentors and advisers that guided me in my early research experiences: Dr. Kenneth Hrdina at Corning Incorporated, Dr. Xidong Chen at Cedarville University, and Prof. Rüdiger Dieckmann at Cornell University.

My research at UCSB would have been impossible (and not much fun at all) without the numerous collaborators I had the privilege to work with for each project described in this dissertation. Dr. Scott Ferguson's endless enthusiasm, tenacity, and ingenuity turned the real-time feedback project from an interesting idea into a reality, and Dan Maliniak and Kyle Ploense provided invaluable time and expertise during our animal work. Prof. Kevin Plaxco and Prof. Tod Kippin provided valuable guidance, constant enthusiasm, and occasional pizza. Dr. Andrew Csordas first showed me how to use FACS and assisted on every FACS experiment described in this dissertation, in addition to providing insightful discussions. YongWoon Song (Sogang University, Korea) developed the software interface and algorithms for the SuperFACS image-based sorting project. Dr. Kuangwen Hsieh served as a key mentor, giving me the opportunity early in my PhD to help him finish his excellent work on contamination-resistant genetic detection. Other key collaborators for the research described in this work were Dr. Monte Radeke, Dr. Daniel Klinger, Dr. Allen Yang, Tyler Brown, Cynthia Wang, Diana Wu, Anusha Pusuluri, Nate Ogden, Dan Mamerow, Jacob Somerson, Dr. Netz Arroyo, and Abe Pressman. I would also like to thank the staff of the UCSB Animal Resource Center, specifically Dr. Manny Garcia, Ronni Wynn, and Amber Griffin, as well as the UCSB Nanofabrication Facility staff. Thank you to Dave Bothman for being a wealth of practical engineering advice and for making the UCSB Microfluidics Lab a reality. I am also indebted to Elizabeth Bagley and Lore Dobler for doing the huge amount of work required to keep the Soh lab running smoothly day-to-day. Finally, it was a joy to work with all of my Soh Lab compatriots over the years: Dr. Seung Soo Oh, Dr. Allen Yang, Dr. Kareem Ahmad, Dr. J.P. Wang, Dr. Gurpreet Sekhon, Dr. Qiang Gong, Dr. Jackie Alva, Dr. Hao Qu, Dr. Faye Walker, Faye Fong, Forrest McClellan, Tracy Chuong, Michael Gotrik, Chelsea Lyons, Brandon Wilson, Ola Jakobsson, Nupur Maheshwari, and David Hoggarth.

I was privileged to work, study, and enjoy Santa Barbara with fantastic colleagues, coworkers, and friends. To all of my friends in Materials, Mechanical Engineering, ECE, Bioengineering, Chemistry, BMSE, Linguistics, the climbing gym, and beyond —I can't imagine my time here without all of you. Thank you to my fantastic roommates at Coolbrook for making the house a true home throughout the years. Finally, I am fortunate beyond words to have had a supportive, loving family behind me the entire time.

Thank you to my grandparents for your active support and involvement throughout my entire education, and for being astounding role models, both personally and professionally. Thank you to my brother, for always being several notches cooler than me. And finally, thank you to my parents, who raised me in such a way that I have never doubted how much you loved me.

Curriculum Vitæ
Peter L. Mage

Education

2016	Ph.D. in Materials, University of California, Santa Barbara.
2011	B.S. in Physics, Cedarville University, *summa cum laude*.
2011	B.A. in Mathematics, Cedarville University, *summa cum laude*

Publications

1   P. Mage, B.S. Ferguson, D. Maliniak, K. Ploense, M. Eisenstein, T. Kippin, and H.T. Soh. "Closed-loop control of therapeutic molecules in live animals." *Manuscript in preparation.*

2   P. Mage, Y. Song, N. Ogden, D. Wu, M. Radeke, H.J. Lee, H.T. Soh. "High-throughput image-based cell sorting." *Manuscript in preparation.*

3   P. Mage, A. Csordas, D. Klinger, C. Wang, T. Brown, C. Hawker, H.T. Soh. "Shape-based sorting of synthetic microparticles with flow cytometry." *Manuscript in preparation.*

4   K. Hsieh*, P. Mage*, K.W. Plaxco, H.T. Soh. "Contamination-resistant real-time LAMP" *Manuscript in preparation.*

5   K. Hsieh*, P. Mage*, A. Csordas, M. Eisenstein, and H.T. Soh. "Simultaneous elimination of carryover contamination and detection of DNA with uracil-DNA-glycosylase-supplemented loop-mediated isothermal amplification (UDG-LAMP)." *Chemical Communications.* 2014 April 11; 50(28): 3747-9. doi: 10.1039/c4cc00540f. *authors contributed equally*

Conferences

1   P. Mage, A. Csordas, D. Klinger, C. Wang, T. Brown, C. Hawker, and H.T. Soh. "Precision sorting of designer microparticles based on size and shape using fluorescence-activated cell sorting (FACS)." Oral presentation at: 2015 Materials Research Society Fall Meeting; 2015 November 30 December 4; Boston, MA.

2   P. Mage, B.S. Ferguson, D. Maliniak, K. Ploense, T. Kippin, and H.T. Soh. "Real-time closed-loop control of circulating drug levels in live animals." Oral presentation at: 2014 Materials Research Society Fall Meeting; 2014 December 1-5; Boston, MA.

3	P. Mage, B.S. Ferguson, D. Maliniak, K. Ploense, T. Kippin, and H.T. Soh. "Real-time control of in vivo drug concentrations in live animals." Poster presented at: Biosensors 2014. 24th World Anniversary Congress on Biosensors; 2014 May 27-31; Melbourne, Australia.
4	P. Mage, K. Hsieh, A. Csordas, and H.T. Soh. "Staying on target: using nature's error-correcting tools to make molecular diagnostics more robust." Poster presented at: SLAS 2014. Third Annual Society for Laboratory Automation and Screening Conference and Exhibition; 2014 January 18-22; San Diego, CA.

Honors and Awards

2015	First Place, Falling Walls Lab, San Diego; Scholar, Falling Walls Lab Finals, Berlin *Worldwide and regional competitions for best breakthrough research talk*
2015	Best Scientific Presentation, UCSB Chemical Sciences Student Seminar Series 2014-2015
2015	Student Delegate, 2015 University of California Graduate Research Advocacy Day *Selected to present research to members of the California State Legislature*
2014	Best Student Presentation (Symposium D: Biosensors), 2014 Materials Research Society Fall Meeting
2013	Grand Prize Winner, UCSB Grad Slam *Campus-wide competition for best three-minute research talk for a general audience*
2012-2013	Honorable Mention, NSF Graduate Research Fellowship Program
2007 - 2011	Cedarville University Scholar Award *Nine recipients yearly; 75% tuition for four years*
2007 - 2011	Cedarville University Deans Honor List

Abstract

Real-time measurement, analysis, and control in microfluidic systems for personalized medicine and designer materials

by

Peter L. Mage

The field of microfluidics has enabled the development of powerful tools for analyzing and manipulating phenomena at the micro- and nano-scales, ranging from chemical analysis of biological samples to controlled synthesis of colloidal materials. In this dissertation we explore four unique platforms for real-time microfluidic measurement, analysis, and control systems with applications at the intersection of biomedicine and materials engineering. First, we show that a real-time biosensor can be used to perform closed-loop control of drug concentrations in the bloodstream of live animals. Second, we show that a commercially available cell-sorting instrument can be used to sort heterogeneous suspensions of synthetic microparticles based on shape using optical scattering measurements, resulting in monodisperse microparticle suspensions with well-defined morphology. Third, we report preliminary results for an image-based cell and microparticle sorter capable of sorting objects using two-dimensional high-speed microscopy and real-time image analysis. Finally, we report a contamination-resistant microfluidic assay for quantitative genetic detection based on real-time loop-mediated isothermal amplification, improving the robustness of point-of-care pathogen detection techniques.

Contents

List of Figures

Chapter 1

Introduction

1.1 Thesis goals and outline

The field of microfluidics has enabled the development of powerful tools for analyzing and manipulating phenomena at the micro- and nano-scales, ranging from chemical analysis of biological samples to controlled synthesis of colloidal materials. In this dissertation we explore several unique platforms for real-time measurement, signal processing, and control in microfluidic systems with applications at the intersection of biomedicine and materials engineering.

First, we describe a potential solution to the widespread clinical problem of patient-to-patient variability in drug response. Here we report a system capable of directly controlling circulating drug levels in the body in real-time. We achieve feedback-controlled drug infusion using a microfluidic real-time biosensor that can continuously measure a wide variety of drugs directly in the bloodstream. We demonstrate closed-loop control of circulating concentrations of the chemotherapy drug doxorubicin in live rabbits and rats, showing the ability to maintain virtually any concentration profile in the bloodstream as a function of time. We demonstrate our system's ability to regulate dosing across

1

multiple animals with varying pharmacokinetics, and within a single animal undergoing acute drug-drug interactions.

Second, we explore the unorthodox use of a microfluidic tool from the field of biology to enable the production of well-defined colloids with applications as functional materials. We show that a commercially available fluorescence-activated cell sorter (FACS) —a powerful and increasingly ubiquitous instrument used by cell biologists —can be repurposed to sort synthetic colloidal microparticles based on shape. Using stretched polystyrene microspheres as a model system, we demonstrate that microparticles exhibit unique shape-dependent optical scattering profiles in FACS. We then use these signature scattering profiles to sort and separate heterogeneous mixtures of particles with different morphologies (spheres, discs, and ellipsoids with varying aspect ratios) with high throughput (>1000 particles/s), purity, and yield, resulting in monodisperse suspensions of particles with well-defined shapes.

Third, we report preliminary results for a novel integrated microfluidic device capable of sorting particles and cells based on two-dimensional image features. Using high-speed microscopy and automated 2D image analysis, we demonstrate automated sorting of polymer microspheres and ellipsoids based on direct image detection of morphological features such as size and shape. We also demonstrate an algorithm for analyzing and sorting stem cell-derived retinal cells based on internal cell features.

Fourth and finally, we report an enzyme-based approach to eliminating carryover contamination in real-time genetic pathogen detection assays based on loop-mediated isothermal amplification (LAMP). Our contamination-resistant real-time LAMP assay combines enzymatic elimination of carryover contaminants with DNA-intercalation-based real-time amplification monitoring. Uracil-tagged carryover contaminants are degraded with the uracil-DNA-glycosylase enzyme, and target amplification is monitored electrochemically in an integrated microfluidic device, enabling rapid discrimination of DNA

samples with different amounts of pathogen DNA even in the presence of substantial carryover contamination. This represents a critical enabling step toward robust, quantitative real-time pathogen detection.

Because of the wide variety of topics covered in this dissertation, rather than using unified "Introduction," "Theoretical Framework," and "Conclusion" chapters, each chapter has self-contained introductory material describing the motivation, prior work, relevant theoretical discussions, and proposed future work related to that chapter's topic.

Chapter 2

Closed-Loop Control of Circulating Drug Concentrations in Live Animals

2.1   Introduction

Although personalized medicine is typically perceived through the lens of matching patients with the appropriate drugs, achieving the ideal dose for a given individual is also critical. The optimal dose should maximize the efficacy of treatment while minimizing the risk of harmful toxicity, a target range that is exceedingly narrow for many widely-used drugs including chemotherapeutics [1,2], immunosuppressants [3,4], antipsychotics [5], anticoagulants [6], aminoglycoside antibiotics [5], and others. Achieving this optimal dose for drugs with narrow therapeutic windows is a major challenge for clinicians because of the profound variability with which patients respond to medication, both from patient-to-patient and within the same patient over time [2,7]. Response to drug varies due to differences in both pharmacokinetics (PK) —describing how the

body affects drug concentration over time through absorption, distribution, metabolism, and excretion —and pharmacodynamics (PD), describing how the drug's physiological effect depends on effect-site concentration [8]. This variability in drug response, which arises from a combination of genetic, physiological, and environmental factors [2], can result in harmful under- or over-dosing, making it one of the principal problems in drug development and clinical pharmacology.

To counter this unpredictability, clinicians presently use a variety of imperfect tools that attempt to tailor drug dose to a specific patient's needs. Most commonly, dosage is selected by comparing the patient's physiological parameters —such as sex, weight, or body surface area (BSA) [9] —to dosage tables based on population-averaged PK/PD data for that drug [10]. Unsurprisingly, this simple approach fails to account for a large proportion of the clinically meaningful PK/PD variability observed across patients [1, 10, 11]. The recent explosion of "precision medicine" has encouraged the use of more sophisticated personalization methods such as pharmacogenetic profiling, which identifies specific polymorphisms in the individual's genome that are known to cause changes in drug metabolism, clearance, or susceptibility [12]. Unfortunately, pharmacogenetic approaches are time- and resource-intensive to develop and administer, making them useful for only a select few drugs [13] and severely limiting their clinical deployment [14]. Moreover, methods such as pharmacogenetics and BSA-normalization do not correct for physiological changes that may occur within a single patient over time, potentially altering their response to drug over the course of treatment (*e.g.*, exposure-dependent pharmacokinetics, or comorbidities affecting ADME such as hepatic or renal failure, or lowered serum albumin levels). To account for both patient-to-patient and intrapatient variability, some drugs are accompanied by therapeutic dose monitoring (TDM), which entails tracking the plasma levels of drugs and metabolites after initial drug administration, and adjusting subsequent dosing accordingly based on PK/PD models [15, 16].

Although TDM is the current standard of care for many narrow-therapeutic-index drugs, it is constrained by slow, delayed measurements of plasma concentration at single time-points, giving limited PK/PD insights and preventing responsive dose adjustment for fast-acting drugs or rapidly changing disease states.

A much more powerful approach to personalized dosing would be to control the circulating level of drugs in the body in a closed-loop manner. Toward this end, a small number of closed-loop dosing systems have been developed since the 1950s for niche applications involving narrow-therapeutic-index drugs, namely anesthesia delivery during surgery [17–19] and cardiovascular drug infusion for maintenance of hemodynamics [20–22]. More recently, the artificial pancreas platform has been used to regulate blood glucose levels in diabetic patients through feedback-controlled insulin infusion [23]. Although these systems have shown improved therapeutic outcomes compared to manual human-guided dosing [21, 24, 25], they cannot be applied to the vast majority of other drugs. This is because all existing closed-loop dosing platforms perform control based on readily measurable physiological effects of the drug (*e.g.* depth of anesthesia, blood pressure, or blood glucose levels for the respective systems mentioned above) which act as feedback for adjusting drug delivery. Many other drugs with narrow therapeutic windows, such as chemotherapeutics or antipsychotics, have effects that cannot be measured quickly enough to adjust infusion, preventing this sort of feedback control from being implemented. A more general approach would be to control drug levels directly based on measurements of *in vivo* drug concentration; however, the vast majority of drugs cannot be measured in the body in real-time, making such an approach impossible to date. Nevertheless, such control, if possible, would eliminate a major source of pharmacokinetic uncertainty, namely, how drug infusion is related to the drug's concentration-time profile in the bloodstream.

Here we report the first medical technology that directly controls the circulating con-
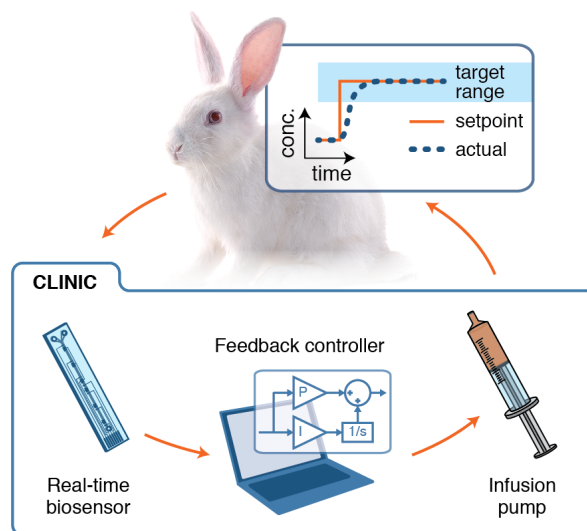
Figure 2.1: Scheme for closed-loop control of *in vivo* drug levels with CLINIC. As a programmable infusion pump injects drug into the animal, the bloodstream is sampled continuously by our real-time biosensor. The resulting electrochemical measurements of drug concentration are analyzed by our control algorithm, which calculates the infusion rate needed to maintain the desired circulating drug set-point at any given time, and automatically adjusts the infusion rate accordingly.

centrations of drugs in the body in real-time. Our Closed-Loop Infusion for *In vivo* Control (CLINIC) system (Figure 2.1) continuously regulates the circulating concentration of intravenous drugs by measuring the drug's concentration in the bloodstream with a real-time aptamer-based biosensor [26] and using a feedback control algorithm to continuously modulate the rate of drug infusion, achieving the desired *in vivo* concentration at minute time-scales. Crucially, in contrast to existing closed-loop dosing systems, CLINIC controls infusion based on direct measurement of drug concentration *in vivo*, rather than depending on delayed physiological indicators of drug activity as proxies for drug concentration. This enables rapid and responsive control of drug plasma levels from patient to patient and within the same patient over time, with no need for complex pharmacokinetic modeling [10]. As a proof of concept, we used CLINIC to perform continuous closed-loop dosing of the chemotherapy drug doxorubicin (DOX) in live rabbits and rats, demon-

strating the capacity to achieve and maintain a wide range of concentration set-points in the bloodstream as a function of time. We chose to use DOX because, while widely used in cancer treatment, it is difficult to dose successfully in the clinic. The therapeutic outcome of DOX treatment is closely tied to its plasma concentration profile over the course of treatment, with efficacy dependent on total plasma exposure [27] and cardiotoxic side effects correlated with peak plasma levels reached during drug infusion [28–31]. However, DOX exhibits a very narrow therapeutic dose window [32], and patient-to-patient pharmacokinetic response to DOX varies widely [27, 33, 34] even when normalized to body surface area (BSA) —the current clinical standard for DOX dosing [11, 35]. Suboptimal DOX dosing has been linked to a significant reduction in survival among breast cancer patients [36].

2.2 Background and Theoretical Framework

2.2.1 Sensing requirements for feedback control

Performing feedback control of drug concentration requires a sensor that quantitatively measures drug levels in the body **continuously** (*e.g.*, with high time resolution relative to the relevant physiological processes, usually in the minute-range but potentially shorter for applications such as neurological stimulation) and **in real-time** (*e.g.*, with minimal measurement lag relative to the aforementioned time scales). A practical consequence of these requirements is that measurements must be performed directly in the biological medium of interest, since traditional benchtop processing steps such as centrifugation or affinity purification would introduce unacceptably long processing times. Unfortunately, the majority of existing bioanalysis assays —such as the widely-used enzyme-linked immunosorbent assay, or ELISA —provide only single time-point

measurements [26]. This is because they require time-consuming sample processing and analysis procedures, typically with multiple incubation and wash steps, making them impossible to use for real-time feedback control. Toward enabling continuous measurements, other biosensor formats interrogate changes in physical properties of surface-bound receptors (typically antibodies) exposed to a sample flow containing analyte, providing a continuous measurement of analyte concentration; examples of such an approach are surface plasmon resonance and quartz crystal microbalance systems [37]. However, these systems are cripplingly susceptible to nonspecific binding, making measurements all but impossible in complex media such as blood [37]. This leaves a small number of analyte-specific tools for measuring molecular species *in vivo* both continuously and in real-time, namely, the pulse oximeter for monitoring blood oxygen content and oxidase-based electrochemical sensors for blood glucose, lactate, glutamate, and cholesterol [37]. Unfortunately, each of these examples is based on a target-specific enzyme interaction that allows a quantitative readout of target concentration; such an enzymatic approach is not generalizable to the vast majority of other analytes of interest.

Toward developing a general biosensor that could be used for *in vivo* feedback control, the Soh lab developed a sensor platform capable of real-time, continuous molecular measurement directly in complex biological media. This platform combines three key technologies. First, **electrochemical aptamer probes** provide instantaneous, reversible, and quantitative readout of target molecule concentration. These probes are target-specific and can be generated for a wide variety of molecular targets [38]. Second, a **kinetic differential measurement** scheme is utilized to eliminate baseline drift, removing the need for baseline correction during post-processing and thus allowing truly real-time measurements. Third, measurement is performed in a **microfluidic blood sampling device** that enables analyte measurements directly in whole blood drawn directly from the bloodstream [26]. We will briefly discuss each of these technologies in

turn.

2.2.2   Real-time biosensing with electrochemical aptamer probes

Electrochemical aptamer probes are a class of reagentless probes for real-time molecular detection [39–41]. Aptamers are synthetic single-stranded DNA or RNA oligonucleotides (generally < 100 bases long) that are generated through an *in vitro* evolution process to bind specifically to some molecular target. Electrochemical aptamer probes are based on a subset of aptamers whose three-dimensional conformation changes significantly upon target binding. This target-induced structure change can be measured by probing the change in proximity that occurs between the 3' and 5' ends of the oligonucleotide strand. This can be performed optically in solution, using a fluorophore-quencher or FRET pair on the 3' and 5' ends of the strand. Alternatively, the conformation change can be probed electrochemically using surface-tethered aptamers, wherein one end of the aptamer is anchored to an electrode and the other end is tagged with a redox-active reporter which transfers electrons to the electrode through oxidation and reduction at the appropriate potentials. We measure this redox activity using square-wave voltammetry (SWV), which minimizes the effects of capacitive charging so that only faradaic electron transfer due to redox reactions is measured. The amplitude of this faradaic current is highly dependent on the average distance from the redox probe to the electrode surface; hence, SWV interrogation of the redox-tagged surface-bound aptamer provides an instantaneous electrical readout of target-binding-induced aptamer conformation changes.

Electrochemical aptamer-based sensing enables sensitive, specific, and real-time measurement of target molecule concentrations. The performance of an electrochemical aptamer for doxorubicin [26,42] is shown in Figure 2.2. First, the aptamer probe is sensitive to DOX over a range of concentrations covering therapeutic levels in humans [43]; binding
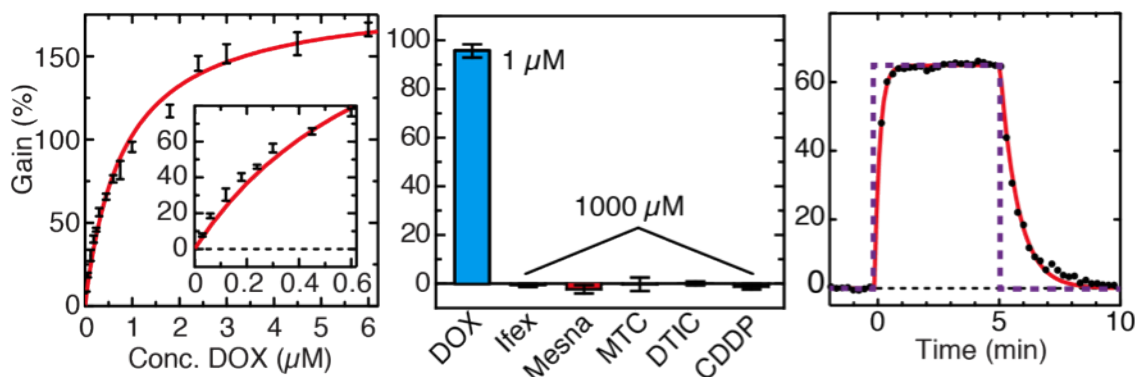
Figure 2.2: Characterization of electrochemical DOX aptamer performance, showing probe response to target (left), probe specificity (center), and probe binding kinetics (right). Adapted with permission from [26].

follows a Langmuir isotherm with an apparent dissociation constant of ~ 0.8 nM in buffer (Fig. 2.2, left). Second, the electrochemical DOX aptamer is highly specific to DOX over other chemotherapy drugs commonly administered with DOX (Figure 2.2, center), although it is known to bind to the structurally similar anthracycline daunorubicin [42]. Third, the DOX aptamer exhibits reversible drug binding with rapid binding kinetics as shown in response to a 5-minute pulse of 600 nM DOX (Figure 2.2, right). The aptamer exhibits an on-rate of $k_{on} = 3.0 \pm 0.35$ mM^{-1} min^{-1} and an off-rate of $k_{off} = 1.35 \pm 0.05$ min^{-1}, enabling real-time readout of DOX pharmacokinetics [26].

2.2.3 Drift-free concentration tracking through kinetic differential measurement

To avoid signal drift over time, our real-time biosensor employs a differential measurement scheme that self-corrects for baseline drift. Unlike differential measurements that rely on a separate "reference" sensor, we perform differential measurements using a single probe. We do this by exploiting the fact that the DOX aptamer, like many other structure-switching electrochemical aptamers [38], can be used both as a "signal-on"
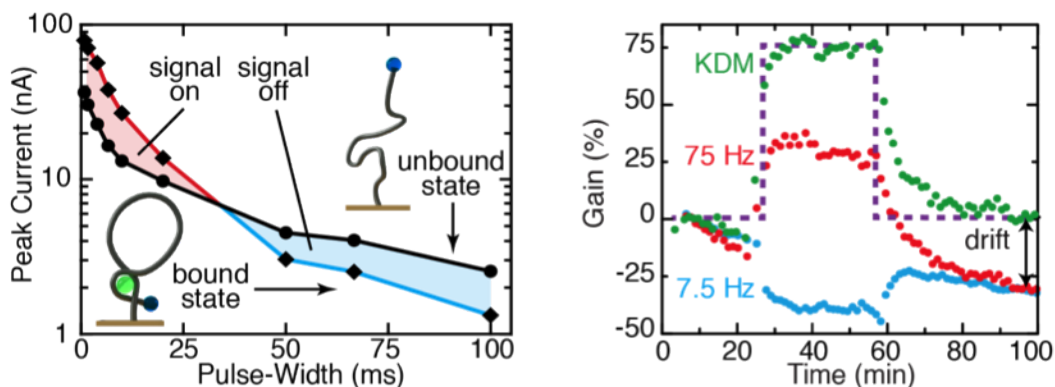
Figure 2.3: The signaling polarity of the DOX aptamer is dependent on SWV pulse width ($1/2f$, where f is SWV frequency) (*left*). By measuring at both signal-on and signal-off SWV frequencies, a drift-free differential measurement can be obtained (*right*). Adapted with permission from [26].

probe, where redox current increases with target binding, and as a "signal-off" probes, where current decreases with target binding. The signaling magnitude and polarity of electrochemical aptamers is dependent on the SWV interrogation frequency (the inverse of the square-wave pulse width) [38], an effect arising from the kinetics of charge depletion for surface-bound redox probes [38]. The DOX probe exhibits a signal-on response in the presence of DOX when interrogated at high ($\geq$100Hz) frequencies, and a signal-off response to DOX at low (leq10Hz) frequencies (Figure 2.3, left). By interrogating the probe at both signal-on and signal-off SWV frequencies, we obtain two current traces with opposite target response polarity but similar baseline drift; subtracting these two signals eliminates baseline drift while maintaining response to target. This kinetic differential measurement (KDM) strategy has two key benefits: (1) reduced baseline drift and (2) enhanced signal magnitude relative to "common mode" noise (Figure 2.3, right) [26].
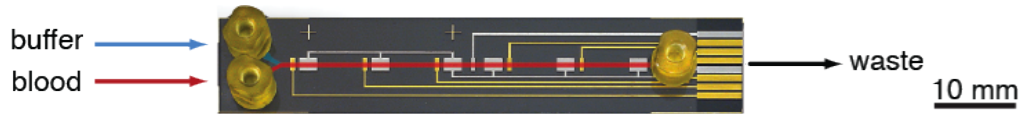
(a) Diagram of the microfluidic real-time biosensor chip.
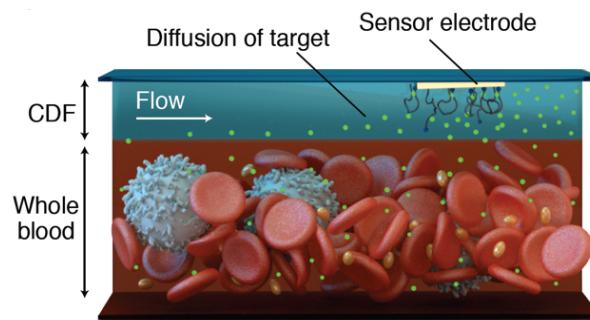
(b) Cross-sectional schematic of the CDF (components not to scale).
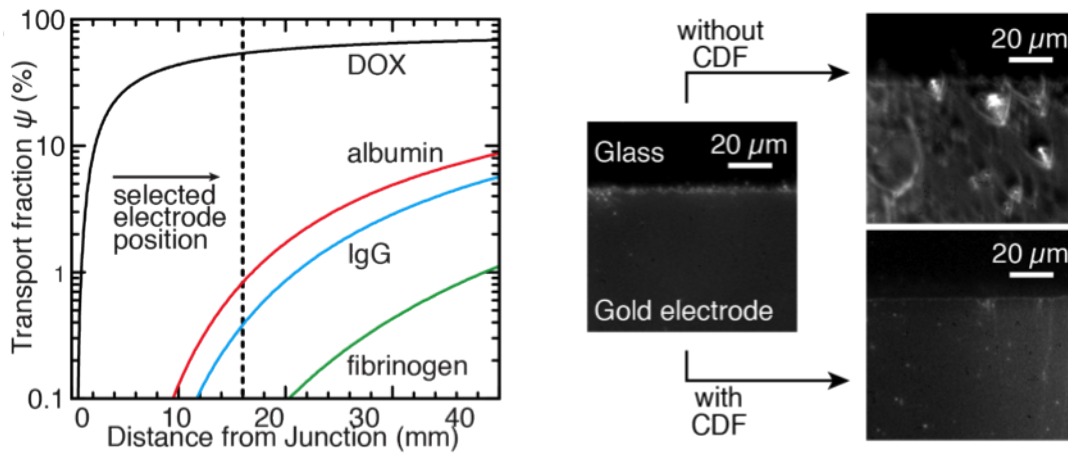
(c) Simulated molecular transport across the CDF (left) and optical micrographs of electrode fouling with or without the CDF (right).

Figure 2.4: Schematic and characterization of the continuous diffusion filter (CDF). Adapted with permission from [26].

2.2.4   Microfluidic continuous diffusion filter for long-term measurement directly in whole blood

The third key technology in our real-time biosensor is a microfluidic continuous diffusion filter (CDF) which allows target measurement directly in whole blood. The CDF prevents occlusion of the aptamer-functionalized electrode surface by blood cells, platelets, and other high-molecular-weight interferents (such as serum albumin and clotting factors) present in blood; such biofouling occurs rapidly on unprotected electrodes placed directly in blood, causing significant baseline drift and diminished signal in response to target. The CDF is formed within a microfluidic channel in the biosensor chip (Figure 2.4a) via vertical laminar flow stacking of a saline buffer layer (blue) on top a continuous flow of blood (red), which may be drawn directly from a sample tube or from an animal or patient's bloodstream through a catheter (Figure 2.4b). The buffer layer serves as a liquid-phase low-pass molecular weight filter between blood and the aptamer-functionalized sensor electrode (located at the top of the channel). Low-molecular-weight species, such as DOX, rapidly diffuse through the CDF and are detected at the electrode, while only a small fraction of high-molecular-weight blood interferents are able to diffuse to the electrode (finite element simulations of molecular transport across the CDF shown in Figure 2.4c, left). Furthermore, the CDF prevents physical occlusion of the sensor by blood cells and platelets (Figure 2.4c, right) [26].

In summary, our real-time biosensor achieves continuous quantitative measurements of DOX directly in whole blood by integrating (i) electrochemical aptamer probes interrogated with (ii) a kinetic differential measurement scheme in (iii) a microfluidic blood sampling device that utilizes continuous diffusion filtering.

14

2.3   Results and Discussion

2.3.1   CLINIC system overview

The CLINIC system controls *in vivo* drug concentrations by integrating our real-time biosensor (RTB), a dose controller, and an intravenous infusion pump into a closed feedback loop (Figure 2.1) which operates as follows. The RTB continuously samples circulating blood directly from the bloodstream, transmitting drug concentration measurements to the controller for real-time analysis. Based on the measured drug level, the controller uses a feedback control algorithm to calculate the infusion rate required to reach and maintain the desired concentration set-point. The controller then modulates the infusion pump's rate of drug administration accordingly. In this way, CLINIC continuously adjusts drug infusion in response to measurements of drug concentration, enabling it to control a wide range of concentration profiles in the bloodstream over time with sub-minute resolution.

2.3.2   Real-time biosensing

The RTB achieves continuous, virtually lag-free measurements of *in vivo* DOX levels by integrating electrochemical aptamer-based detection with a microfluidic blood sampling system, described in detail above and in [26]. For this work, we dramatically reduced the measurement lag of the RTB compared to our previous work by implementing two key improvements. First, we wrote a real-time electrochemical analysis script in MATLAB that converts raw electrochemical measurements to DOX concentration values on-the-fly. Second, we optimized fluidic transport of blood from the animal to the device by using short (< 10 cm) lengths of small-bore (~ 200 μm ID) microcapillary tubing between a venous catheter and the chip. Implementing these improvements enabled the controller
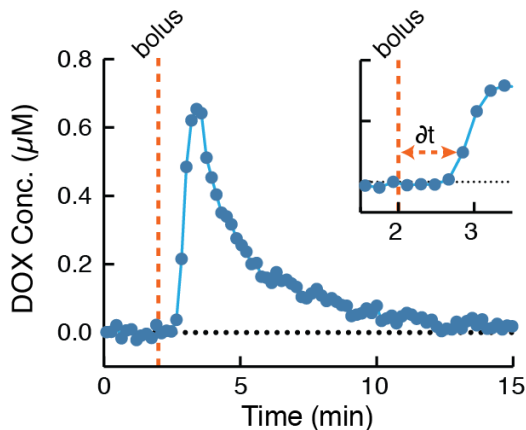
Figure 2.5: Real-time biosensing of DOX in live rabbits. CLINIC's real-time biosensor has a point-to-point time resolution of 11 seconds and a measurement lag (δt) of 0.8 min (inset). Vertical dotted line indicates time of DOX bolus injection (0.93 mg/m^2).

to respond to DOX fluctuations *in vivo* within 40 seconds (*e.g.*, sensor-to-pump lag) with a sampling interval of 11 seconds (Figure 2.5). Importantly, the aptamer probes in our biosensor can readily be exchanged to measure a variety of target molecules [26], thereby enabling CLINIC to potentially control a broad range of small-molecule drugs.

2.3.3   Feedback controller design, modeling, and tuning

CLINIC modulates the rate of drug infusion using a proportional-integral (PI) feedback control algorithm to achieve responsive, robust control of drug levels in the bloodstream. The PI algorithm calculates infusion pump output U at any given time t as a weighted sum of one term proportional (P) to the present error $e(t)$ (difference between measured and set-point concentrations) and another term proportional to the integral (I) of the total error over time:

$$U(t) = k_p e(t) + k_i \int_0^t e(\tau)d\tau \tag{2.1}$$

16

Controller performance is wholly determined by two parameters, the proportional and integral gains k_p and k_i, which determine the relative weight of the P and I terms. Although physiological closed-loop control systems such as the artificial pancreas typically rely on complex model-based control algorithms (*e.g.*, [44]), we selected the PI feedback algorithm for its simplicity and ability to respond rapidly to set-point changes while achieving stable set-point tracking even in the presence of sensor lag.

To design and optimize the controller, we first modeled the entire feedback loop *in silico* as a linear time-invariant system (Figure 2.6a). The central element of the system model is a pharmacokinetic expression that empirically describes how DOX levels in the bloodstream change over time, using a biphasic exponential decay model with a constant dilution volume [45]. The model captures the dynamics of the rapid distribution (α) and elimination (β) phases of DOX plasma clearance in rabbits ($t_{1/2}^{\alpha} = 2$ min, $t_{1/2}^{\beta} = 18$ min) while ignoring the γ-phase ($t_{1/2}^{\gamma} = 15$ hr) [45], which is too slow to meaningfully affect our system. To build this model, we experimentally determined average α- and β-phase half-lives of DOX by using the RTB to measure circulating DOX levels in rabbits during DOX administration. We then empirically tuned the model so that it accurately simulated *in vivo* concentrations for a given DOX input (Figure 2.6b). We finally added components to the system model describing the temporal behavior of the RTB, the infusion pump, and the feedback controller, allowing us to simulate operation of the entire CLINIC system.

To ensure that simulations using our system model matched real-world CLINIC behavior, we measured the step response of the controller using a simple, untuned proportional (P only, $k_i = 0$) control algorithm. When deployed in a rabbit, the controller had the underdamped response typical of untuned P control for a second-order process, with a steady-state error due to sensor lag (Figure 2.6c, top). Simulating the same control algorithm with our system model yielded quantitatively similar control behavior (Figure 2.6c, bottom), validating the model's usefulness for describing CLINIC performance.

(a) Feedback loop model

(b) Pharmacokinetic simulation

(c) Controller simulation performance

(d) Result of PI controller tuning
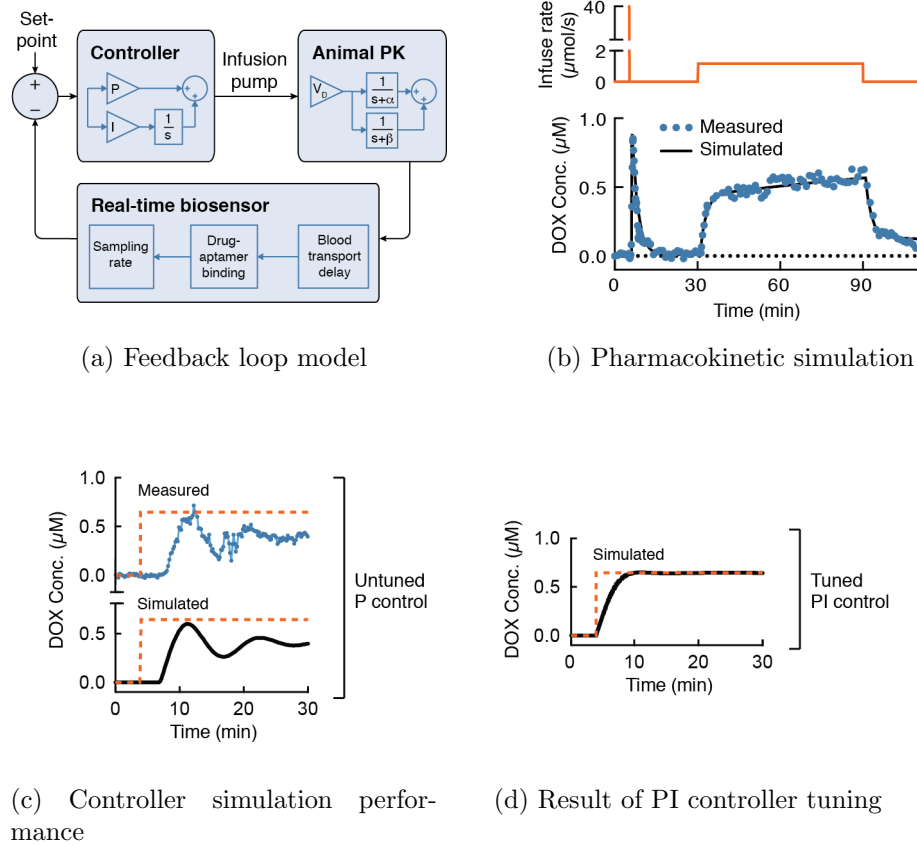
Figure 2.6: Simulation and tuning of CLINIC feedback controller

Using our system model, we tested the performance of different PI control settings to determine an optimal controller design for CLINIC use *in vivo*. Notably, simulations showed that controller performance was sufficient without a derivative (D) term (used in the more common PID algorithm), which would have made the system more susceptible to high-frequency noise in the RTB measurements. We used our system model and controller tuning software to determine an optimal set of k_p and k_i parameters that balanced controller response time and stability (Figure 2.6d). We then utilized these gain parameters in CLINIC's tuned PI controller.

2.3.4   Closed-loop control of DOX levels in live rabbits and rats

Using this algorithm, CLINIC achieved stable, prolonged feedback control of circulating levels of DOX in live, conscious New Zealand White rabbits (Figure 2.7). CLINIC responded rapidly to changes in set-point (Figure 2.7, top), reaching 95% of the set-point concentration in 7.52.9 minutes from the start of controlled infusion, and remained within 20% of the set-point throughout the experiment (details in supplementary online text). We note that these set-points, representative of typical therapeutic concentrations for humans, are maintained for durations similar to those used during clinical infusions [43]. We also used CLINIC to maintain other dosing profiles as a function of time, including concentration ramp-ups and ramp-downs and arbitrary combinations of ramps and holds (Figure 2.7, middle and bottom, respectively). In all instances, CLINIC maintained stable feedback control with minimal oscillation.

To demonstrate our platform's capacity for robust closed-loop feedback control across species, we used CLINIC in live, anesthetized Sprague-Dawley rats. We chose this species because rats have DOX plasma clearance times markedly different from the rabbit model but nearly identical to those of humans [43,46–48]. We obtained optimal P and I control parameters for infusion in rats by adapting our in silico model to account for this cross-species difference in pharmacokinetics. By adjusting only the P and I control parameters without further modifications to the CLINIC system, we achieved feedback performance in rats that was essentially equivalent to that demonstrated in rabbits, reaching 95% of the concentration set-point within 8.6 min (Figure 2.8). Of note, DOX plasma levels returned to an elevated baseline concentration at the end of infusion because DOX has considerably longer α- and β-phase circulation half-lives in rats.

Figure 2.7: Closed-loop feedback control of doxorubicin. CLINIC accurately maintains *in vivo* drug concentrations (blue dots) at the desired set point (orange line) with a response time of 5-10 minutes in live, conscious New Zealand White rabbits. A variety of concentration profiles can be realized continuously as a function of time. Start of control indicated by orange arrows.
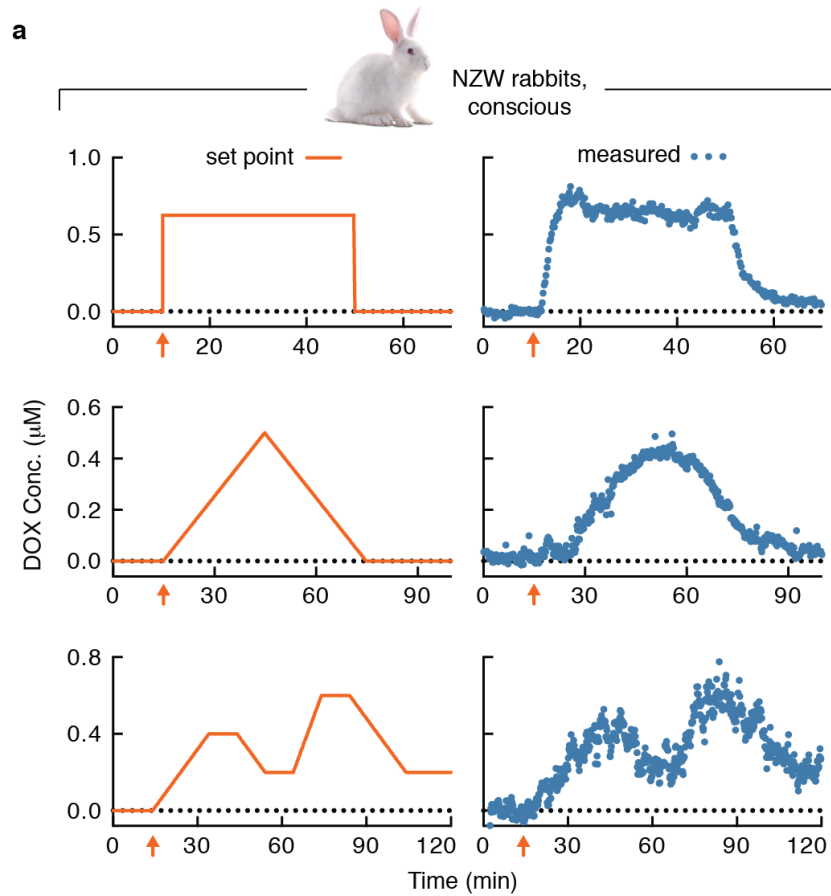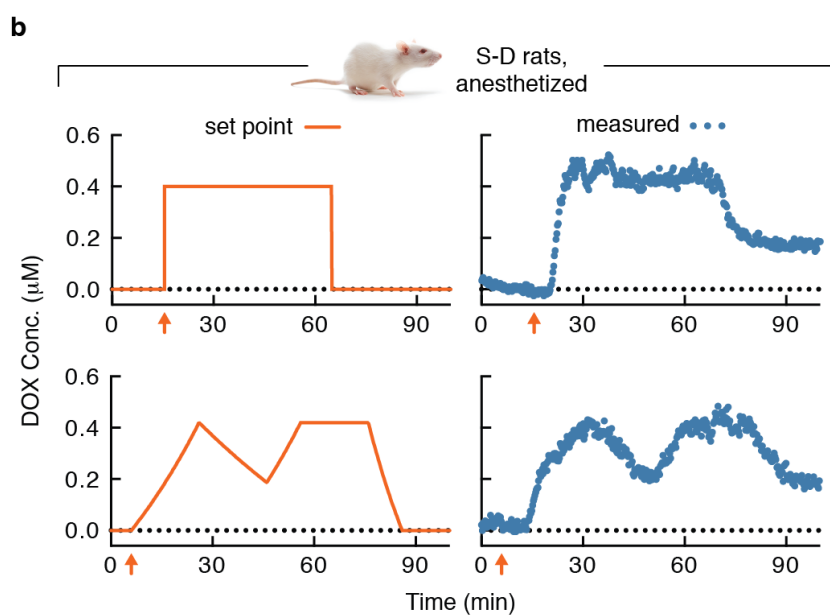
Figure 2.8: Closed-loop feedback control of doxorubicin. CLINIC accurately maintains *in vivo* drug concentrations (blue dots) at the desired set point (orange line) with a response time of 5-10 minutes in live, anesthetized Sprague-Dawley rats. A variety of concentration profiles can be realized continuously as a function of time. Start of control indicated by orange arrows.

2.3.5   Compensating for animal-to-animal pharmacokinetic variability with CLINIC

We next applied CLINIC to the widespread clinical problem of pharmacokinetic variability in chemotherapy dosing, both across individuals and in the same individual over time [2, 7]. First, we employed CLINIC to perform real-time dose compensation for individual differences in DOX pharmacokinetics across multiple rabbits. To quantify the extent of pharmacokinetic variability, we administered three different rabbits with an identical BSA-adjusted dose of DOX. We performed a constant one-hour infusion regimen at 11.5 mg/m^2/hr, equivalent to typical human therapeutic dosing [35]. Real-time biosensor measurements revealed pronounced variability in plasma levels of DOX across individual rabbits during this "open-loop" dosing, even though the dosing regimens were normalized by BSA —the current clinical standard (Figure 2.9A). Only Rabbit 3 achieved the desired plasma level and stayed in the target concentration range for 80% of the infusion period (white windows in Figure 2.9A). The steady-state values of plasma DOX levels in Rabbits 1 and 2 were either below or above the desired level, staying within the target concentration range for only 31% and 12% of the infusion period, respectively (Figure 2.9A). The biosensor was independently calibrated immediately prior to each infusion, ensuring that differences in measured plasma levels were due to pharmacokinetics and not sensor variability.

In contrast to open-loop dosing, CLINIC automatically and dynamically adjusted infusion rates to achieve the desired DOX concentration (Figure 2.9B). Under closed-loop infusion control, Rabbits 1 and 2 remained within the target concentration range 81% and 96% of the time, respectively (Figure 2.9C), a significant improvement compared to open-loop BSA-adjusted dosing. Importantly, the same P and I control parameters were used for all animals, demonstrating that CLINIC can optimize therapeutic dosing
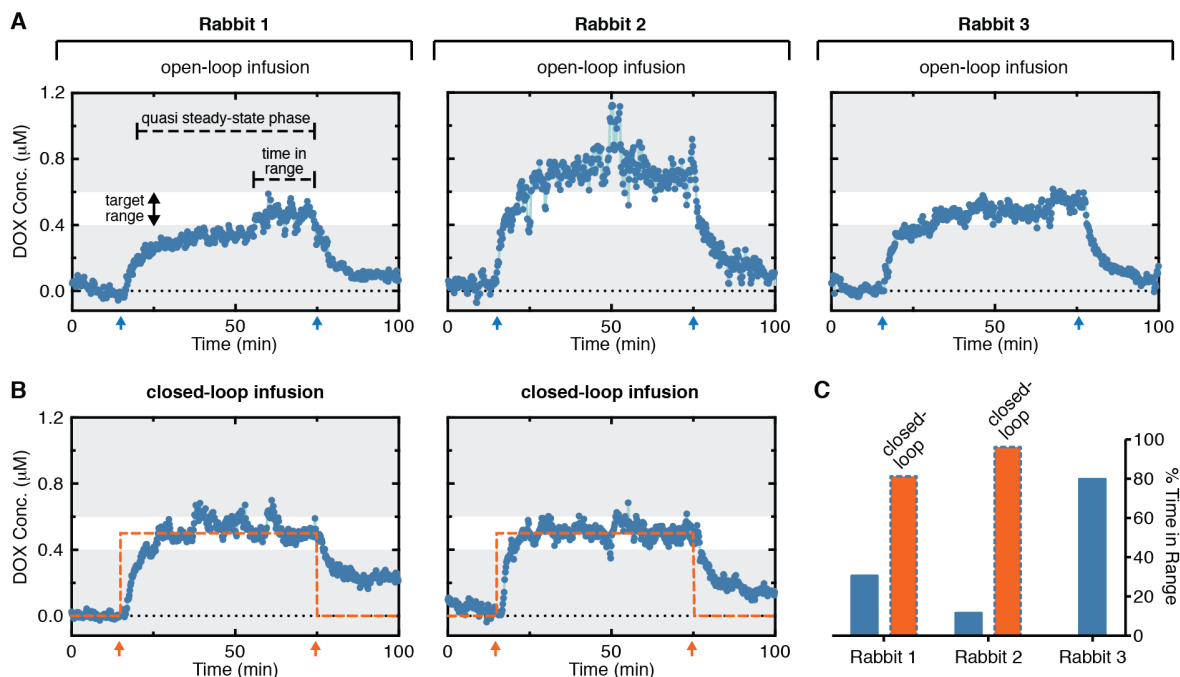
Figure 2.9: CLINIC maintains stable plasma drug levels in animals with varying pharmacokinetics. (A) Pharmacokinetic variability results in distinctly different DOX plasma concentrations in three different animals over the course of infusion; only Rabbit 3 remains in the target range (white band) for the majority of the infusion period (demarcated by arrows). (B) CLINIC maintains the desired DOX plasma concentration set-point (orange dashed line) in both Rabbits 1 and 2. (C) Closed-loop feedback control results in a far greater proportion of time spent in the target concentration range, independent of pharmacokinetic variability.

without a priori knowledge of an individual's pharmacokinetics.

2.3.6　Correcting for acute drug-drug interactions with CLINIC

Finally, we used CLINIC to automatically optimize dosing during acute drug-drug interactions, which can cause rapid, unpredictable, and dangerous pharmacokinetic disturbances [7]. Specifically, we co-administered the widely-used chemotherapy drug cisplatin (CDDP) to rabbits prior to DOX infusion [49], leading to a drug interaction known to significantly extend DOX's plasma half-life and increase its peak plasma concentration, presumably due to CDDP-induced changes in liver and kidney function [50].

This interaction was clearly evident when we compared the plasma concentration pro-
file of DOX during DOX-only infusion (Figure 2.10A, left) to that of DOX during
DOX+CDDP co-administration in the same rabbit one week later (Figure 2.10A, cen-
ter). Co-administration led to significantly higher plasma levels of DOX over the course
of infusion, even though an identical BSA-adjusted DOX dose was given in both cases.
This open-loop dosing resulted in only 34% time in the target concentration range dur-
ing co-administration, dramatically worse than the 95% for DOX infusion alone (Figure
2.10A, right). In contrast, closed-loop dosing with CLINIC automatically maintained
DOX at precisely the desired concentration in the presence of CDDP (Figure 2.10B),
increasing percent time in the target concentration range to 97% during DOX+CDDP
co-administration.

2.3.7   Discussion and Conclusion

In this work, we have demonstrated CLINIC's potential to enable precise therapies
through closed-loop control of drug concentrations *in vivo*. As a proof-of-concept, we di-
rectly controlled the circulating levels of the chemotherapeutic agent DOX in live rabbits
and rats, with the ability to reach and maintain a broad range of concentration set-points
in the bloodstream as a function of time. Our system automatically adapts drug delivery
to individual animals' physiology, compensating in real-time for pharmacokinetic vari-
ability and drug-drug interactions to enable optimal therapeutic dosing. We have shown
that CLINIC can be readily adapted to regulate DOX levels in two mammalian species
with dramatically different physiological and pharmacokinetic characteristics. Based on
this, we believe that CLINIC could be successfully adapted to control DOX levels in hu-
mans with minimal changes to the system. Moreover, because CLINIC uses a real-time
biosensor based on aptamers that can readily be exchanged to measure other molecular
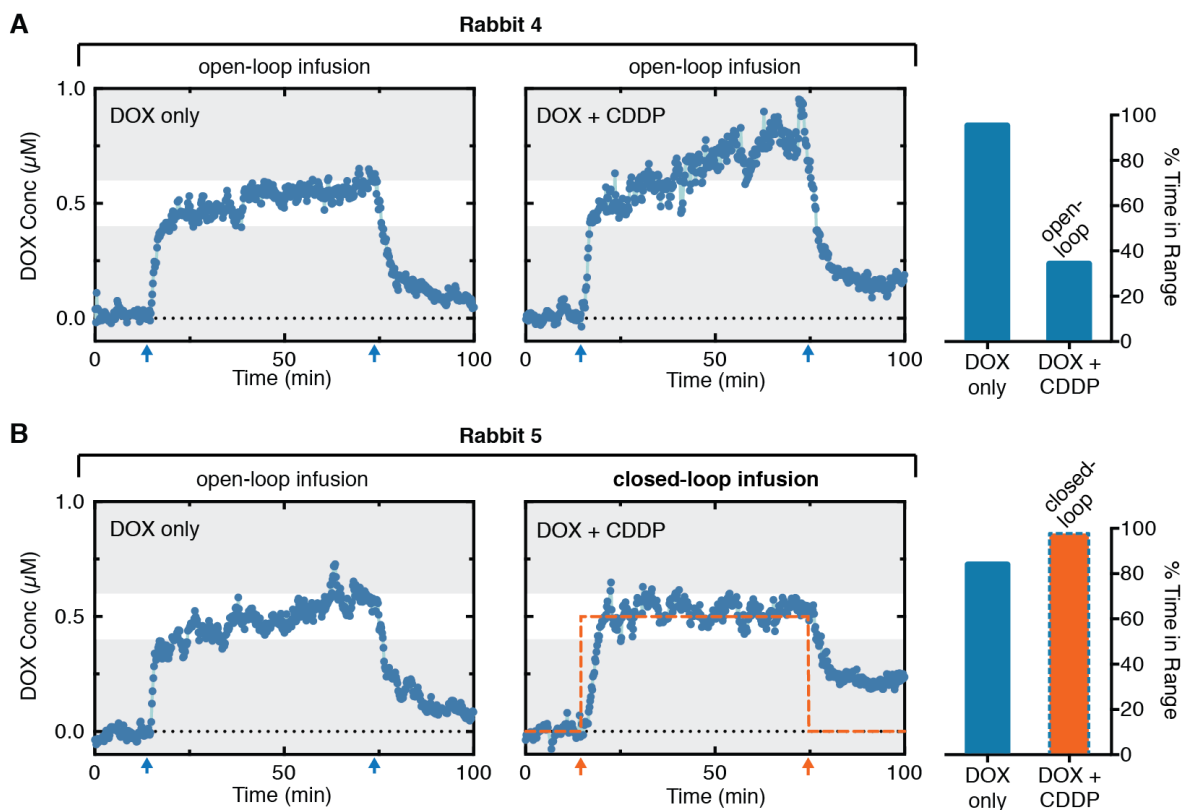
Figure 2.10: CLINIC automatically corrects for acute drug-drug interactions. (A) DOX pharmacokinetics in rabbits (left) is markedly altered by co-administration of cisplatin (CDDP; middle), resulting in plasma concentrations that exceed the target range (right). (B) CLINIC automatically corrects for this effect and achieves a stable set-point (middle), maintaining the target concentration for the entire duration of infusion (right). Arrows indicate start and end of DOX infusion.

targets [26], it offers a generalizable platform for closed-loop control of a broad range of drugs in living subjects.

Although this work demonstrates CLINIC's therapeutic potential, there are a number of limitations to the results of this study. We did not perform therapeutic endpoint studies to determine whether our dosing approach improves efficacy or diminishes toxicity in an animal model over the course of long-term treatment. However, because the efficacy and toxicity of DOX are known to be correlated with plasma drug levels, such studies are a logical next step. We also note that our system only regulates levels of unbound

drug in the circulatory compartment, which, while clinically relevant for DOX and many other drugs, neglects the fact that there is often a complex pharmacokinetic relationship between plasma levels and effect-site concentration (and therefore efficacy) for other drugs.

There are several areas of improvement possible for the CLINIC platform. First, CLINIC can actively increase circulating DOX levels by accelerating infusion, but concentration decreases are dependent on the animal's physiological drug-clearance rate. However, for drugs with injectable reversal agents [51, 52], our system could readily be adapted to perform active reduction of effective drug concentrations. Second, CLINIC is presently designed to control infusion based on measurements of unbound drug molecules in the blood. However, for many drugs, levels of metabolites and protein-bound drug are also important indicators of pharmacological activity. Future versions of our system could integrate multiple aptamer probes to control infusion based on simultaneous measurement of not only free drug but also its metabolites and drug-protein complexes. Third, we demonstrated stable drug control over multiple-hour time periods, suitable for acute clinical applications. Previously, similar aptamer probes have been shown to be chemically stable for several weeks [53]. Based on these results, we anticipate that control with CLINIC could be extended over much longer time frames to enable treatment of chronic conditions.

2.4   Conclusion

Our results controlling DOX suggest that CLINIC would be particularly useful for drugs with narrow therapeutic windows, a major class of therapeutics with unresolved challenges for dosing due to patient-to-patient variability [5]. Another potentially powerful application of CLINIC is for dosing drugs with fast pharmacokinetics and pharmaco-

dynamics (e.g., propofol [54]), especially in situations where patient physiology changes rapidly and unpredictably (e.g., during surgery or trauma care). In its present configuration, CLINIC is an *ex vivo* system that would be well-suited for use in clinical settings, but future iterations of our platform could incorporate implantable sensors [55] and infusion devices [56] to enable continuous, minimally-invasive dose regulation for chronic conditions. We envision that future versions of CLINIC could eventually be used to control drug delivery not only based on measurement of *in vivo* drug levels, but also by continuously monitoring the body's response to drug in the form of circulating biomarkers. This ability would be a first step toward direct closed-loop regulation of physiological processes, potentially making CLINIC a powerful tool for next-generation precision medicine.

2.5   Experimental Methods

2.5.1   Study design

The objectives of our study were twofold. First, we sought to demonstrate the proof-of-concept capability to directly control circulating concentrations of therapeutic agents in live New Zealand White rabbits and live Sprague-Dawley rats, using DOX as a model. Second, we aimed to use this closed-loop control to adjust DOX administration in rabbits to automatically compensate for pharmacokinetic variability, both from animal-to-animal and within the same animal due to drug-drug interactions. To evaluate controller performance, DOX concentrations were measured directly in the animals' bloodstream using our real-time biosensor. To evaluate pharmacokinetic variability, we measured the circulating concentration of DOX in multiple rabbits undergoing identical BSA-adjusted infusions of DOX, as well as in rabbits undergoing identical infusions of DOX before and

after CDDP administration (details in Results). For pharmacokinetic variability experiments, rabbits were used instead of rats because drug monitoring and control can be performed as a non-terminal survival procedure in rabbits, enabling comparison across multiple experiments in the same animal. Individual animals were selected randomly for each experiment. Blinding was not applicable to this study. Replication conditions for each experiment are defined and described in Results.

2.5.2 Sensor fabrication

Sensor fabrication (Figure 2.11) is described in detail in [26]. Briefly, two Borofloat glass wafers (University Wafer Inc.), each 10 cm in diameter and 700 μm thick, were cleaned by sequential immersion in acetone, isopropanol and deionized water. Gold working electrodes and platinum counter and reference electrodes were photolithographically patterned onto the top wafer and electron beamevaporated (VES 2550, Temescal) to a thickness of 300 nm on 20-nm titanium adhesion layers. Subsequently, a CNC mill (Flashcut CNC) with 1.1-mm diamond bit (Triple Ripple, Abrasive Technology) was used to drill fluidic vias (two inlets, one outlet) in the top wafer. The top and bottom wafers were diced (DISCO) into device pieces with dimensions of 58 mm 11 mm and 53 mm 11 mm, respectively. The 500-μm-wide top (buffer) and bottom (blood) flow channels were both cut from a 250-μm-thick polydimethylsiloxane (PDMS) sheet (BISCO Silicones, Rogers Corp.) using a laser cutter (Speedy 100, Trotec).

The blood channel was first bonded to the diced bottom glass substrate via 10-s corona-ozone treatment (BD-20AC, Electro-Technic Products Inc.). The buffer channel was then bonded to the blood channel. To prevent clot formation in the sensor chips during exposure to whole blood, a commercial heparin surface-coating kit [57,58] (Harvard Apparatus) was used to treat the inner surface of the assembled blood and buffer

MEDIC Sensor Chip Assembly

top view

Glass cover
700 µm thick

PDMS blood channel
250 µm thick

PDMS buffer channel
250 µm thick

Gold measurement electrodes
0.3 µm thick

Platinum reference/counter electrodes
0.3 µm thick

Glass electrode substrate with fluid vias
700 µm thick

10 mm

exploded view

deposit electrodes

bond channels to cover glass

bond to electrode glass

electrical connection pads

fluid waste outlet

5 mm

measurement electrodes
(central rectangles)

flow direction

MEDIC sensor

buffer inlet

blood inlet

Figure 2.11: Exploded diagram of MEDIC chip components and assembly.

channels as well as the bottom glass substrate. Meanwhile, electrochemical cleaning of the gold working electrodes was performed on the top electrode glass substrate following the protocol in [26]. The heparin-treated bottom glass substrate-blood channel-buffer channel assembly and cleaned top electrode glass substrate were both ozone treated in a UV ozone cleaner (Novascan) for 10 minutes and subsequently bonded. Alignment was performed under a standard inverted microscope via an xyzq stage (Newport Corp.) and vacuum chuck. Fluidic port connectors were glued onto the device with 5-min epoxy (ITW Devcon), readying the chip for probe immobilization.

2.5.3   Aptamer probe preparation and immobilization

The DOX-specific aptamer probe was synthesized by Biosearch Technologies with the following sequence: 5'-(HS-(CH2)6)3-ACCATCTGTGTAAGGGGTAAGGGGTGGT-MB-3'. Design rationale for this probe is described in detail in [26]. Notably, we replaced the mono-thiol linker used in [26] with a more robust trithiol anchor, extending the sensor lifetime and thermal stability compared to mono-thiol linkers alone [53]. The probe was tri-thiolated at the 5' end to facilitate self-assembly on the gold working electrodes, and conjugated with a methylene blue (MB) redox label at the 3' end to enable target binding-induced charge transfer modulation. Probe preparation and immobilization were otherwise identical to [26].

2.5.4   Fluidic instrumentation

All flow to and from CLINIC was controlled via syringe pumps (PhD 2000, Harvard Apparatus). The sensor chip input port was connected to a 24-gauge intravenous catheter (Beckton Dickinson) for animal studies via a 15-cm length of 0.20-mm inner diameter (ID) fluorinated ethylene propylene (FEP) tubing (IDEX). A 10-ml syringe loaded with 1 SSC

supplemented with 100 U/ml heparin was placed in a pump and connected to the buffer port on the sensor chip via a 30-cm length of Tygon tubing (Saint-Gobain Performance Plastics), with 1.78-mm outer diameter (OD) and 1.02-mm ID. The sensor chip output port was connected to a primed 20-ml "waste" syringe placed in a second pump via 1.65-mm OD and 0.762-mm ID silicone tubing (NewAge Industries). To monitor flow rates in real-time, we used a flow meter (Mitos Flow Rate Sensor, Dolomite Microfluidics) in-line between the output port and waste syringe pump. The buffer layer was established by engaging the buffer pump at 0.331 ml/hour. Simultaneously, sample was continuously drawn into the device by engaging the waste pump at 1.654 ml/hour.

2.5.5   Voltammetry

Electrochemical measurements were conducted with a PalmSens EmStat2 USB-connected potentiostat (Palm Instruments BV). Sensor chips were connected to the potentiostat via an 8-pin card edge connector. Square-wave voltammetry (SWV) scans were performed at interrogation frequencies of 10 Hz and 100 Hz, with a square-wave pulse amplitude of 30 mV and potential steps of 10 and 1 mV, respectively, resulting in an average scan period of 5.5 s. A potential range of 160 mV to -240 mV (vs. Pt) was used to capture the full redox current peak of MB. In cases where reference potential drift occurred, the scan range was adjusted until the MB redox peak occurred in the center of the range.

2.5.6   Sensor characterization and calibration

To convert electrochemical current measurements to concentration values, we obtained a dose-response curve by exposing the sensor chip to DOX (LC Laboratories) concentrations ranging from 250 nM to 8 μM in rabbit whole blood flowing at the rate described above. At each concentration, the sensor signal was permitted to equilibrate

and the subsequent 50 points were averaged as the reported values. A dose-response curve was obtained by fitting signal gain to a Langmuir isotherm, resulting in an apparent dissociation constant (K_d) of 1.682 ± 0.030 μM (mean$\pm$SD).

2.5.7   Real-time analysis and control program

To facilitate real-time measurement, dose calculation, and pump control, a custom analysis and control program was written in MATLAB (Mathworks). The program performs three key functions: (1) retrieving and converting raw electrochemical data from the potentiostat into concentration measurements, (2) calculating the necessary infusion rate —based on these measurements and the user-input concentration set-point —using a discrete implementation of the parallel PI control algorithm, and (3) communicating with the infusion pump to adjust the drug infusion rate. In addition, the program provides a real-time graphical plotting interface enabling the user to observe concentration measurements and controller output.

2.5.8   Control system modeling, simulation & tuning

The dynamical systems simulation software Simulink (Mathworks) was used to model the feedback loop comprising the animal pharmacokinetics, real-time biosensor, and PI controller, as well as all relevant transport and signal processing delays in the system 2.12. Pharmacokinetics of DOX in rabbits and rats was modeled as a biphasic concentration decay with decay constants α and β and respective weighting constants W_α and W_β:

$$\frac{C(t)}{C_0} = W_\alpha \exp(-\alpha t) + W_\beta \exp(-\beta t) \tag{2.2}$$

where $C(t)$ is drug concentration in the bloodstream at time t and C_0 is the initial concentration. A constant blood dilution volume was incorporated to account for dilution
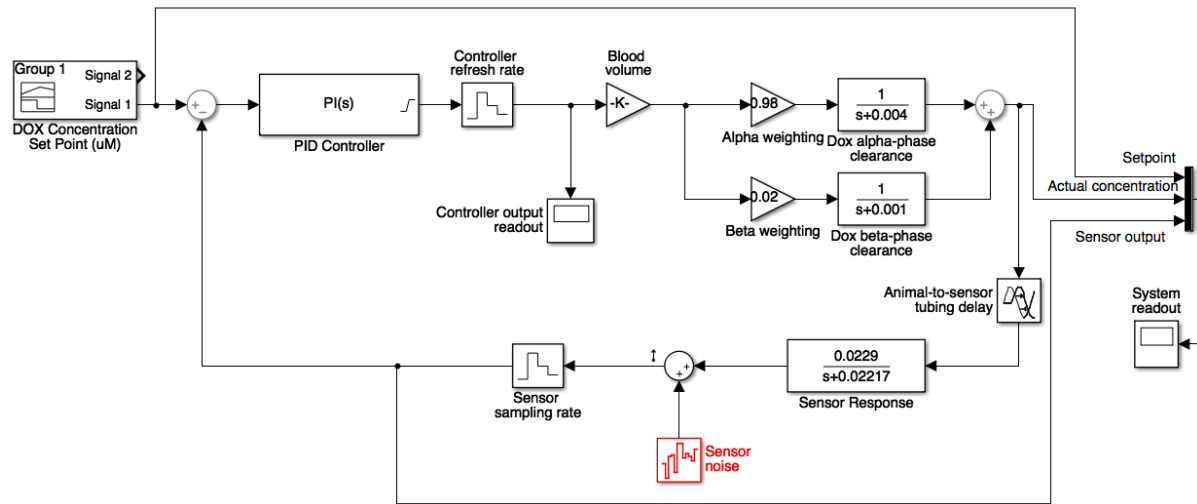
Figure 2.12: Simulink model used for controller tuning.

of drug in the bloodstream. To model the real-time biosensor, we incorporated terms to account for the fluidic transport delay from the animal's bloodstream to the sensor, as well as the sensor's fixed sampling rate and its temporal response to changes in DOX concentration (fitted from sensor step-response data).

With the full feedback loop described in the model, we used Simulink's built-in PID tuning functionality to determine P and I parameters that maximized response time (rapid rise time) and minimized both overshoot and oscillation about the set-point. To account for uncertainties in the model, it was necessary to determine a correction factor so that these in silico tuned parameters would result in similar control performance when implemented *in vivo*. To do this, we performed *in vivo* feedback control using specific sets of "training" control parameters. We then manually adjusted the control parameters in the Simulink model until we found a set of P and I parameters that resulted in in silico performance that was quantitatively similar to the *in vivo* training data. We compared the *in vivo* control parameters to the in silico control parameters that produced the same observed performance, and subsequently calculated a correction factor. The final control

33

algorithm was implemented in a discrete form, with a fixed sampling time of 5 seconds.

2.5.9   Live animal studies

Live animal studies using New Zealand White rabbits were performed according to our protocol titled "*In vivo* small molecule detection (rabbits)," approved by the University of California, Santa Barbara (UCSB) Institutional Animal Care and Use Committee (IACUC) and assigned protocol number 859. All rabbits used in this work were male (n=14) and purchased from Charles River Laboratories. Rabbits were acclimated to the facility for at least one week after arrival and observed for abnormal health conditions before experiments were performed. Rabbits were treated with aspirin (CVS) (10 mg/kg P.O. cumulative) and clopidogrel (Henry Schein) (10 mg/kg P.O. cumulative) over the four days leading up to and including the day of the experiment to prevent formation of clots in the catheter, tubing, and chip during blood draws [59]. Immediately prior to the experiment, rabbits were partially sedated with acepromazine (Henry Schein) (1 mg/kg I.M.). Rabbits were placed in rabbit restrainers to prevent them from damaging or disturbing their catheters. To facilitate catheter access to the marginal ear veins, the rabbits' ears were shaved and a topical anesthetic (EMLA lidocaine/prilocaine cream, MedVet) was applied 15 minutes prior to catheterization. Cannulation was performed in the marginal vein of both ears (Insyte Autoguard Shielded IV Catheter, Becton-Dickinson). To prevent clot formation in the catheters, tubing, and sensor chip, an initial dose of 300 IU/kg heparin (SavMart) was injected via each catheter, followed by hourly doses of 150 IU/kg administered via the right ear vein catheter. Following catheterization and heparin administration, 2.5 mL of blood was drawn for sensor calibration. After calibration, capillary tubing (0.008" ID FEP tubing, IDEX) was inserted into the left ear vein catheter and blood was drawn continuously from the catheter through the sensor chip

at a rate of 1.323 ml/hr. Bolus injections, continuous infusions, and controlled infusions of DOX (LC Laboratories) and CDDP (Western Medical Supply) were all administered via the right ear vein catheter. Continuous and controlled infusions were injected by a syringe pump from a 5 ml syringe connected to the catheter via a 30-cm length of polytetrafluoroethylene (PTFE) tubing (Cole-Parmer), with 0.76-mm OD and 0.30-mm ID. The catheters for infusion and measurement were placed such that injected drug passed through the heart and into circulation before being withdrawn for measurement. At the conclusion of experiments, rabbits were euthanized via intravenous Euthasol (Virbac Animal Health) injection if they received CDDP during the experiment and/or their cumulative dose of DOX over all experiments exceeded 1 mg/kg; otherwise, they were returned to their cages for recovery and use in subsequent experiments.

Live animal studies using Sprague-Dawley rats were performed under our "*In vivo small molecule detection*" protocol, similarly approved by the UCSB IACUC and assigned protocol number 824. All rats used in this work were male (n=6) and purchased from Charles River Laboratories. The rat surgical setup protocol, including anesthetization, catheter placement, heparin administration, DOX bolus administration, and euthanasia, is identical to the protocol described in [26], with the addition that controlled infusion of DOX was administered into the right jugular vein catheter using the same setup described above for rabbits.

Controlled infusions of DOX for rats and rabbits were given at a concentration of 2 mM. For continuous open-loop infusion experiments in rabbits, DOX concentration and volume infusion rate were selected such that all rabbits would receive the same BSA-adjusted dose at an infusion rate of 11.5 mg/m^2/hr for exactly one hour. Body surface

area (BSA, m^2) for dose normalization was calculated according to the equation

$$BSA = \frac{9.9 \times \mathrm{m}^{2/3}}{10,000} \tag{2.3}$$

as described in [60], where m is the animal's mass in grams. CDDP, when administered, was given to a total dose of 4 mg/kg as a single bolus injection at a concentration of 1 mg/ml, 2-4 hours prior to DOX infusion.

2.5.10   Step-response rise time calculation and infusion analysis

To quantify controller performance *in vivo*, we calculated the time required for the controller to reach 95% of its set-point step response, with starting time defined as when feedback control was activated. For these calculations, sensor data was smoothed to minimize the impact of high-frequency noise. Step response profiles from four separate rabbit experiments were analyzed to calculate mean and standard deviation.

In each rabbit, the plasma concentration profile was characterized by a rapid rise (drug distribution phase, 1-5 minutes after start of infusion), a subsequent slow linear increase in concentration over the remainder of the infusion time (quasi-steady state, qSS, 6-60 minutes after start of infusion), and a rapid decrease to a slightly elevated baseline concentration after cessation of infusion. We defined the target concentration range as a window whose center is the average concentration during the qSS phase across all three animals and whose width is the average standard deviation of the qSS-phase concentration in a single animal. We calculated this target range to be 0.5 μM $\pm$ 0.1 μM. Percent time in target range was defined as the percentage of the qSS phase during which the measured *in vivo* concentration was within the target concentration range.

Chapter 3

Shape-based Separation of Synthetic Microparticles with a Fluorescence-Activated Cell Sorter

3.1   Introduction

[1] Synthetic microparticles are a major class of "designer" materials [61], with applications ranging from drug delivery [62–64] and biomedical imaging [65] to directed assembly of photonic colloids [66] and other functional materials [67–69]. Successful synthesis of well-defined colloidal materials for these applications requires tight control over not only their chemical properties, but also their physical attributes such as microparticle size and shape [63] As a result, a large body of work related to controlled polymer microparticle synthesis has been developed over the past several decades. Complex schemes relying on droplet microfluidics [70–73], flow lithographic methods [71, 74, 75], and electrohydrody-

---

[1]At the date of compiling this thesis, March 17, 2016, this work is still in progress. The contents are thus presented as preliminary results.

namic inkjet printing [76] have been developed, all boasting various degrees of control over particle shape, size, and composition. However, such approaches are typically difficult to develop and operate, requiring specialized devices for any desired particle, preventing their adoption on a large scale. In addition, these approaches are often severely limited by their particle generation throughput. On the other end of the synthesis spectrum are facile and scalable methods such as emulsification in bulk mixtures undergoing mechanical agitation or sonication [61] or precipitation reactions [77]; however, these approaches typically result in heterogeneous, polydisperse colloidal mixtures [61,67,78]. Aggregation-based methods, wherein clusters of monodisperse "building blocks" can be formed through templated [67] or surface-tension driven [79] self-assembly, can also be used to generate clusters of specific size and shape, but similarly require downstream purification.

The heterogeneity resulting from scalable, facile synthesis approaches can be overcome with downstream fractionation and sorting, enabling purified populations of microparticles with specific desired morphologies to be obtained. A wide range of techniques for separating particles based on their physical characteristics have been reported [80]. The majority of these rely on intrinsic differences in the particles' density, volume, or hydrodynamic radius to achieve separation. Density gradient centrifugation is the most common example of such an approach. Isopycnic centrifugation can be used to enrich particles based on their density, but is incapable of separating particles based on shape. Rate-zonal centrifugation can separate particles based on mass differences, but can only achieve shape-based separation for radically differing shapes (*e.g.*, needles vs. spheres), with poor resolving power and purity [81,82]. More sophisticated electrophoretic techniques have also been used to separate nanoparticles based on shape (hydrodynamic radius) [83], but require coating the particles with charged functional groups. Specialized microfluidic tools have also been developed to sort particles based on their hydrodynamic or electroki-

netic properties. Deterministic lateral displacement (DLD) can separate particles based on volume and shape (exploiting the fact that particles with different shape have different hydrodynamic radii), but are physically limited to very low flow rates and consequently have very low particle throughput [84, 85]. Other techniques utilizing electrokinetics are similarly throughput- and purity-limited [86]. Faster systems using inertial microfluidics have been shown to passively separate isovolumetric ellipsoid particles based on aspect ratio [87] at comparatively high fluid volume throughput (40-80 μl/min, demonstrated with 1×10^6 particles/ml), but with limited separation purity and separation resolution. More troublingly, the use of such microfluidic systems defeats the purpose of using facile and scalable emulsion-based synthesis techniques, because they require specialized microfluidic devices that are difficult to design and operate, they necessitate extensive tuning and even redesign depending on the target particle system to be sorted, and have poor scalability. There is thus a pressing need for a separation strategy that can achieve high sorting sensitivity and purity, while preserving the scalability and throughput of facile emulsion-based synthesis.

Toward this end, we report the first shape-based sorting of synthetic microparticles using elastic optical scattering measurements performed in a commercial fluorescence-activated cell sorter (FACS). Optical scattering is a well-characterized method for non-destructive characterization of synthetic microparticle morphology [88–90], but has never been used for active sorting or enrichment of microparticles. FACS is used heavily in the fields of molecular and cell biology[2] to sort single particles (typically cells) based on optical characteristics such as scattering or fluorescence [91]. Commercial FACS instruments can typically handle objects ranging from ∼500 nm to > 100 μm in size, and are capable of particle throughput in excess of 10,000 particles/s [91], with newer instruments

---

[2]For reference, the number of papers in the NCBI Pubmed database containing the phrases "flourescence-activated cell sorting" or "flow cytometer" has exceeded 10,000 every year from 2010 to 2015.
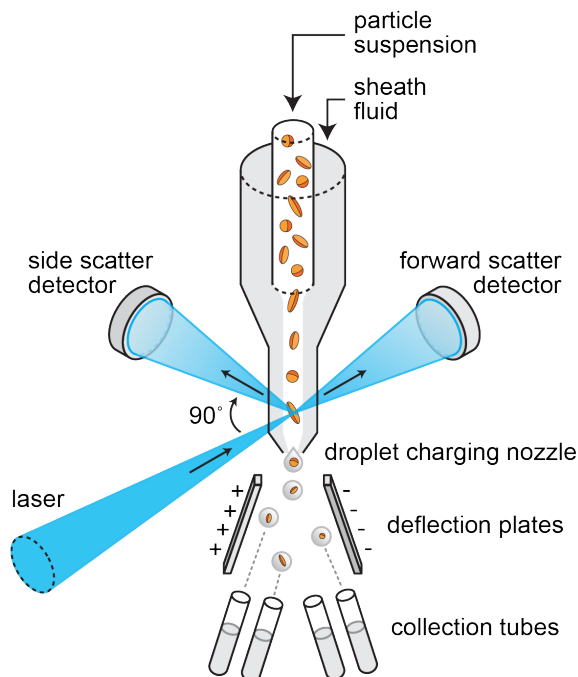
Figure 3.1: FACS scheme

exceeding 50,000 particles/s. Here we use FACS to analyze and sort mixtures of shaped polystyrene microparticles using single-particle elastic optical scattering measurements. With no special sample preparation or labeling required, we achieve high separation purity, throughput, and yield for a variety of particle morphologies.

3.2   Background and Theoretical Framework

3.2.1   FACS and Flow Cytometry

FACS is a flow-based single-particle analysis and sorting tool. There are three major elements to any FACS system: fluidic handling, optical interrogation, and particle sorting. A schematic of a FACS instrument is shown in Figure 3.1. A suspension containing cells or particles to be analyzed is flowed into the instrument. The sample stream is

coaxially injected through a flow nozzle into a saline buffer sheath flow that serves to hydrodynamically focus particles to a well-defined flow region in the core of the sheath flow. This hydrodynamic focusing process also ensures that particles flow through the instrument in single-file, enabling single particles to be interrogated one at a time and precisely manipulated downstream. The focused particles are subsequently illuminated by one or more lasers for fluorescence excitation as well as elastic scattering measurements. Scattered light is collected for measurement in two directions: at small (0±5 deg) angular deviations from the laser's direction of incidence ("forward scatter" or FSC) as well as perpendicular to the incident light (90±5 deg) ("side scatter" or SSC). Scattered light is collected and focused to detectors (FSC light is measured with a photodiode, while SSC and fluorescence are measured with PMTs). After optical interrogation, particles pass through a droplet nozzle that is excited at ultrasonic frequencies by a piezoelectric vibrator. Just as these droplets are broken off the main sample stream into air, a charging collar applies a net negative or positive charge (or no charge) to each droplet depending on the desired deflection. The ejected droplets then pass through a fixed electric field between two charged deflection plates; the direction and amplitude of their deflection is controlled by the polarity and amount of charge they receive from the charging collar at the droplet nozzle. Finally, the droplets are collected in tubes placed at appropriate angles beneath the deflection plates to collect the deflected droplets.

Analysis in FACS instruments is performed on the basis of the various scattering and fluorescence measurements that have been collected for each particle. To facilitate population-level visualization and sorting, FACS data are typically presented as 1-dimensional histograms (for examining a single measurement parameter for a collection of particles) or as correlated 2-dimensional scatter plots (for examining two measurement parameters simultaneously), where each point represents a single particle. Sorting is achieved by defining "gates," one-dimensional intervals or two-dimensional regions of

interest on these histograms or scatter plots. Detected particles, or "events," can be deflected to specific collection tubes based on whether or not they reside in a given gate. By performing Boolean gating, wherein gates are combined or assembled into hierarchies, particles can be classified and sorted based on more than just two parameters.

3.2.2   Elastic optical scattering in FACS

While FACS is most often thought of as a tool for measuring fluorescence (*i.e.*, inelastic optical scattering), it is also used to measure the elastic optical scattering properties of cells and microparticles. Fundamentally, scattering describes the interaction of incident light with dipoles in matter; elastic optical scattering involves light-matter interactions in which the energy (wavelength) of the incident and scattered light is the same. Scattering behavior —described by the angular intensity distribution and polarization of scattered light relative to the incident light —is strongly dependent on the wavelength and polarization of the incident light, as well as the intrinsic (refractive index) and extrinsic (size, shape) properties of the scatterer itself. In flow cytometry, the intensity of scattered light at small angles relative to the direction of incidence (forward scatter) is often used to gain insight into the size and refractive index of the interrogated object, while large-angle scattering (side scattering) provides additional information about the object's granularity or surface roughness.

Elastic scattering in flow cytometers has been rigorously characterized, both experimentally and theoretically using electromagnetic scattering theory. For instance, for polystyrene spheres, the strong dependence of FSC and SSC amplitude on particle size can be predicted using Mie theory (described below) [92]. Interestingly, the specific optical geometry of the FACS instrument has an important impact on scattering measurements. For example, the angular width of the forward scatter obscuration bar, which

42

blocks unscattered incident illumination at $\sim 0°$ from swamping the FSC detector, was found to affect the quantitative relationship between particle size and FSC intensity [92]. The role of incident beam geometry has also been explored [93]. The scattering properties of biological particles across a wide range of sizes have been rigorously characterized using FACS, ranging from cells on the order of 10s of microns [94–96] to sub-micron protein aggregates [97] and vesicles [98–100]. A good review of single-cell scattering analysis, including FACS and other methods, is provided by Kinnunen *et al.* [101]. Of note, the same fundamental phenomenon of elastic optical scattering is frequently used in synthetic particle characterization, whether in ensemble approaches such as dynamic light scattering or in single particle analyzers such as aerosol monitors [88–90].

In addition to using FACS to measure the amplitude of elastically scattered light, useful information about particle morphology may also be obtained by analyzing the temporal shape of the scattering signal pulse at the photodetector [102], which is generated as the particle passes through the interrogation beam. Sharpless *et al.* found that the pulse width of both the fluorescence signal [103] and the FSC signal [104] for spherical synthetic microparticles are strongly correlated with particle size. Leary and coworkers found a similar relationship between FSC pulse width and microsphere diameter [105]. Interestingly, the relationship between size and pulse shape differs significantly for FSC in comparison to SSC [102]. Pulse-width analysis has since been used extensively for size discrimination for a variety of biological targets such as endosomes [106, 107], immune cells [108], and algae [109].

Based on the fact that scattering can be measured at multiple angles (FSC and SSC) and analyzed using multiple parameters (scattering amplitude and pulse width), combinatorial analysis can enable more effective particle discrimination than the use of single parameters alone [110]. Terstappen *et al.* showed that by using various combinations of scattering parameters, the four most clinically-relevant distinct subtypes of white blood

cells can be separated from each other out of a white blood cell mixture [111,112]. Recent work by Tzur *et al.* found that gates based on combinations of scattering parameters (such as scattering amplitude and pulse width) are more effective for size-based discrimination than either parameter alone, for a wide variety of cell types [113].

3.2.3 Optical scattering for analysis and sorting of nonspherical particles

As described above, the relationship between scattering measurements and particle size has been extensively characterized; however, there is comparably little research regarding the use of scattering in FACS to characterize particle shape independent of size, even though the scattering behavior of both nonspherical cells [114] and nonspherical synthetic microparticles [115] is known to be orientation-depedent. In a patent application regarding a FACS-basd pulse-width analyzer, Leary *et al.* noted that pulse width measurements vary for identical nonspherical particles depending on their orientation when entering the interrogation beam [116]. The most common use of FACS for shape-based particle discrimination is blood typing, where disk-shaped erythrocytes can be separated from more spherical leukocytes. Early work by Salzman and coworkers showed that the optical scattering of disk-shaped red-blood cells takes on a unique distribution based on the range of potential orientations that the cells can take when being interrogated [117].

3.2.4 Simulating elastic optical scattering

While elastic optical scattering can be fully described across all length scales by solving Maxwell's equations, this is analytically and computationally impractical for all but the simplest scatterer geometries. It is therefore useful to consider a number of approximations that apply in limiting size regimes described by the characteristic scattering size

parameter $x = \frac{2\pi a}{\lambda}$, where a is the effective radius of the scatterer and λ is the wavelength of the incident radiation. For particles significantly smaller than the incident wavelength (Rayleigh scattering, where $x \ll 1$), the particle effectively acts as a single dipole, scattering light equally in all directions independent of shape but dependent on size, refractive index, and incident wavelength. For scatterers much larger than the illuminating wavelength ($x \gg 1$), the classical macroscopic descriptions provided by geometric optics, such as reflection and refraction, are sufficiently descriptive. For microparticle scattering, we are interested in an intermediate regime where the scatterer has a size similar to the incident wavelength; unfortunately, calculating such scattering behavior is more difficult than the large and small extremes described above due to the lack of simple approximations. Nevertheless, a number of approaches to obtaining approximate or exact solutions to Maxwell's equations may be used for particles in this size range. Mie theory in particular is a powerful tool, providing an exact solution to Maxwell's equations for an incident electromagnetic plane wave interacting with homogenous spherical scatterers [118].

While electromagnetic scattering of homogeneous spheres is a solved (and computationally tractable) problem using Mie theory, scattering of nonspherical particles is more difficult to simulate. Geometric approximations based on Mie theory have been explored for prolate and oblate spheroids [119]. Alternatively, the T-matrix method provides an exact solution for nonspherical scatterers [120]. T-matrix calculations have been used to predict scattering for spheroids [121], ellipsoids [122], and cylinders [123]. Spheroid-based simulations have been found to predict experimental scattering behavior of particles of arbitrary shape [124].

3.3   Results and Discussion

3.3.1   Optical scattering is dependent on particle shape, size, and orientation

We characterized microparticles in FACS using optical scattering measurements, captured both in the direction of incidence (FSC) and orthogonal to the direction of incidence (SSC). The intensity of scattered light in these directions is converted to a voltage by either a photodiode (for FSC) or PMT (for SSC), giving a characteristic voltage pulse for each particle as it passes through the interrogation beam. The FACS instrument digitizes this pulse and records the peak height (H) as well as the integrated pulse area (A). The pulse width (W) is then calculated and reported as the ratio of peak area to height. Since pulse width is calculated from the other two parameters, there are effectively only two "independent" pulse shape parameters; the pulse shape information provided by the instrument is fully contained in any pair of the three available parameters H, A, and W. For simplicity, we use pulse height and pulse width only. Therefore, since there are two scattering detectors, each particle's measurement has four independent parameters: pulse height and width at the forward detector (FSC-H and FSC-W), and pulse height and width at the orthogonal detector (SSC-H and SSC-W). Pulse height is closely related to the amplitude of the scattered light, while pulse width is a more complex function of both the particle's residence time in the interrogation beam as well as the shape of the pulse during interrogation.

We measured FSC and SSC for a variety of polymer microparticles with different morphologies. As a model system, we used microparticles formed by stretching an initial suspension of monodisperse polystyrene microspheres (6 μm diameter) in the manner described by Champion, *et al.* [62]. Specifically, we examined spheres and ellipsoids (aspect
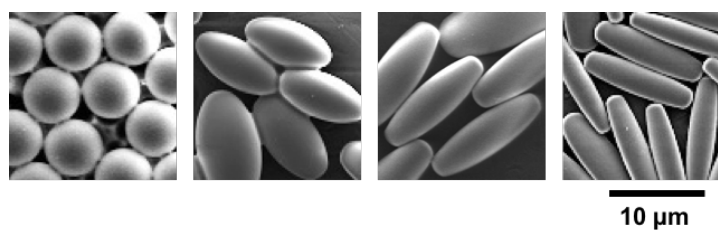
(a) SEM images of stretched polystyrene ellipsoids with aspect ratios of (left to right) 1.0, 2.0, 3.0, and 4.5.
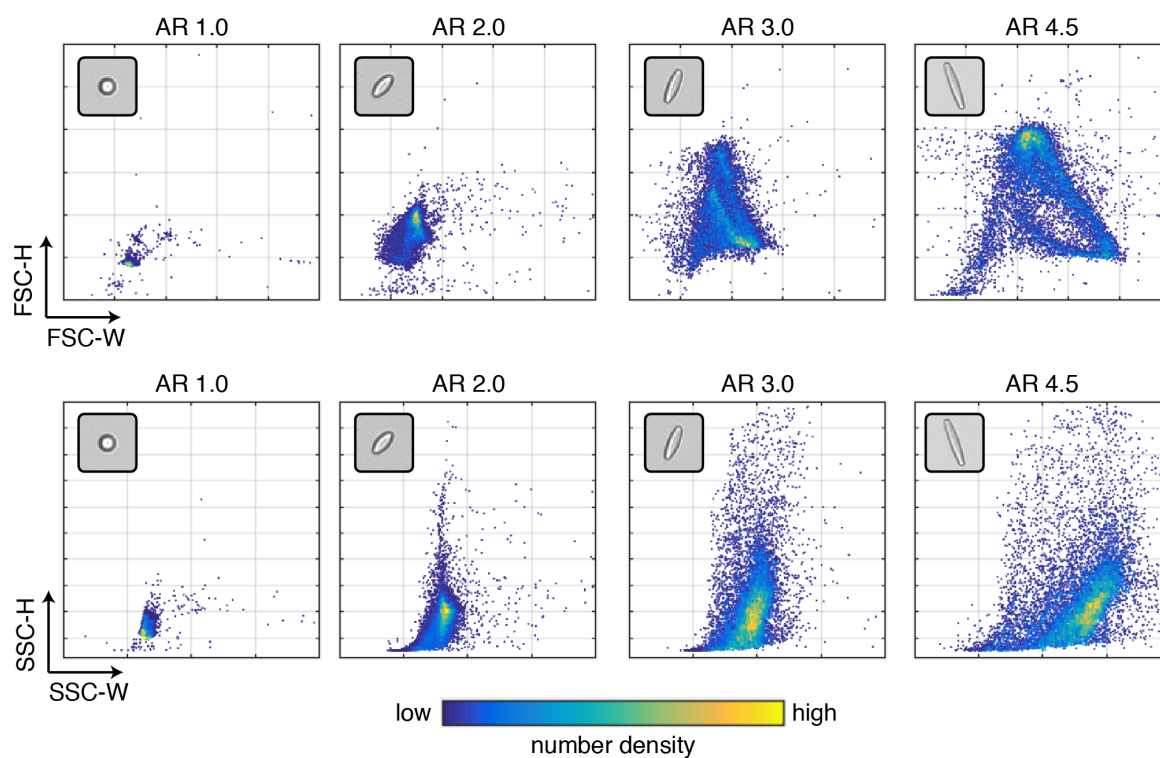
(b) Scattering profiles for microparticles with varying aspect ratios.

Figure 3.2: Shape dependence of scattering profiles for ellipsoids
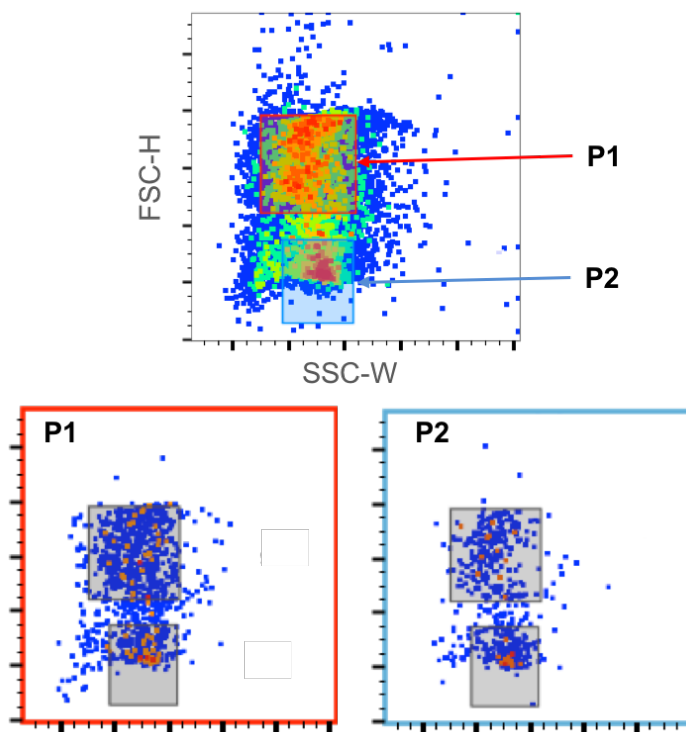
Figure 3.3: Scattering profiles of AR 4.5 ellipsoids arise from particle orientation, not sample heterogeneity. (top) Particles falling in gates P1 (red) and P2 (blue) were separately collected and re-analyzed in the instrument (bottom), each yielding the full scattering distribution of the original suspension.

ratios ranging from 1.1 to 4.5). Notably, all microparticles we examined had identical volumes and densities, differing only in terms of their shape. Nevertheless, we found that each particle morphology, when analyzed by scattering measurements in FACS, exhibited a distinct range of scattering parameters (FSC-H, FSC-W, SSC-H, and SSC-W). Two-dimensional correlated scatter plots show unique "scattering profiles" arising from particles of different morphologies. Spheres exhibit a relatively narrow distribution for all four parameters, while increasingly eccentric particles yield a significantly wider range of FSC-H, FSC-W, SSC-H, and SSC-W values. The complexity of these correlated scatter plots increases for increasingly nonspherical particles.

We next sought to determine whether scattering profiles are due to sample hetero-

geneity or are intrinsic to particle morphology, arising from the ensemble of random orientations available to the particles as they pass through the optical interrogation region. Due to the fully developed laminar (Poiseuille) flow in the sample stream, there is a parabolic velocity distribution across the cross section of the stream, such that fluid in the center of the stream flows faster than fluid at the channel walls. Consequently, particles passing through the sample stream experience a net torque and undergo rotation, leading to a full range of possible orientations for any particle entering the interrogation beam [125]. Because the angular distribution of scattering intensities is highly dependent on particle orientation relative to incident radiation [119], this leads to a range of potential FSC and SSC intensities for any given particle, depending on its orientation. To verify this, we defined sorting gates P1 and P2 on a 2-D scatter plot of FSC-H vs SSC-W for a relatively monodisperse suspension of AR 4.5 ellipsoids. These gates encapsulated two distinct population density peaks along the SSC-H dimension. Particles from each gate were collected and separately re-analyzed in the FACS instrument. A bimodal scattering profile nearly identical to that of the original unsorted suspension was observed for the particles obtained from both gates, strongly suggesting that the scattering distribution arises primarily from random particle orientations and not from sample heterogeneity. [3] Similar results were obtained for a suspension of stretched discs showing a trimodal population density distribution (data not shown); in this case, a three-way sort was performed and the sorted suspensions were re-analyzed, each yielding the full scattering distribution independently. Similar behavior has previously been reported for red blood cells, where the disc-like geometry results in a range of FSC and SSC intensities based on cell orientation [126,127]; cells collected from non-overlapping gates yielded the same full distribution of scattering parameters when re-measured in the instrument.

---

[3]Notably, there is a difference in the relative population percentages for the P1 and P2 gates in the two sorted samples, likely due to some polydispersity in the starting suspension.
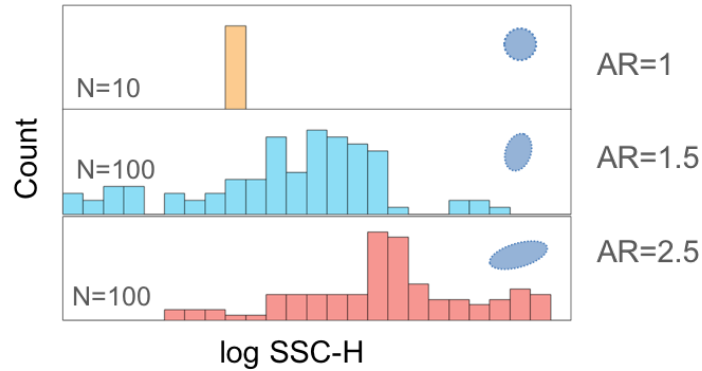
(a) Histograms of side-scatter intensity (integrated intensity over a solid angle spanning 83° to 97° in both the azimuth and zenith angles in the instrument coordinate system, see [128] for geometry details) for randomly oriented particles of varying aspect ratio, as simulated using the T-matrix method.
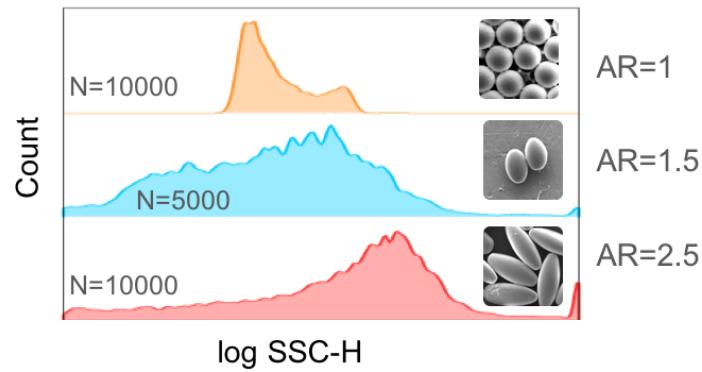
(b) Measured histograms of SSC-H for particles of varying aspect ratio.

Figure 3.4: Scattering simulations of side-scatter intensity distributions match the relationship between differently-shaped particles observed in experimental scattering measurements, further confirming that the observed distribution of scattering parameters arises due to random particle orientations. The discrepancy between simulated and measured scattering for spherical particles is likely due to slight polydispersity in the spherical particle suspension, resulting in a broader distribution.

We further sought to verify that the scattering profile arises from random scatterer orientations by performing numerical electromagnetic scattering simulations. Specifically, we used the T-matrix method [128, 129] to simulate scattering of spheres and ellipsoids with AR 1.5 and 2.5. These simulations calculate the angular dependence of the scattered light intensity for a variety of particle orientations relative to the direction of incident radiation. Using this approach, we show that the distribution of orthogonal scattering amplitudes (SSC-H) is predicted well by scattering at random orientations. These simulations match both the experimentally-observed distributions of values observed for all three particle types, as well as their relative values from shape-to-shape. Notably, this simulation does not capture the nonuniform incident beam geometry, which has a Gaussian intensity profile [91] and is focused to a height of 9 mum, smaller than the longest dimension of the AR 2.5 ellipsoids. This may explain the lack of measured high-intensity values for AR 2.5 compared with the simulated results. Due to convergence limitations of the specific T-matrix algorithm employed here, only aspect ratios up to 2.5 could be explored for particles of this volume using 488 nm illumination [130].

3.3.2   Defining gates to separate particles

We next attempted to sort a heterogeneous mixture of ellipsoidal particles (Figure 3.5a) based on scattering measurements. To do this, we sought to define minimally overlapping sort gates on a 2D correlated scatter plot of scattering parameters. We therefore decided to define gates on a plot of FSC-H vs. SSC-W, because the four different types of ellipsoids exhibited distinct (though overlapping) scattering profiles for this parameter pair. The scatter plot for the 4-way particle mixture is shown in Figure 3.5b. Sort gates were defined manually using the following procedure. First, population density plots of each particle type were examined to determine the highest-

density regions. Initial "high-yield" gates for each particle type were created around these population peaks. For each particle type, we then applied the high-yield gate to scatter plots of the three other particle types to see how many non-target particles would be included (*e.g.*, how many particles of AR 2.0, 3.0, or 4.5 would be included in the initial high-yield gate for AR 1.0). The high-yield gate was then manually adjusted to include the highest-density regions of the target particle type, while avoiding the highest-density regions of the non-target particle types. In this way, high-purity gates for each particle type could be defined (Figure 3.5c).

The results of this 4-way sort based on 2D gates are shown in Figure 3.6a. Sorted particle mixtures were recovered from the instrument and analyzed via optical microscopy to determine the sort purity (details in Section 3.5.4); purity values were renormalized to reflect a hypothetical 0.25:0.25:0.25:0.25 distribution of particle types as the sorter input. Although all sort gates resulted in purities exceeding 75%, only the gates for AR 1.0 and AR 4.5 particles resulted in purities above 95%. The lower purity achieved by the AR 2.0 and AR 3.0 gates can be attributed to a significant degree of overlap between these populations on the plot of SSC-W vs. FSC-H (Figure 3.6b). Moreover, there is significant overlap between the scatter plots for AR 3.0 and AR 4.5 particles, further worsening the purity of the AR 3.0 gate. Notably, the AR 1.0 and AR 4.5 gates both result in relatively high purities because their respective areas of highest population density are far from the population peaks of the other particle types.

3.3.3   Sorting with higher-dimensional gates

While sorting based on 2-D gates is possible, the highest purity attainable is limited by overlap between closely-related particle types. However, there are a total of 4 independent parameters available for sorting. The correlation between these scattering
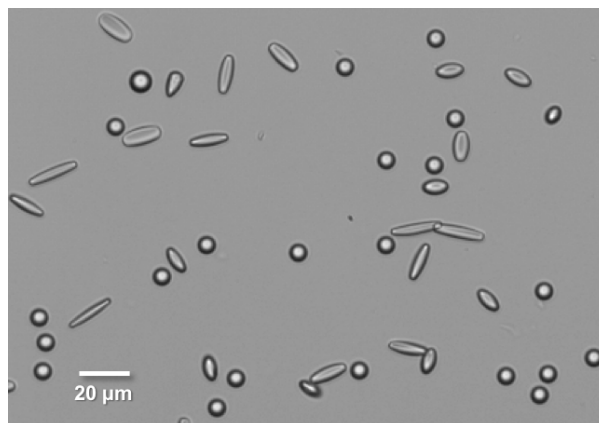
(a) Heterogeneous particle mixture for sorting, containing microparticles with aspect ratio 1.0, 2.0, 3.0, and 4.5
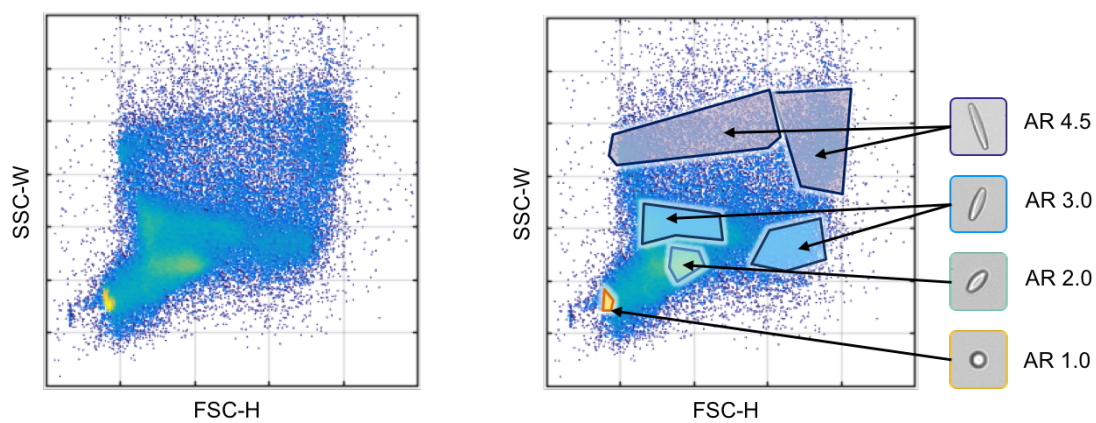
(b) Scattering profile for heterogeneous mixture

(c) Sorting gates for each particle type

Figure 3.5: Two-dimensional gate design for ellipsoid sorting.

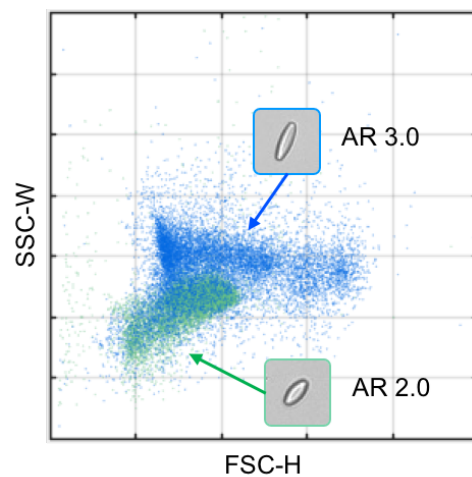(a) Purity for each particle type after performing the 2-D sort

(b) Closely related particle types have significant overlap in their 2-D scatter profiles

Figure 3.6: Sorting of ellipsoids based on 2-D gates

parameters for various particle types can thus be considered in a higher-dimensional space, as shown for example in the 3-D correlated scatter plots of FSC-W vs. FSC-H vs. SSC-H (Figure 3.7). Such higher-dimensional visualization reveals that populations which appear to significantly overlap on any given 2-D parameter space may actually be possible to separate in the higher-dimensional scattering space.

However, sorting particles based on gates defined in higher-dimensional space (3-D or 4-D) presents two important technical and practical challenges. First, we must determine a method for rigorously defining particle-specific regions in higher-dimensional scattering space that do not overlap each other. While visual inspection of the plots in Figure 3.7 suggest that such regions exist, defining and optimizing them is not a straightforward task. While a number of statistical tools are available for defining clusters in higher-dimensional FACS data [131–142], these are primarily designed to discover and distinguish unknown cell populations. Our problem is the inverse: we already know the unique scattering profiles for each particle type, but now want to determine the optimal higher-dimensional region for maximizing both yield and purity. The second key challenge is both practical and technical: the higher-dimensional gates, once discovered and defined, must then be translated for sorting with the FACS instrument software. Unfortunately, commercial FACS instruments are only capable of sorting based on gates drawn on 1-D histograms or 2-D correlated scatter plots; no software tool exists for sorting directly based on 3-D, 4-D, or higher-dimensional gates.

To overcome these problems and sort using 4-D gates, we first exploited the fact that a convex region in higher-dimensional space can be reconstructed from its projections onto lower-dimensional spaces. For each particle type, we defined a 4-D gate by creating 2-D gates on multiple 2-D parameter spaces (with 6 different 2-D spaces available based on pairwise combinations of FSC-H, FSC-W, SSC-H, and SSC-W). These 2-D gates are manually selected for yield and purity following a procedure similar to that described in
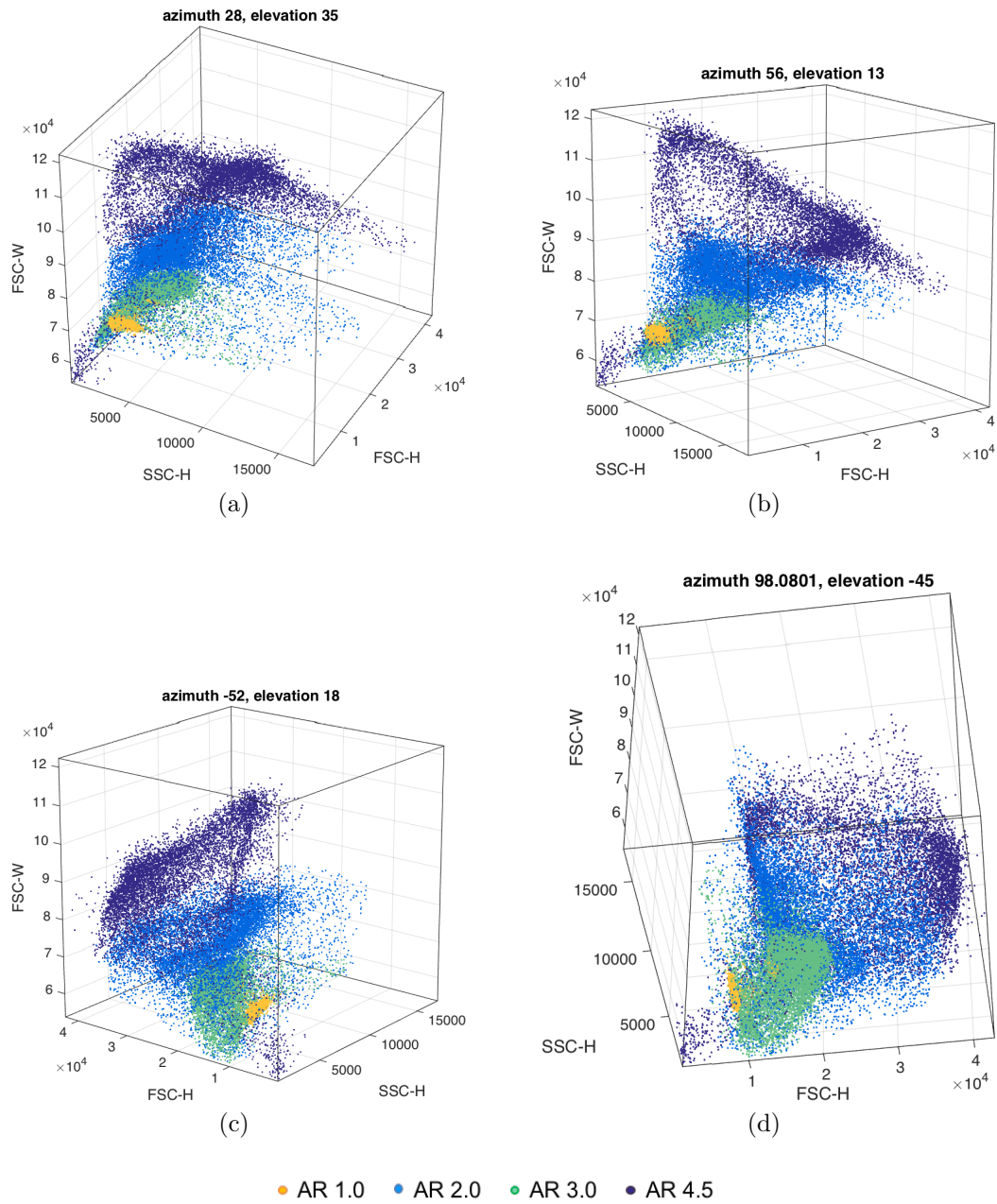
Figure 3.7: 3D visualization of scattering profiles for a four-component particle mixture

Section 3.3.2. The intersection of this set of 2-D gates then defines a particular region in 4-D space; and, because FACS software allows sorting based on Boolean combinations of 2-D gates, we can perform a sort based on this 4-D region using a logical "AND" combination of its constitutive 2-D projections. Therefore, this projection-reconstruction approach enables us to begin solving the two problems described above, by (i) facilitating the definition of a 4-D sorting region for each particle type and (ii) providing a simple means of translating that region to the FACS software for actual sorting.

However, while this projection-reconstruction approach can recreate simple convex regions in 4-D space, it is unable to capture more complicated geometric features such as concave regions, gaps, and holes. Practically, this limits the maximal purity attainable using gates developed with the projection-reconstruction approach, due to the high degree of overlap of different particle types' scattering profiles. To achieve higher purity, we need to define more complex 4-D regions in a manner that is still compatible with the constraints of the FACS software. We can achieve this higher geometric complexity by "rasterizing" the 4-D regions. This is achieved by defining 1-D slices (in the form of interval gates on a histogram plot) along one parameter axis, and creating multiple 2-D gates within the subpopulation defined by that slice using combinations of the other three parameters (*e.g.*, define a slice on the histogram of SSC-H, then create 2-D gates using combinations of FSC-H, FSC-W, and SSC-W). This approach allows complex 4-D geometries to be built up slice by slice. Moreover, this approach is compatible with the FACS sorting software, which allows sorting based not only on Boolean gate combinations, but also on nested sub-gates (*e.g.*, gates defined as subsets of populations defined by other gates). In this manner, each 1-D slice is a separate subpopulation of the total parent population; sets of intersecting 2-D gates are then applied to these subpopulations independently.

Using the combined rasterization and projection-reconstruction method, we per-
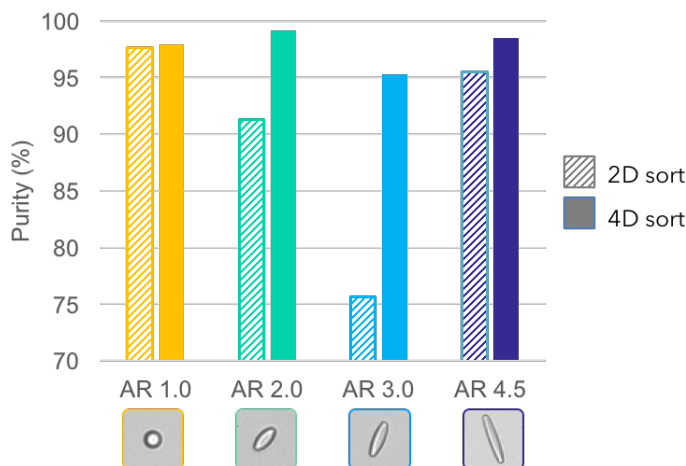
Figure 3.8: Results of sorting ellipsoids based on 4-D gates

formed a four-way sort based on 4-D gates. The specific gates used for each particle type are shown in Appendix B. Optimal gate combinations to achieve maximal purity were selected manually. We note that these sort gates do not necessarily use all possible combinations of scattering parameters; rather, an optimal combination of lower-dimensional gates was chosen that maximized purity while maintaining a reasonable yield. The results of the four-way 4-d sort are shown in Figure 3.8, compared side-by-side with the results of the 2-D sort. The 4-D sort resulted in sort purities above 95% for each particle type, with dramatic improvements for the AR 2.0 and AR 3.0 gates. These results demonstrate that sorting based on 4-D gates can overcome the purity limitations of 2-D sorting, by enabling separation of closely related particle morphologies in a higher dimensional scattering space.

3.3.4　Morphology-based enrichment from polydisperse suspensions: diblock copolymer "micro-footballs"

To demonstrate the utility and generality of our approach, we applied FACS to sort a "real-world" polydisperse mixture of nonspherical microparticles. Football-shaped

poly(styrene-b-2-vinylpyridine) (PS-b-P2VP) diblock copolymer microparticles can be synthesized with alternating stacked lamellar domains of PS and P2VP, causing them to act as Bragg reflectors. These "micro-football" particles have applications in stimuli-responsive optics, wherein pH can be used to tune the relative spacing of the lamellar Bragg domains and thus the particle color, while particle-to-particle arrangement can be used to tune overall reflectance. Such controllable optical properties, however, depends on well-defined particle morphology. Unfortunately, when synthesized through shear-induced emulsification, the resultant microparticle mixture is highly polydisperse (Figure 3.9a).

We used FACS to sort this polydisperse micro-football mixture. Unlike the stretched polystyrene spheroids used before, this mixture does not have well-defined subpopulations; rather, it contains a continuum of particle sizes and shapes. Consequently, the measured scattering profile of the polydisperse mixture shows a wide range of FSC-A and SSC-A values (Figure 3.9b). As a preliminary test, we sorted based on a number of 2-D gates in different regions of the correlated scatter plot (colored areas in Figure 3.9c). Sorted particles were recovered and analyzed via optical microscopy as before. Each gate resulted in a unique distribution of particle sizes as characterized by the particles' major axis length (Figure 3.10). For example, the high-FSC gate (gate 1, blue) contained far more particles with major axis lengths above 4 μm than the starting mixture or any of the other gates. Interestingly, although gates 2 and 3 (orange and magenta) have similar FSC-A values and differ only along the SSC-A axis, their resulting size distributions are appreciably different. These results show that FACS can be used to enrich subpopulations of a polydisperse particle mixture based on morphology, even when the scattering profiles of the individual subpopulations are not known ahead of time.
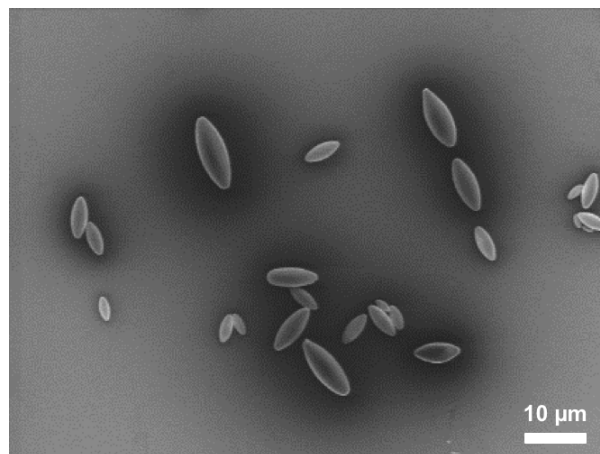
(a) SEM micrograph of polydisperse micro-footballs
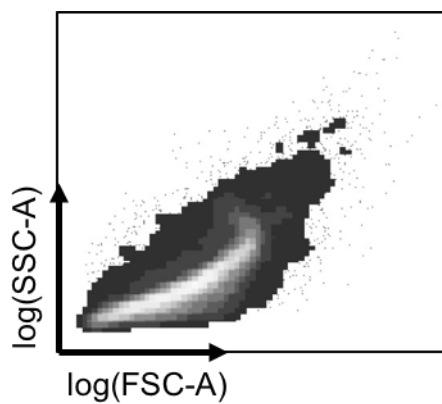
(b) 2-D scattering profile for polydisperse mixture of micro-footballs
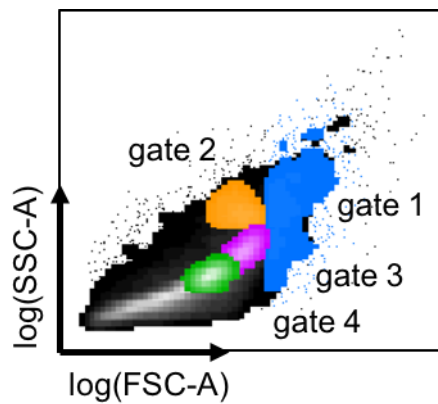
(c) Sorting gates (colored regions)

Figure 3.9: Sorting gates for diblock copolymer micro-footballs
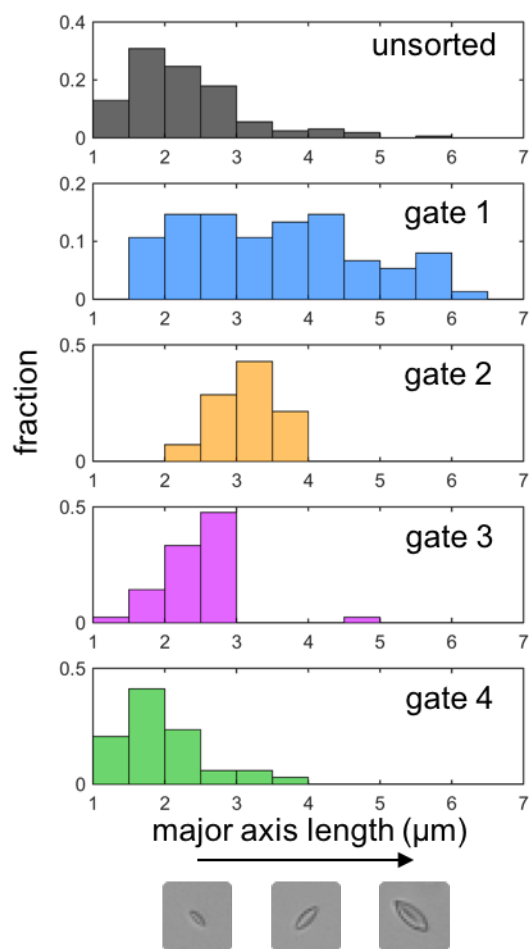
Figure 3.10: Sorting micro-footballs based on scattering results in selective enrichment for particles of various sizes in each gate.

3.3.5   Discussion

In this work, we have demonstrated the first use of a commercial FACS system to sort synthetic microparticles based on shape. Using only elastic optical scattering measurements captured at two angles, we showed the ability to sort multiple varieties of particle morphologies out of heterogeneous suspensions. Furthermore, by utilizing 3- and 4-dimensional gating strategies, we achieved high purity separation for closely related particle morphologies.

Although these preliminary sort results are promising, there are a number of areas of improvement that future works should address. First, for this work, we have focused primarily on maximizing purity; however, many applications of particle synthesis would also require high yield in order to obtain usable quantities of the desired particle morphology. Future gate design procedures, similar to those described above, could take into account the balance between yield and purity, enabling the selection of higher-yield or higher-purity gates depending on the application. The actual instrument yield should also be measured and compared to the predicted gate yield. Second, our existing gating strategy depends ultimately on manual, user-defined gates. While this is sufficient to achieve the high purities obtained in this work, it is time-intensive and ultimately too subjective to be useful as a general approach. Future algorithms could be developed to automate gate selection in either a deterministic fashion, where high-purity and high-yield regions of the 4-dimensional scattering space are selected according to pre-defined design rules, or in a probabilistic fashion, where psuedorandomly generated "seed" gates are tested and gradually evolved to maximize purity and/or yield. Third, further testing with additional morphology types, beyond ellipsoids, should be performed. Preliminary results with stretched discs (data not shown) suggest that this approach is generalizable to multiple particle geometries.

To gain insight into the fundamental nature of FACS-based scattering measurements, we performed simple scattering simulations to verify the orientation dependence of our measured scattering profiles. However, these simulations made a number of simplifying assumptions that should be either validated or corrected in the future. For instance, the simulations assume that our particles are perfect prolate spheroids (where the lengths of the two minor axes are equal), but they are actually irregular ellipsoids with significantly varying minor axes. In addition, the simulation does not take into account the FACS laser's nonuniform Gaussian intensity profile [91]. Future simulations should also more carefully leverage scatterer symmetry to reduce the necessary range of orientations to test and therefore speed up simulation time [93]. In addition, it may be possible to directly simulate arbitrary shapes [143, 144], further increasing the utility of scattering simulations for optimizing FACS-based particle sorting.

Even if these improvements are made, however, there are a number of limitations to this method that are potentially intrinsic to the FACS instrument. First, scattering and pulse width measurements are highly dependent on the specific optical geometry of the FACS instrument being used [110], potentially leading to unpredictable results for the same particle system when analyzed on different models of cytometer. However, we note that we developed our method on one of the most common FACS systems in use in the U.S. (the BD FACSAria II). In addition, the fluidic setup of the cytometer will have an important effect on the ensemble of microparticle orientations; for instance, stream-in-air FACS systems will tend to align oblong microparticles in the direction of flow, potentially resulting in different scattering profiles for the same microparticles from cytometer to cytometer. We also have demonstrated our system using polystyrene particles, which have a large refractive index mismatch with water and therefore scatter strongly. Materials with refractive indices closer to that of water may not provide as distinct of a scattering profile. Finally, we note that this method may not be suitable

for microparticles that are only stable in non-aqueous solvents, since most commercial FACS systems are only designed for use with water.

3.4   Conclusion

Shape-based microparticle sorting in FACS is a promising and potentially general approach to enriching designer microparticles based on morphology. Commercial FACS systems are becoming increasingly ubiquitous in both academic and industrial research settings, making our method accessible to a wide range of researchers. In the future, by exploiting other optical tools built into FACS instruments —such as the ability to measure particle autofluorescence at a variety of excitation wavelengths —FACS-based sorting could be used to enrich microparticles based on other material properties in addition to morphology. By leveraging the high performance (throughput and precision) of commercial FACS instruments, shape-based particle sorting with FACS could become a standard tool for laboratory-scale microparticle enrichment.

3.5   Experimental Methods

3.5.1   Microparticle synthesis and characterization

Microparticles were fabricated by the process described in [63]. Briefly, monodisperse spherical polystyrene (PS) particles (diameter of 6 μm) were suspended in an aqueous solution of polyvinyl alcohol (PVA) which was subsequently spread and dried into a sheet. The sphere-embedded sheet was then heated to 120 °C and stretched to achieve the desired particle shape, followed by cooling and washing to remove any PVA residue.

3.5.2   FACS instrumentation and operating procedure

All experiments were performed on a BD FacsAria II cell sorter. Particles were suspended in DI water and were sonicated for 5 min, vortexed, and filtered through a 35 μm filter prior to analysis. Unless otherwise noted, samples were processed at a cytometer flow rate setting of "1.0," corresponding to a flow rate of approximately 16 μl/min. Particles were sorted into 1.5 ml Eppendorf tubes containing 100 μl of DI water.

3.5.3   Scattering simulation validation

Angular scattering distributions for polystyrene ellipsoids were simulated in Python using a specific implementation of the T-matrix method, described by Mishchenko *et al.* [128] and released in Python by Leinonen *et al.* [129]. To validate this T-matrix algorithm, scattering from homogeneous spheres was simulated using both the T-matrix method and a well-characterized program based on Mie theory developed by Matzler *et al.* [145]. Simulations from both algorithms were performed for spheres of identical size and refractive index, resulting in exact overlap of the scattering distributions calculated by the two methods.

3.5.4   Microscopy analysis procedure for sorter results

Sorted particle samples were centrifuged at 13.7 krcf for 2 minutes to concentrate all particles at the bottom of the tube, and the supernatant was removed and saved so that only 40 μl of concentrated particle solution remained. The concentrated suspensions were then vortexed and 5 μl samples were pipetted onto a microscope coverslip placed on the imaging stage of an Olympus IX-73 inverted microscope. Particles were allowed to settle via gravity. Microscope images were captured across the entire deposited sample drop by scanning across the drop's width and height. Unless otherwise noted, all images

were captured in brightfield at a magnification of 40x using a Phantom v211 camera. Unsorted "input" particle suspensions were not concentrated prior to imaging.

Identification of particles in sorted samples containing highly distinguishable particle types (*e.g.*, spheres vs. ellipsoids or ellipsoids vs. discs) was performed manually. For samples containing particle types that were difficult to reliably distinguish manually (*e.g.*, ellipsoids with aspect ratio 2.5 vs 3.5), images were analyzed by a feature-identification program in MATLAB as follows. First, captured images were manually segmented in MATLAB to identify individual particles. The segmented regions were then analyzed with an ellipse-detection program in MATLAB that performs Canny edge detection and subsequently uses a Hough transform to calculate the best-fit ellipse for each edge in the image, using parameters for major axis length, minor axis length, center X-Y coordinates, and rotation angle[4]. Fitted ellipses were manually verified for each particle through visual inspection. The major axis of the fitted ellipse was found to be the most reliable particle identifier and was used to classify detected particles by their aspect ratio.

---

[4]Available on Mathworks Exchange at http://www.mathworks.com/matlabcentral/fileexchange/33970-ellipse-detection-using-1d-hough-transform, based on [146].

Chapter 4

High-Speed Image-Based Sorting of Cells and Microparticles

4.1 Introduction

[1] Flow cytometry and cell sorting have become irreplaceable tools for cell biology and bioengineering, enabling researchers to study large cell populations with single-cell resolution at high throughput. The current "gold standard" for cytometry is fluorescence-activated cell sorting (FACS), wherein cells are labeled with fluorescent stains or fluorophore-labeled antibodies and are subsequently analyzed based on their fluorescence signatures. Modern FACS instruments can achieve very high sort throughput (approaching 50,000 cells/s for state-of-the-art systems) and are capable of analyzing multiple fluorescence channels simultaneously, enabling serial sorting and enrichment of target cells based on a wide variety of phenotypic criteria. However, this high throughput comes at the expense of spatial resolution: FACS is based only on single point measurements of whole-cell

---

[1]At the date of compiling this thesis, March 17, 2016, this work is still in progress. The contents are thus presented as preliminary results.

fluorescence or scattering intensity.[2] Because of this lack of spatial resolution, FACS is incapable of sorting cells based on complex morphologies or internal cellular features, such as the spatial distribution of organelles or fluorescently-tagged proteins. Such 2-D information is necessary for studying cell cycle progression [147], protein aggregation disorders such as amyloidosis [148], nuclear translocation [149], and endosomal trafficking [150], to name a few. Two-dimensional spatial data is capable of conveying far more biologically useful phenotypic information than whole-cell fluorescence alone [151], but to date there is no system capable of sorting at FACS-like throughput based on two-dimensional microscopy.

The field of imaging flow cytometry has partially solved this problem by combining the rich spatial information of traditional 2-D microscopy with the high throughput of flow cytometry [152]. Unlike FACS, imaging flow cytometers capture full 2-D images of single cells in flow using a CCD or CMOS detector, providing multi-channel fluorescence images in addition to brightfield, darkfield, and (in some instruments) phase contrast images. Advances in high-speed CCD and CMOS technology have made it possible for commercial imaging flow cytometers to reach imaging throughputs approaching 5,000 cells/s at the time of writing this dissertation [149, 152, 153]. However, to date none of these systems are capable of sorting cells based on images. This is because imaging flow cytometers cannot perform real-time image analysis, instead depending on post-processing and off-line analysis after cell images have already been acquired. Such an approach is understandable, since extracting biologically relevant features from 2-D images is a computationally expensive task. Nevertheless, image-based cell sorting would require not only high-throughput image acquisition, but also real-time image analysis to classify cells for sorting based on image features.

---

[2]As discussed in the previous chapter, scattering measurements and fluorescence pulse width analysis do provide some basic spatial information about cell shape and size.

Here we present a system capable of high-throughput image-based sorting of cells and microparticles. Our SuperFACS[3] system combines high-speed CMOS imaging with optical microscopy and real-time image analysis to perform active image-based sorting on a microfluidic chip. To achieve this, we developed a microfluidic sorting platform, a real-time image acquisition interface, and real-time analysis algorithms for object detection, tracking, and feature extraction. We demonstrate sorting of synthetic microparticles based on size and shape, and show preliminary results for internal feature-based sorting of induced pluripotent stem cell-derived retinal pigment epithelium (iPSC-RPE) cells.

4.2   Background and Theoretical Framework

4.2.1   Imaging flow cytometers and image-based sorters

While FACS-based sorting is widespread, no commercial image-based sorters are available. A small number of image-based sorters have recently been reported in the literature, capable of sorting synthetic microparticles [154], bacteria culture in droplets [155], murine macrophages [156], and human embryonic stem cells [157] all based on simple image features like size, granularity, or single channel fluorescence intensity. Crucially, these systems are all limited to throughputs < 100 cells/s, many orders of magnitude lower than those reached by FACS systems. This is primarily due to their slow analysis algorithms (each taking on the order of ∼10 ms/cell). An imaging flow cytometer capable of real-time image analysis, without sorting, was reported to reach higher imaging and analysis throughputs of close to 500 cells/s, with an analysis time per frame of only 250 μs [158]. This fast analysis time was achieved through the use of highly optimized C++ code using the OpenCV image analysis library, implemented on a standard PC with a

---

[3]Yes, really.

six-core central processing unit.

4.2.2   Pressure-driven flow in microfluidic channels

Designing microfluidic flow channels for microparticle and cell manipulation requires an understanding of the physics of pressure-driven flow. For the simple case of pressure-driven laminar flow of an incompressible Newtonian fluid in a rigid channel, the important physical variables describing the system are pressure, hydraulic resistance, and volumetric flow rate. These quantities are related by the Hagen-Poiseuille equation for long cylindrical flow channel geometries:

$$\Delta P = \frac{128 \mu L Q}{\pi d^4} \tag{4.1}$$

where ΔP is the pressure drop, μ is the dynamic viscosity, L is the length of the channel, Q is the volumetric flow rate, and d is the diameter of the channel. By defining the hydraulic resistance $R_H = 128 \mu L / \pi d^4$, the Hagen-Poiseuille equation takes the form

$$\Delta P = Q R_H. \tag{4.2}$$

This is directly analogous to Ohm's law for voltage drop across a resistor, $\Delta V = IR$, where pressure P, flow rate Q, and hydraulic resistance R_H are analogous to voltage V, current I, and electrical resistance R, respectively. Similar analogies apply for other well-known rules describing electrical circuits. For instance, Kirchoff's voltage law and Kirchoff's current law can be recreated by considering mass and energy conservation in fluidic systems, leading to directly analogous rules describing flow and pressure drops in multi-channel, multi-node microfluidic systems. This leads to familiar solutions for total hydraulic resistance in networks of fluidic channels connected in series or in parallel.

Other insights from circuit theory can be applied using the same basic mathematics, such as the design of constant-pressure and constant-flow sources, as well as pressure and flow rate dividers. A good overview is provided in [159].

Due to the practical constraints of microfluidic channel fabrication, many microfluidic systems utilize rectangular channel geometries instead of circular cross-sections. While Equation 4.1 applies only to cylindrical channels, a general hydraulic resistance R_H can be defined such that Equation 4.2 applies to arbitrary channel geometries. For rectangular channels of height h and width w (with $w > h$), the hydraulic resistance is given exactly by [160]

$$R_{H,rec} = \frac{12\mu L}{h^4 \left(\frac{w}{h} - \left(\frac{192}{\pi^5} \sum_{n=1}^{\infty} \frac{1}{(2n-1)^5} \tanh \left(\frac{(2n-1)\pi w}{2h} \right) \right) \right)}. \tag{4.3}$$

Thus, R_H increases linearly with channel length L and is inversely proportional to the fourth power of h, with an additional geometric factor dependent on channel aspect ratio.

4.2.3   Dielectrophoresis

To enable high-speed sorting of cells and microparticles, we require a rapidly switchable, nondestructive actuation technique. Hydraulic switching using valves is gentle, but limited in throughput due to compliance in the fluidic system. Electrophoresis, while rapidly switchable and popular for macromolecule separation, requires the object being manipulated to have a net charge; in addition, it requires the use of strong DC fields, which can interfere with cell function (and even cause cell death) and can lead to unwanted bubble generation in the device due to electrolytic water splitting. An extensive review of microfluidic particle manipulation approaches is provided in [161]. Dielectrophoresis (DEP), on the other hand, exploits the force experienced by a dielectric object suspended in a medium of differing complex permittivity, all under the influence

of a spatially nonuniform AC electric field [162]. Therefore, DEP does not require particles to carry a net charge, and can be performed using biocompatible high-frequency AC fields that avoid electrolysis.

The DEP force experienced by a spherical particle of radius r and complex permittivity ϵ_p^* in a medium of complex permittivity ϵ_m^* in an electric field $\vec{E}$ is given by

$$F_{DEP} = 2\pi r^3 \epsilon_m \text{Re} \left\{ \frac{\epsilon_p^* - \epsilon_m^*}{\epsilon_p^* + 2\epsilon_m^*} \right\} \nabla |\vec{E}|^2 \quad \text{where} \quad \epsilon_i^* = \epsilon_i + \frac{\sigma_i}{j\omega_i}, \tag{4.4}$$

where the term in brackets is the Clausius-Mossotti (CM) factor f_{CM}. The complex permittivity can be rewritten in terms of the absolute permittivity $\epsilon = \epsilon_r \epsilon_0$, where ϵ_r is the dielectric constant and ϵ_0 is the vacuum permittivity; the conductivity $\sigma = \sigma_b + \frac{2K_s}{r}$, where σ_b is the bulk conductivity and K_s is the surface conductivity [163]; and the applied field frequency ω. Thus, the DEP force on a particle of a given size depends on (i) the difference in dielectric constant and conductivity between the particle and the medium (captured in f_{CM}), (ii) the frequency of the applied field (which determines the sign and magnitude of f_{CM}), and (iii) the gradient of the electric field (which depends on electrode geometry and applied voltage) [162]. In order to achieve the maximum DEP force possible, the frequency and medium conditions must be optimized to maximize the magnitude of f_{CM}, while the electric field gradient must be made as sharp as possible near the path of the object in flow. Notably, for a given particle and medium, f_{CM} may be either positive or negative depending on frequency, allowing the selection of either an attractive or repulsive DEP force. Dielectrophoretic sorters have been reported for droplets [154, 155, 164, 165], cells [166–168], and microparticles [166].
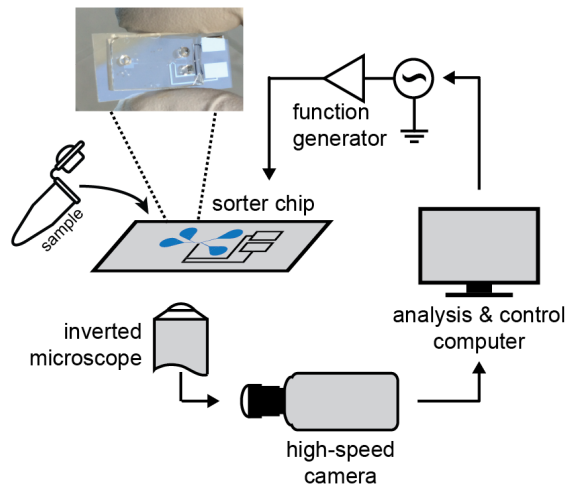
Figure 4.1: SuperFACS system scheme

4.3   Results and Discussion

4.3.1   SuperFACS system overview

To perform image-based sorting of cells and microparticles, the SuperFACS system combines three key functions: (i) microfluidic particle manipulation, (ii) high-speed microscopy, and (iii) real-time image analysis. The scheme for SuperFACS operation is shown in Figure 4.1. Particles flowing one-by-one through the microfluidic chip are imaged through an inverted microscope using a high-speed camera. These images are transferred to a computer in real-time, where a custom program performs image analysis to detect, analyze, and identify particles in the microchannel. Based on this analysis, particles classified as "target" objects are actively sorted into a separate collection channel within the microfluidic chip; this sorting is achieved using DEP actuator electrodes on the chip, which are attached to a function generator controlled by the analysis computer. In this way, particles flowing through the SuperFACS chip are imaged, analyzed, and sorted in a serial manner.

73

4.3.2   Microfluidic channel for particle handling and flow control

The sorter chip uses pressure-driven flow to focus the input mixture of microparticles to a single-file stream for imaging and subsequent sorting at a Y-junction downstream in the chip (Figure 4.2). The chip consists of two layers: a glass substrate with deposited microelectrodes, bonded to a PDMS flow channel fabricated using soft lithography (details in Section 4.5.1). The chip has three fluidic inputs: (1) the sample sheath inlet, which provides a flow of buffer to propel particles through the chip and prevent particle settling [169]; (2) the sample injection port, where a concentrated suspension of cells or microparticles is introduced into the chip; and (3) the focusing sheath inlet, which provides a secondary stream of buffer that focuses the particles to a narrow range of streamlines in the channel and introduces additional longitudinal spacing between subsequent beads [170] (Figure 4.2b, left inset), thereby enabling consistent actuation. Particles are imaged before reaching the actuator, which is located upstream of the Y-junction (Figure 4.2b, right inset). By default (that is, without DEP actuation), particles flow into the waste outlet (bottom of diagram) at the Y-junction, because it is wider and therefore has slightly lower flow resistance. However, particles actuated by the DEP electrodes will be deflected away from the electrodes into a streamline leading to the collection outlet (top of diagram).

Fluid flow through the SuperFACS chip is driven by a simple hydrostatic pressure source. The two sheath inlets are connected via fluid-filled tubing to an off-chip fluid reservoir, while the waste and collection outlets are similarly connected to a second fluid reservoir (the sample injection port is sealed after the introduction of the concentrated sample solution, and thus no flow occurs through this port during device operation). The total pressure difference between the inlets and outlets is determined by the relative heights of the fluid columns in the inlet reservoir and the outlet reservoir, resulting from
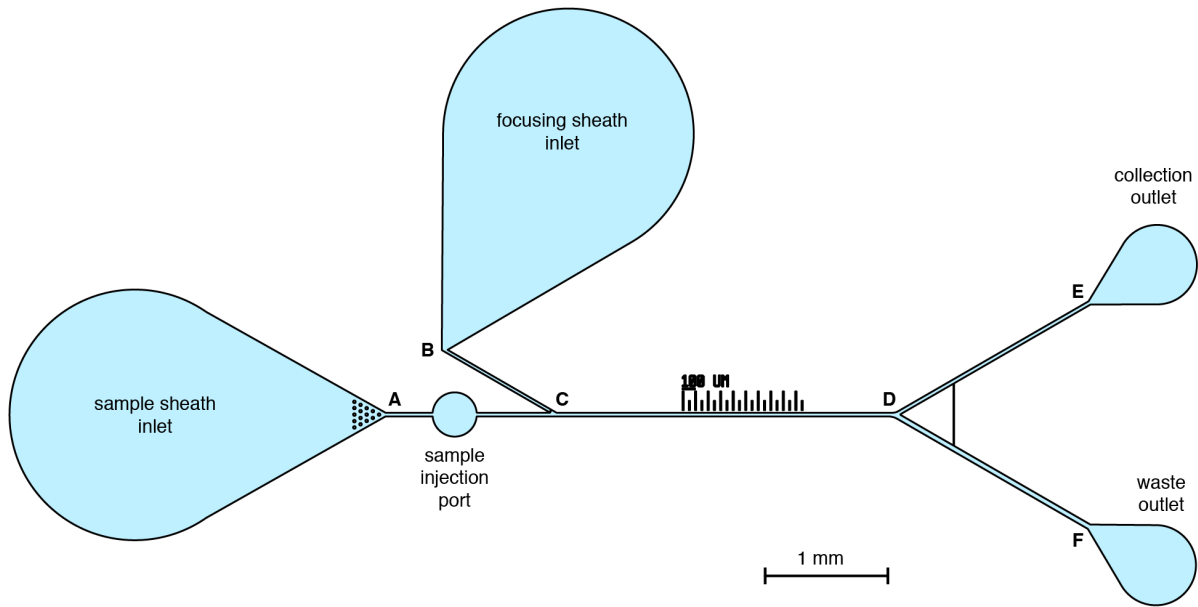
(a) SuperFACS flow channel design
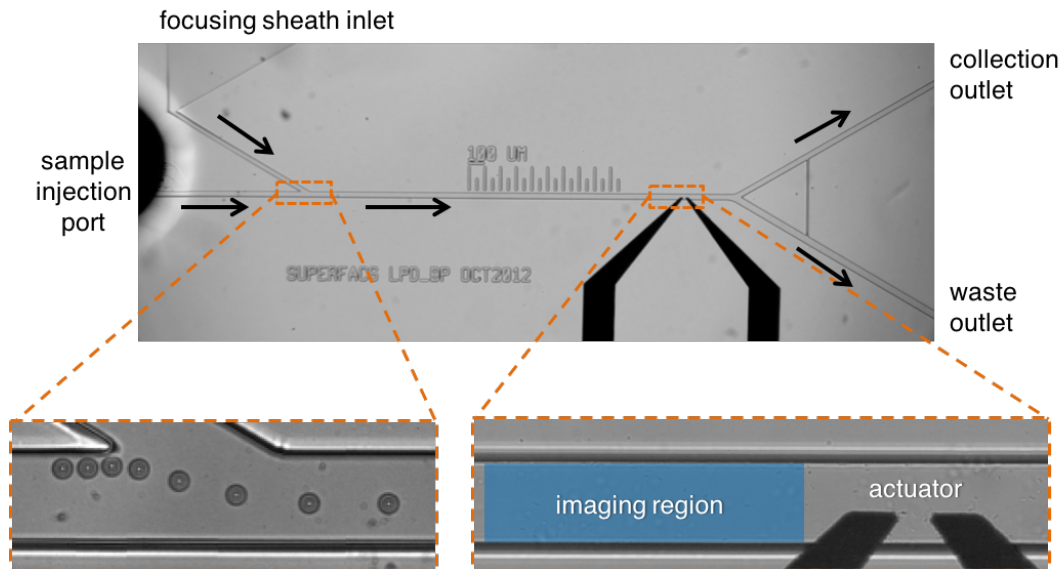
(b) Optical micrograph of assembled SuperFACS chip with flow channel and sorter electrodes. Arrows indicate direction of flow. Left inset shows magnified view of focusing sheath performance for a single 6 μm polystyrene microbead (time-lapse image sequence captured at 30 fps). Right inset shows magnified view of imaging and actuation regions.

Figure 4.2: SuperFACS flow channel design and layout

Segment	Width (μm)	Height (μm)	Length (μm)	R_H (Pa·m^{-3}·s)	Q (μL·hr^{-1})
AC	30	25	615	2.81×10^{13}	1.41
BC	25	25	1000	6.48×10^{13}	0.61
CD	30	25	2725	1.25×10^{14}	2.02
DE	30	25	1750	8.00×10^{13}	0.77
DF	40	25	1750	4.90×10^{13}	1.25
Total	-	-	-	1.75×10^{14}	2.02

Table 4.1: Hydraulic resistance calculations for the channel segments shown in Figure 4.2a for water at 25 °C. Example flow rates Q are calculated for the hydrostatic pressure resulting from a 1 cm height differential between the inlet and outlet fluid reservoirs. Note that the length of AC does not include the ~ 700 μm diameter sample injector port, whose contribution to the total hydraulic resistance between points A and C is very small.

gravitational force on the two fluid columns; this pressure difference results in net fluid flow across the device. By simply changing the fluid column height in the reservoirs (*e.g.* by adding or removing fluid), we have a highly controllable method of adjusting the fluid flow rate through the chip; moreover, the reservoir volume is large relative to the total volume flowed through the chip during an experiment, meaning that flow rates are stable over time. Notably, because both inlets are connected to a common fluid reservoir, there is no pressure difference across the inlets and therefore no risk of inlet-to-inlet backflow; the same is true for the outlets. The relative flow rates through the individual inlet channels **AC** and **BC** and outlet channels **DE** and **DF** (Figure 4.2a) are a result of each channel's dimensions, which are designed to provide the appropriate flow ratios at each junction. The channel dimensions and calculated flow rates in each channel for a 1 cm inlet-to-outlet reservoir height difference is shown in Table 4.1. In summary, our hydrostatic control scheme enables robust and reliable fluidic operation of the SuperFACS chip without a complex pumping setup.
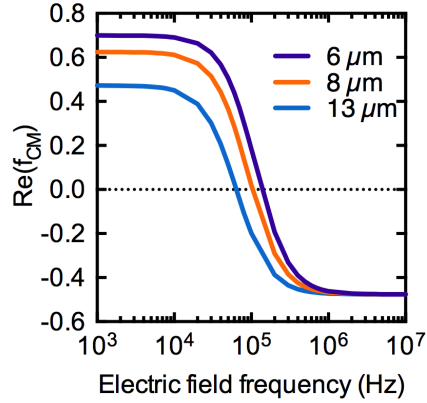
Figure 4.3: Real component of the calculated Clausius-Mossotti factor f_{CM} as a function of applied field frequency for polystyrene spheres of varying diameter suspended in deionized water.

4.3.3   Dielectrophoretic actuation

To design and implement an optimal DEP actuator, we mathematically simulated the effects of particle size, electric field frequency, and electrode geometry on the strength and polarity of the DEP force. We first calculated the Clausius-Mossotti factor, which determines the magnitude and direction of the DEP force, for polystyrene spheres of varying size suspended in deionized water over a range of applied frequencies, using Equation 4.4 (Figure 4.3). These results indicate that DEP is strongly attractive ("positive DEP", or pDEP) at lower frequencies, and strongly repulsive ("negative DEP", or nDEP) at higher frequencies; moreover, the crossover frequency between pDEP and nDEP is size-dependent, in agreement with results reported elsewhere [171, 172]. Although polystyrene spheres can undergo both pDEP and nDEP depending on frequency, cells suspended in salt-containing cell culture media (DMEM, conductivity 1.5 S/m) undergo only negative DEP, regardless of applied field frequency [173]. Therefore we elected to use an actuator design based on repulsive nDEP only.

We next used finite element analysis (COMSOL) to simulate the two-dimensional DEP force field arising from different electrode designs. As expected, smaller electrode
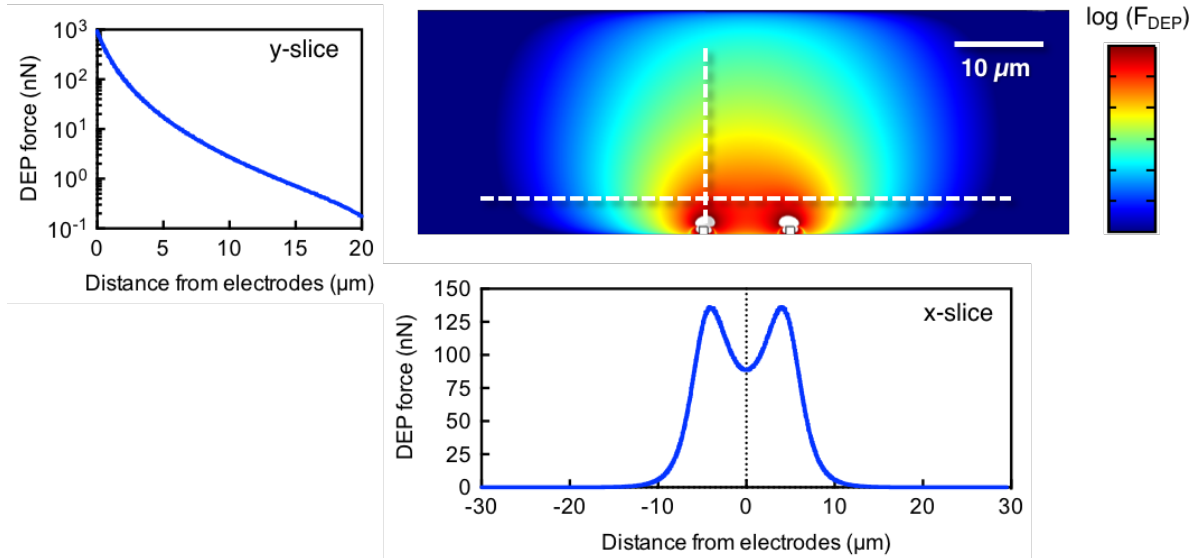
Figure 4.4: Simulated DEP force experienced by a 6 μm polystyrene particle suspended in deionized water for electrodes spaced 10 μm apart, with a driving field frequency of 1 MHz and a peak-to-peak voltage of 40 V. Insets show the 1-D force distribution for slices (white dashed lines) perpendicular to the direction of flow (left inset) and parallel to the direction of flow (bottom inset). Only the y-component of the force (*e.g.*, perpendicular to the direction of flow) is shown.

spacings resulted in stronger electric field gradients and higher possible DEP forces. We chose a 10 μm electrode spacing because it achieves strong DEP deflection, but is still facile to fabricate using standard photolithography. Figure 4.4 shows the two-dimensional repulsive DEP force distribution in the channel for electrodes spaced 10 μm apart and protruding 1 μm into the channel for a 6 μm polystyrene sphere suspended in deionized water, with an applied potential of 40 V_{PP} at 1 MHz. These simulations indicate that the DEP force is highly localized at the electrode tips and is strongly position-dependent in the channel.

Finally, based on these simulated designs, we fabricated and tested the DEP actuator. The chip's platinum actuator electrodes (10 μm spacing) are connected to a function generator and amplifier which provide the necessary AC voltage. We verified the actuator's performance for deflecting both polystyrene microparticles (Figure 4.5a) and live human

(a) Polystyrene microsphere   (b) MCF-7 cell
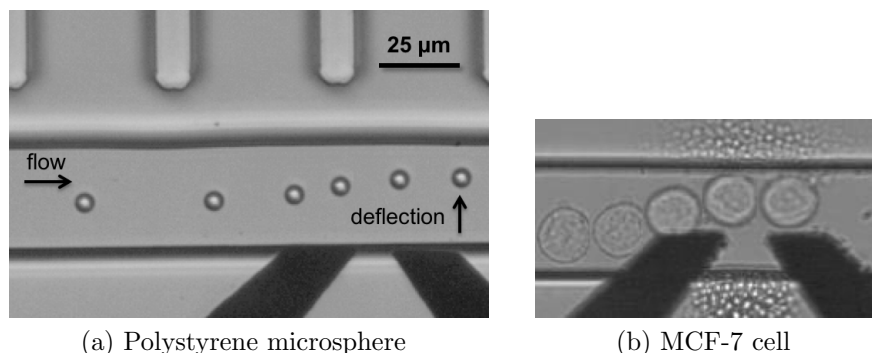
Figure 4.5: Time-lapse image composites of DEP actuation of a polystyrene microsphere in water (a) and a human breast cancer cell in cell culture media (b). Flow direction is left-to-right.

cancer cells (Figure 4.5b), both with a driving frequency of 1 MHz and a peak-to-peak voltage of 34 V. For both synthetic microparticles and live cells, the actuators provide sufficient nDEP repulsive force to deflect the particles or cells into the collection outlet.

4.3.4   Imaging, tracking, analysis, and classification

The assembled SuperFACS chip is mounted on an inverted microscope (Olympus IX-73), and imaging of the flow channel is performed using a high-speed CMOS camera (Vision Research Phantom v211). Sorting requires us to obtain image data from the camera in real-time, but commercial high-speed cameras are only designed to store images on internal memory and transfer them to an external computer after the full image sequence has been captured [4]. To overcome this problem and obtain images in real-time, we wrote a custom interface that bypasses the camera's internal storage and delivers image data directly to the analysis computer. This interface is built around a manufacturer-provided API that enables direct access to the camera's "image preview" function over a 1 Gb/s ethernet connection. Using this approach, we can capture a live stream of 8-bit images

---

[4]Specifically, high-speed cameras continuously store data from the image sensor on internal flash memory using a circular buffer; when triggered by an external computer, the camera then "dumps" the most recent images from its internal memory to an external computer for storage and analysis.

from the camera at a resolution of 512×56 px at a framerate of 250 fps.

This stream of images is continuously processed by an analysis program that performs three key tasks for each frame: (i) object detection, to determine if an object such as a microparticle or cell is present in the image; (ii) object tracking, to determine the object's location and speed by comparing it to objects detected in previous frames; and (iii) object classification, in which the relevant image feature for sorting is extracted and quantified, enabling an eventual sorting decision. The program first uses contrast thresholding and edge detection to determine if the image is occupied by any objects of interest, defined as any pixels with sufficiently high contrast compared to the channel background. If any such edges are present, the program performs image segmentation using feature-specific algorithms, such as circle or ellipse detection. These detection algorithms provide the size and location of any objects in the frame; the program then performs frame-to-frame comparisons to determine if a given object in the present frame is the same object as detected in the previous frame or is a new object. If the object has been detected in the preceding frame(s), its position in the channel is compared to its position in previous frames to determine its displacement. This displacement, combined with the images' timestamps, can be used to calculate the object's velocity. The program uses this velocity measurement to calculate the precise time delay required for accurate DEP actuation of the particle downstream. This dynamic velocity tracking is important because particles passing through the channel can have varying velocities due to the non-uniform (parabolic Poiseuille flow) cross-sectional flow profile in the channel, resulting in variable time delays between the imaging region and the actuator for different particles.

Finally, the program compares the extracted image features for a given object to a user-defined sort criteria, classifying the object as "target" or "non-target" for sorting downstream. If the object is classified as "non-target," no action is taken and the object will flow to the waste channel by default. If the object is classified as "target," the

program will use the object's detected velocity to calculate the appropriate time delay for activating the DEP electrodes, which are situated a known fixed distance downstream from the imaging region. The program activates the electrodes by triggering a function generator using a 5V TTL signal through the computer's serial port. To facilitate post-experiment analysis, all images containing detected objects are saved and timestamped.

4.3.5   Size-based sorting of microparticles

As an initial test of our system, we demonstrated real-time sorting of spherical polystyrene beads based on size. Specifically, a mixture of 13 μm and 8 μm diameter beads suspended in a water/surfactant solution was flowed through the SuperFACS chip. Bead images were analyzed via edge detection and subsequent circle detection using the circle Hough Transform [174], which provides the center coordinates and radius of any detected circular objects (Figure 4.6a). Total time for image acquisition, transfer, and analysis was $\sim$ 10 ms per image. The program then checked to see whether the radius measured for the bead in the current image was larger or smaller than the threshold value for sorting. If the radius met the sort criteria (in this case, was smaller than the sort threshold), then the program classified the bead as a "target" object for subsequent actuation and sorting into the collection outlet downstream. For frames with a bead with a radius above the sorting threshold, the electrodes were not energized and thus the bead was allowed to pass into the waste outlet. To verify sorter performance, we used the program's position tracking ability to monitor each beads center coordinates both upstream and downstream of the actuator electrodes. The deflected beads exhibit a large change in their position in the y-direction (*i.e.*, perpendicular to the direction of flow), providing an automatic means of detecting whether a bead was deflected or not. Results from this preliminary sort are shown in Figure 4.6a, which plots the observed

(a) Circular edge (orange and blue outlines) of polystyrene microspheres detected by the circle Hough Transform

(b) Size-based sort results
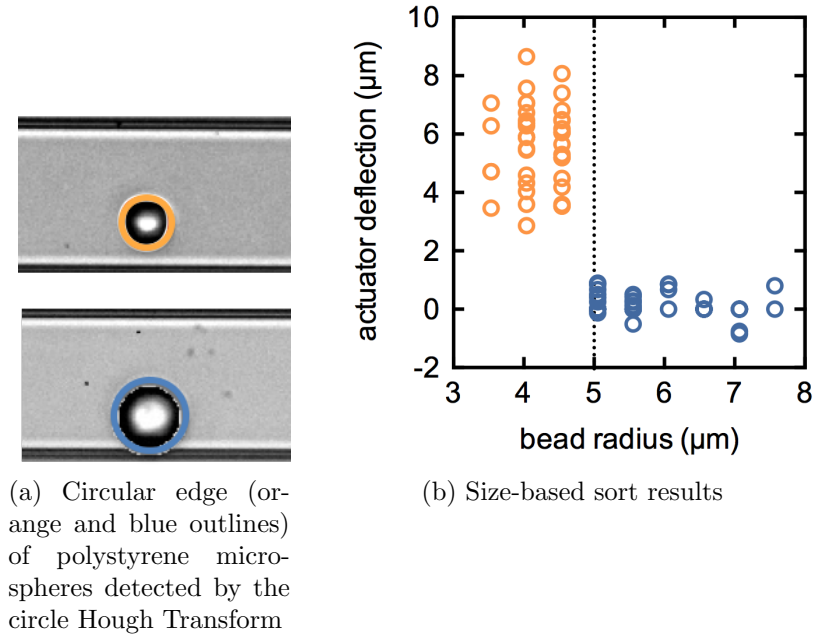
Figure 4.6: Sorting of microparticles based on size

bead deflection due to DEP actuation against the detected bead radius. Only those beads whose radius was measured to be below the sort threshold of 5 μm were actuated into the collection channel, as intended.

4.3.6 Shape-based sorting of microparticles

We next used our sorter to perform the more sophisticated task of sorting microparticles based on two-dimensional shape. As a model system, we attempted to sort stretched polystyrene ellipsoids (described in detail in Chapter 3) based on their aspect ratio. To do this, we utilized an open-source ellipse detection algorithm in the OpenCV imaging library based on least-squares fitting [175]; this algorithm provides the major and minor axis lengths of the fitted ellipse, in addition to center coordinates and rotation angle (Figure 4.7a. Using this algorithm, we sorted a mixture of stretched ellipsoids and spheres, with the sorting criteria that only objects with an aspect ratio exceeding 2.0 be deflected

into the collection channel. Results for this sort, quantified in terms of measured actuator deflection as in the preceding section, are shown in Figure 4.7b, with the total number of particles directed into the target and waste outlets shown in Figure 4.7c. As intended, only those particles with detected aspect ratios greater than 2 were deflected. However, we note that an appreciable number of detected "target" particles were not actuated. This was due to suboptimal alignment of the particles as they flowed through the channel, arising from a faulty focusing sheath inlet. Thus, some of the particles were already at the "top" of the channel and could not be deflected further. Manual inspection of the images recorded during this experiment reveal that even for those beads with AR¿2 where no deflection was detected due to their position at the upper edge of the channel, the actuator actually did fire at the appropriate time, as revealed by motion of the particle out of the microscope's focal plane.
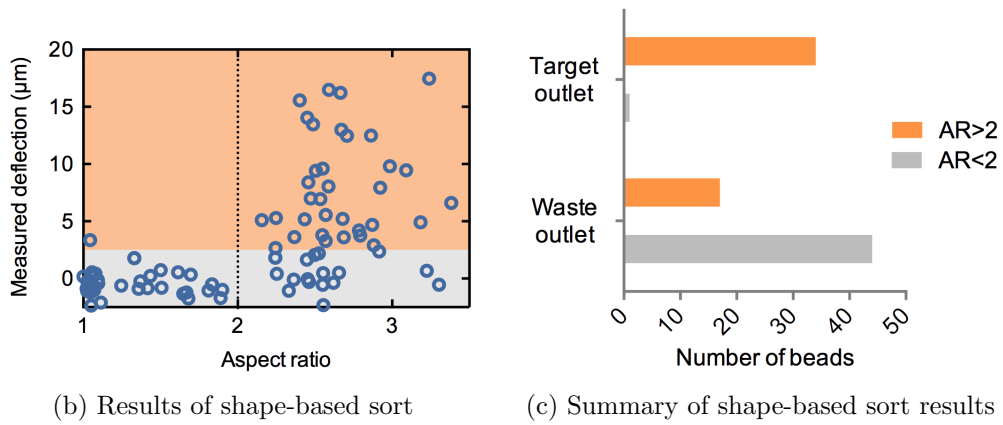
4.3.7   Toward image-based sorting of live cells

Having demonstrated sorting of synthetic particles based on two separate 2-D image features (detected radius and aspect ratio), we next sought to sort live cells using the SuperFACS system. However, cells present a number of challenges for image analysis compared to synthetic microparticles. First, unlike synthetic microparticles, cells can take on a wide range of irregular shapes and sizes, making it difficult to define a specific shape or feature *a priori* for the algorithm to detect, *e.g.*, spheres or ellipses. Second, when viewed in the brightfield mode, cells have relatively low contrast with the channel background compared to polystyrene microparticles, due to the similar refractive index between the cells and their suspension media. This leads to less robust edge detection, resulting in failed or inconsistent object recognition using the object-oriented shape detection algorithms described above.
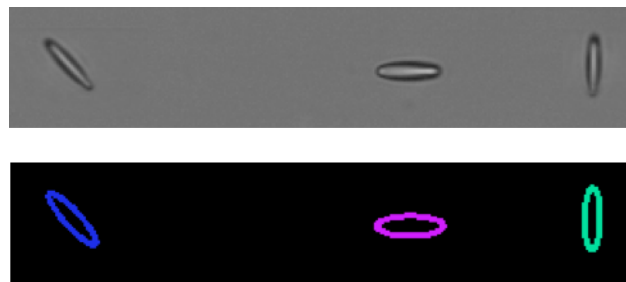
(a) Example fits for ellipsoid microparticles in the flow channel using the ellipse detection algorithm

(b) Results of shape-based sort

(c) Summary of shape-based sort results

Figure 4.7: Sorting of microparticles based on shape

To overcome these problems, we developed a new cell tracking algorithm for detecting, tracking, and analyzing cells of arbitrary shape, size, and contrast. At the heart of this algorithm is a pixel-based contrast analysis scheme, which detects cells by finding groups of pixels with brightness values different from the channel background. This algorithm is implemented via a five-step procedure (Figure 4.8). First, the input image undergoes Gaussian smoothing to minimize the effect of image sensor noise (Figure 4.8a). Second, all pixels with values close to the average channel background brightness are subtracted, leaving only those "feature pixels" that are sufficiently brighter or darker than the background (Figure 4.8b). Next, the channel is downsampled so that immediately proximal feature pixels are grouped together (Figure 4.8c). Connected component analysis using an 8-way nearest neighbor algorithm on the downsampled grid is used to identify clusters, or "connected components," of feature pixels (Figure 4.8d). Finally, overlapping clusters are merged using a blob association algorithm, and only clusters above a certain size cutoff (*e.g.*, the smallest cell size expected) are preserved (Figure 4.8e), in order to reject contrast artifacts such as debris in the channel.

The final outputs of the cell tracking algorithm are the cluster of contrasting feature pixels, as well as the rectangular region-of-interest (ROI) bounding the detected cell, from which the cell's approximate center coordinates and size may be determined. Further cell-specific image analysis, either pixel-based or object-oriented, can subsequently be performed on either the feature pixels only, or on all pixels contained within the ROI. There are several key benefits to this algorithm's design. First, because it is based on pixel analysis, it is generalizable to potentially any type of object moving through the flow channel, so long as it has some contrast with the channel background (*i.e.*, is visible). Second, the algorithm's computational simplicity makes it very fast to operate, taking only ~ 6 ms per frame. Third, it decouples the task of object detection/tracking from object analysis/classification. Because stable sorter operation requires object de-

(a) Gaussian smoothed input

(b) Background subtraction
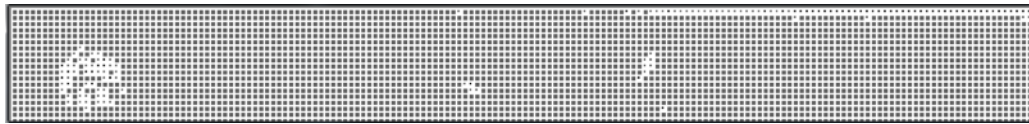
(c) Downsampling and pixel grouping
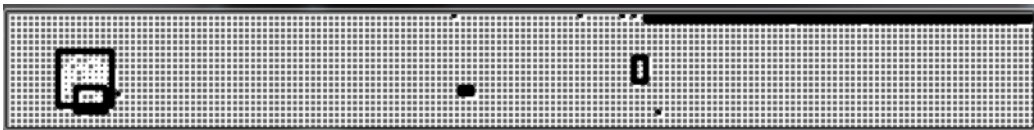
(d) Connected component analysis (black boxes indicate connected components)

(e) Blob association and artifact rejection, with the final "cell ROI" shown as a black rectangle containing the white "feature pixels"

Figure 4.8: Contrast-based object tracking algorithm demonstrated for an image of an RPE cell in the flow channel

tection and tracking to be performed on each frame, the overall sorter throughput is coupled to the tracking analysis time per frame. However, object analysis/classification can be performed on the basis of a single frame. While the relatively fast algorithms used for shape detection above are not a problem in this regard, more soph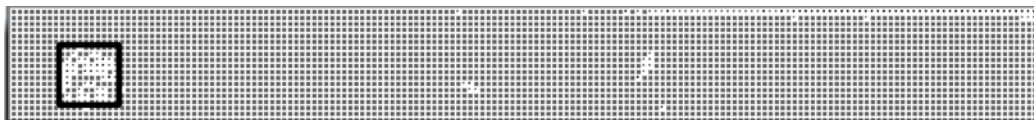isticated cell classification may require more computationally intensive, and therefore slow, analysis algorithms. Thus, the fast tracking algorithm described above could be performed for each frame to maintain a fast framerate; the slower classification algorithm would only need to be performed once (*e.g.*, on that cell's first frame in the imaging region).

To demonstrate the utility of our tracking algorithm, we used it to analyze live iPSC-RPE cells flowing through the device. Transplantation of RPE cells is a promising method for the treatment of age-related macular degeneration [176, 177], but therapeutic use requires highly pure populations of mature, fully-differentiated RPE cells, indicated by their degree of pigmentation. However, highly pure discrimination of pigmented versus unpigmented RPE cells is unfeasible using traditional FACS alone. We therefore used a pixel-based algorithm to classify RPE cells flowing through the SuperFACS device as either pigmented or unpigmented. To do this, we first used our contrast-based tracking algorithm to detect and track the cells as they flowed through the channel. For each cell image, we then counted the number of feature pixels within each cell that are brighter than the average background pixel value, as well as the number of pixels that are darker. By plotting the dark pixel count versus bright pixel count for each cell, we can define a dividing line differentiating pigmented cells from unpigmented cells (Figure 4.9). This simple algorithm requires further optimization and testing, but is a promising approach to perform image-based sorting of RPE cells in the future.
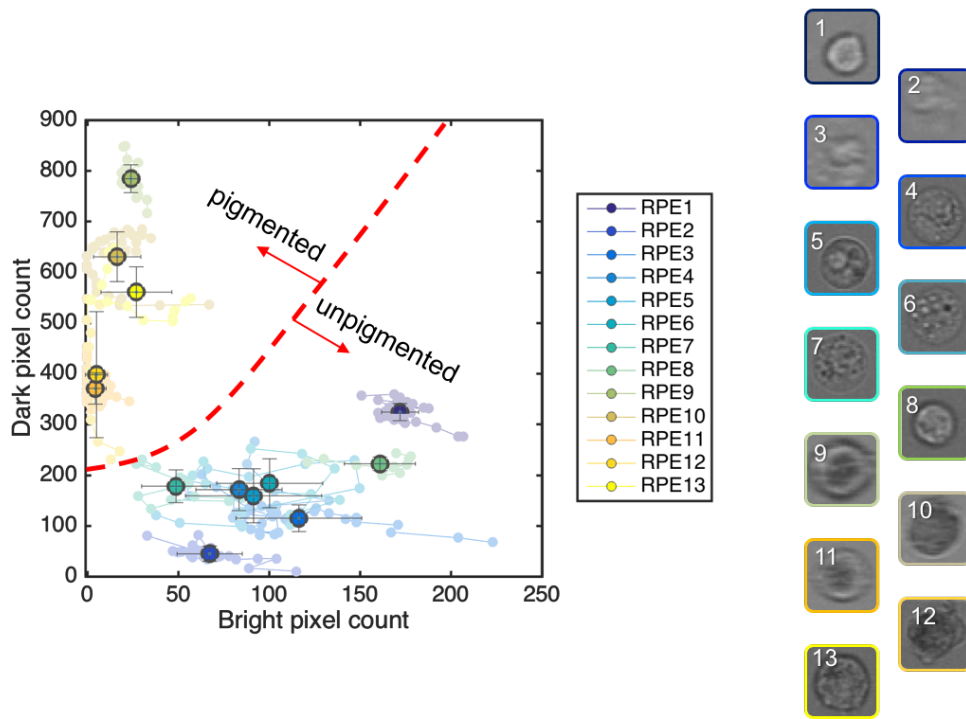
Figure 4.9: Pixel-based algorithm for classification of RPE cells based on pigmentation. Small faded circles indicate analysis of individual frames as the cell flowed through the channel, while large bright circles indicate the mean values for a given cell across all its frames (error bars indicate S.D.). A representative image for each numbered cell is shown on the right.

4.3.8   Discussion

In this work, we have showed promising preliminary results toward an image-based cell sorter. We demonstrated that the SuperFACS system's unique combination of microfluidic particle manipulation and real-time image processing enables image-based sorting of synthetic microparticles based on a variety of two-dimensional features. We also developed a novel object tracking algorithm to enable the analysis and sorting of a wide variety of cell types, and we demonstrated preliminary results for a pixel-based classification algorithm for iPSC-RPE cells. These proof-of-concept results should be followed up with a real-time sort of RPE cells based on pigmentation.

A critical performance metric for the SuperFACS system is its sorting throughput. The overall system sort rate depends on a number of limiting factors, including the image capture rate, image transfer rate, image analysis time, and actuator speed. The current throughput bottleneck is image analysis time, which takes roughly 5-10 ms per frame using our existing unoptimized algorithms. This currently limits our practical sorter throughput to a rate of < 100 objects/s. Future work utilizing dedicated image analysis hardware through an FPGA would be able to lower this analysis time by 2-3 orders of magnitude [158, 178]. Image transfer rate is also presently limited to about 250 fps; again, high-speed image transfer interfaces and dedicated image acquisition hardware (*e.g.*, a framegrabber FPGA) can increase this throughput 10-100 fold. As imaging and analysis rates are increased, the DEP actuator may not be able to deflect cells sufficiently quickly without applying large electric fields that could damage cell viability. To overcome this problem, we could employ gentler methods of cell manipulation capable of rapid switching, such as surface acoustic wave actuators [179, 180] that can actuate microparticles and cells at rates approaching 20,000 Hz. With all of these potential improvements combined, we estimate that a final sorter throughput of ~ 1000 cells/s

could be feasible.

One key limitation of the SuperFACS system in its current iteration is its inability to perform fluorescence imaging. Because of the very brief exposure times employed for high-speed imaging, we are currently limited to capturing brightfield images only; well-resolved fluorescence images would be impossible to obtain for all but the brightest fluorescent dyes. This problem could be addressed by utilizing high-gain image sensor techniques such as time-delay integration [153, 181], but such hardware-based techniques are difficult to implement on commercially available high-speed image sensors. Brightfield imaging still contains a wealth of phenotypic information —especially when "brightfield-visible" labeling strategies are used, such as antibody-conjugated high-contrast microparticles that bind to specific surface proteins on a cell of interest [182] —but the overall usefulness of the SuperFACS system will be limited without fluorescence imaging capabilities.

Another key challenge for image-based cell sorting is the determination of the ideal image analysis and classification criteria to use in order to enrich cells expressing the desired phenotype. While certain cases, such as RPE pigmentation, have an obvious visual phenotype on which sorting may be based, many other cellular systems have far more subtle differentiating features separating "target" and "non-target" cell types. Future work in image-based sorting should leverage recent advances in the field of high-speed imaging flow cytometry which have employed machine learning approaches to identify relevant image features for cell classification [147, 151, 182].

4.4   Conclusion

We have demonstrated promsing proof-of-concept results for image-based cell sorting, which has the potential to become a powerful tool for biological research, biotechnology, and biomedicine. By combining the rich information content of traditional microscopy

with the throughput and population-level data afforded by flow cytometry, image-based sorters could enable new insights into subtle cellular processes and new approaches to cellular therapeutics.

4.5   Experimental Methods

4.5.1   Chip fabrication and assembly

Microelectrodes were deposited on glass wafers (500-μm thick, 100 mm diameter) via contact lithography and electron beam deposition (200 Ti, 1800 Pt). The wafer was then diced to form individual glass substrates with electrodes. A master mold for the microfluidic flow channels was fabricated via contact lithography on a silicon substrate using SU-8 negative photoresist. Polydimethylsiloxane, or PDMS (Sylgard 184, Dow-Corning), was then mixed and poured over the mold. After being partially cured at 80 °C for one hour, we peeled the PDMS off of the mold and punched 1.5 mm diameter holes to form the sample sheath inlet, focusing sheath inlet, and outlets. A via to the sample injection port was formed using a 0.7 mm hole punch. The bottom (channel-imprinted) side of the PDMS and the top (electrode) surface of the glass substrate were both briefly exposed to an O_2 plasma (BD-20AC Laboratory Corona Treater, ETP Inc.). Immediately after, the plasma-treated PDMS and glass substrate were aligned using an inverted microscope to ensure that the electrode tips were located directly in the center of the microchannel $\sim$ 5 microns upstream of the sorting junction, and were subsequently placed into contact and cured for several hours at 80 °C, facilitating an irreversible covalent bond between the glass and PDMS. Finally, wires leading to a BNC connector were soldered to the electrode contact pads to allow for connection to the function generator.

4.5.2   Fluidic connections

Fluidic vias to the sample sheath inlet, focusing sheath inlet, and waste and collection outlets were formed via 1 cm lengths of 0.02" I.D. / 0.06" O.D. Tygon tubing (Saint-Gobain Performance Plastics). These vias were friction-fit into the ends of 20 cm lengths of 0.04" I.D. / 0.07" O.D. Tygon tubing, which ultimately were passed into the inlet reservoir (for the sample sheath and focusing sheath inlets) or the outlet reservoir (for the collection and waste outlets). The sample injection port was attached to a 5 cm length of 0.76-mm O.D. / 0.30-mm I.D. PTFE tubing (Cole-Parmer), which was filled with the suspension to be sorted and capped with a small plunger to enable injection into the chip. The inlet and outlet reservoirs contained deionized water.

4.5.3   Electronic instrumentation

The sorter chip's electrodes were connected to a high-frequency function generator (AFG320, Tektronix) and a custom-built power amplifier. In order to achieve maximum dielectrophoretic deflection at the electrodes, a DEP driving signal of 1 MHz at 34 V peak-to-peak amplitude was employed.

4.5.4   Microparticles and suspensions

Size-based sorting of spherical microparticles was performed using 8 and 13 μm diameter polystyrene microbeads (Fisher). Stretched polystyrene ellipsoids were produced in the same manner as was described in Chapter 3. All synthetic particles were suspended in deionized water containing 1% Tween 20 (Sigma Aldrich) as a surfactant. Particle suspensions were vortexed, sonicated, and passed through a 20 μm filter prior to use in the chip.

4.5.5   Cell protocols

MCF-7 cells for actuator testing were revitalized from liquid nitrogen storage and suspended in 1 mL of culture media containing Eagle's minimum essential medium (EMEM) supplemented with 10% fetal bovine serum (FBS) and 1% penicillin/streptomycin. All culture reagents were purchased from ATCC (Manassas, VA). Cells were then incubated in T-150 cell culture asks (Fisher Scientic) with 30 mL of culture media until they reached 90% conuence. The cells were washed with Dulbecco's phosphate-buered saline (DPBS; ATCC), released using 5 mL of trypsin/EDTA solution (ATCC), and then collected and pelleted via centrifugation at 400g for 10 min. Live cells were resuspended in 10 mL of EMEM. Retinal pigment epithelium cells produced from induced pluripotent stem cells (iPSC-RPE) were provided by Dr. Monte Radeke of the UCSB Neuroscience Research Institute.

Prior to sorting, cells were suspended in Dulbecco's modified Eagle medium (DMEM) at a concentration of 1×10^5 to 1×10^6/ml. Immediately prior to entering the chip, all cell suspensions were gently mixed with a 1 mL pipette and subsequently passed through a 20 μm filter.

Chapter 5

Contamination-Resistant Loop-Mediated Isothermal Amplification for Genetic Pathogen Detection

5.1 Introduction

[1] Rapid, sensitive, and specific genetic amplification methods have become an indispensable tool for a wide array of applications including disease diagnostics [183–185], food safety testing [186–188], and environmental monitoring [189, 190]. In particular, loop-mediated isothermal amplification (LAMP) [191] has emerged as a popular technique because of its sensitivity, specificity and isothermal reaction conditions, which obviate

---

[1]The first portion of this chapter was previously published in Hsieh, K., Mage, P.L., Csordas, A.T., Eisenstein, M., Soh, H.T. *Simultaneous elimination of carryover contamination and detection of DNA with uracil-DNA-glycosylase-supplemented loop-mediated isothermal amplification (UDG-LAMP).* **Chemical Communications** 50, 3747-9 (2014).

the need for specialized thermal cycling equipment [191, 192]. Unfortunately, LAMP's potent amplification mechanism, while making the assay highly sensitive, also renders it highly susceptible to carryover contamination, wherein amplified DNA products from previous LAMP reactions become templates for re-amplification that lead to false positive results [193]. Importantly, there is currently no effective means for eliminating LAMP carryover contamination. Thus, laboratories using LAMP can only rely on careful (and failure-prone) preventative methods, because once contamination occurs, the process of decontamination is costly and time-consuming, sometimes requiring a complete redesign of the assay.

Toward a strategy to eliminate carryover contamination, a number of groups have explored selective enzymatic digestion of contaminant amplicons (see references [194, 195] for extensive reviews). For example, the pioneering work by Longo and coworkers [196] utilized deoxyuridine triphosphate (dUTP) for polymerase chain reaction (PCR) amplification, such that all amplicons incorporated uracil bases. Prior to performing subsequent PCR reactions, any uracil-containing PCR amplicons from previous reactions (*i.e.*, carryover contaminants) were digested with uracil-DNA-glycosylase (UDG) [197], an enzyme that specifically removes uracil bases in uracil-containing DNA but has no effect on natural, thymine-containing DNA [197, 198]. This enzyme degraded uracil-containing PCR amplicons from previous reactions, preventing them from amplifying while leaving only the target DNA intact for amplification. Crucially, this assay is effective because it is a one-pot reaction that can be performed in a closed-tube vessel; it is well known that opening the reaction vessel during the amplification reaction dramatically increases the risk of reintroducing contaminants from the environment [193].

Recently, He and co-workers have shown that dUTP can also be incorporated into LAMP reactions and that UDG can be used to degrade uracil-labeled LAMP amplicons in a similar manner to PCR [199, 200]. Unfortunately, the assay requires UDG digestion and

LAMP amplification to be performed in separate reactions, which necessitates opening the reaction vessels and exposing them to carryover contaminants in the environment. This key limitation has prevented the translation of this method into a practically useful assay.

5.2   Results and Discussion

5.2.1   Overview of UDG-LAMP Assay

Motivated by this critical unmet need, we report the first integration of LAMP amplification with UDG digestion in a one-pot, closed-vessel reaction to eliminate false-positive results arising from carryover contaminants. Our uracil-DNA-glycosylase-supplemented LAMP (UDG-LAMP) assay requires only two additional components relative to conventional LAMP and eliminates carryover contamination in two stages. In the first stage, we add dUTP into all LAMP reaction mixtures so that uracil is incorporated into the amplicons (Figure 5.1; stage 1). To enhance dUTP incorporation, which is critical to the success of this method, we have replaced the Bst DNA polymerase commonly used in conventional LAMP reactions with Bst 2.0 DNA polymerase [201]. In the second stage, which applies to all subsequent reactions, we perform UDG digestion and the LAMP reaction in a one-pot process. Specifically, prior to amplification, we treat the reaction mixture with a heat-labile UDG enzyme [202, 203] (Figure 5.1; stage 2) at room temperature for 5 minutes. The UDG enzyme selectively cleaves uracil bases from any contaminating LAMP amplicons, leaving behind abasic sites [204], while uracil-free target DNA remains completely unaffected. In the immediately ensuing LAMP reaction, these abasic sites block replication by DNA polymerases and cause rapid degradation of the carryover contaminants via hydrolysis at the phosphate backbone [196, 205], effectively
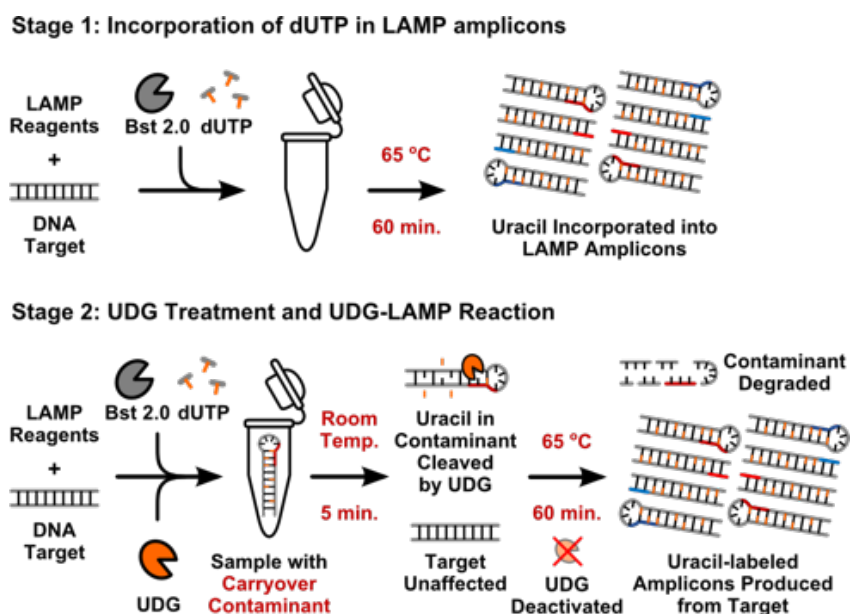
Figure 5.1: Overview of uracil-DNA-glycosylase-supplemented loop- mediated isothermal amplification (UDG-LAMP). UDG-LAMP eliminates carryover contamination in two stages. First, all LAMP reactions are performed in the presence of dUTP and Bst 2.0 DNA polymerase, such that all amplicons contain uracil bases. All subsequent LAMP reactions are then treated with UDG to eliminate carryover contaminants by specifically removing uracil from amplified products from previous LAMP reactions, while having no effect on natural DNA. During the LAMP reaction, the digested contaminants are degraded and the UDG enzyme is heat-inactivated, ensuring that only the target is amplified.

preventing them from re-amplification.

Critically, the use of our heat-labile UDG enables the UDG-LAMP assay to be performed in a single closed vessel, because the enzyme is rapidly and automatically deactivated when the LAMP reaction is performed at an elevated temperature (i.e., °65 C). In this way, genuine amplicons subsequently produced from the target during the reaction are not digested, allowing amplification to proceed normally (Figure 5.1; stage 2). Finally, once amplification is complete, amplicons from the UDG-LAMP reaction can be detected with standard methods such as gel electrophoresis and fluorescence. Here, we used commercially available calcein fluorescence reagents to detect UDG-LAMP amplicons in a closed-tube fashion, further ensuring a contamination-free read-out of the reaction [193].

Samples that have undergone amplification exhibit strong calcein fluorescence that is directly observable under ambient light or UV irradiation.

5.2.2   LAMP with dUTP and Bst 2.0 DNA polymerase

To demonstrate the utility of UDG-LAMP, we used the assay to detect genomic DNA from Salmonella enterica serovar Typhimurium (S. Typhimurium), a bacterial pathogen that causes food poisoning, using a pre-existing set of six primers that target the invA gene [206] (see Methods for primer sequences). We first confirmed that robust LAMP reactions could be achieved with Bst 2.0 DNA polymerase incorporating dUTP into LAMP amplicons in the presence of the UDG enzyme. To test this, we added either dUTP alone or both dUTP and UDG to the reaction mixture (see Methods for details), along with 2104 copies of purified S. Typhimurium genomic DNA as target. After incubating the reaction for 60 minutes at 65 °C, we observed strong calcein fluorescence in both target-containing reaction tubes under UV illumination, confirming that both samples amplified successfully with Bst 2.0, even in the presence of the UDG enzyme (Figure 5.2A).

5.2.3   UDG digestion of carryover contaminant

We next verified that UDG is capable of digesting carryover contaminants with high efficiency. To demonstrate this, we performed a UDG-free LAMP reaction supplemented with dUTP, and then added between 100 zeptograms (1×10^{-19} g) and 1 femtogram (1×10^{-15} g) of amplicon DNA from this reaction into a new set of target-free UDG-LAMP reactions to simulate carryover contamination. In parallel, we also added the same amounts of contaminants to a set of LAMP reactions without UDG as controls. We estimated the amount of carryover contaminants by mass because LAMP reactions produce
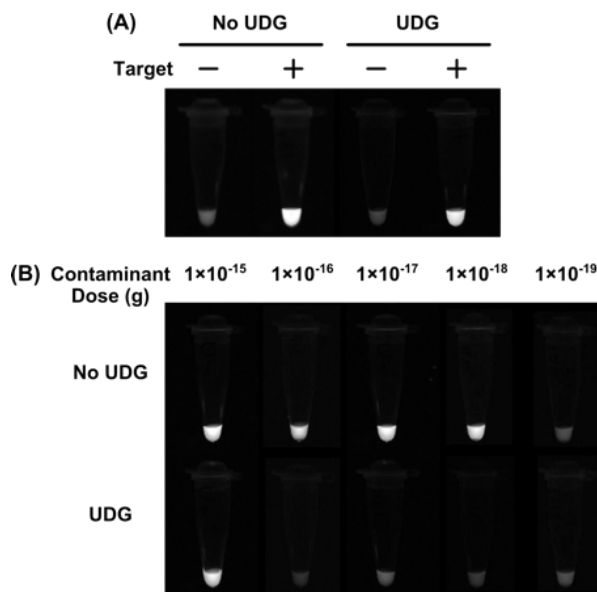
Figure 5.2: Addition of UDG preserves robust LAMP reactions and achieves effective digestion of carryover contaminants. (**A**) Bst 2.0 DNA polymerase successfully incorporated dUTP into amplicons both in the presence and absence of UDG, as indicated by the bright calcein fluorescence from the reaction mixture. Control reactions with no target DNA exhibited minimal fluorescence. (**B**) UDG-free reactions yielded amplification from as little as 1 attogram of carryover contaminants (top row). In contrast, UDG treatment effectively eliminated such amplification, even at 100-fold higher contaminant concentrations (bottom row).

amplicons of various lengths, rendering a priori estimates of copy number impractical (see Methods for calculation).

In samples without UDG, we observed amplification from as little as 1 attogram of carryover contaminant (Figure 5.2B, top row). This demonstrates that a source contaminant equivalent to a 0.2μm-diameter aerosol droplet (4×10^{-18} L) —which cannot be efficiently blocked by fibrous pipette tip filters [207, 208] —was sufficient to contaminate new reactions. These results clearly illustrate the danger of carryover contamination in LAMP reactions, where even miniscule amounts of contaminant can produce unwanted amplification. In contrast, UDG prevented amplification of up to 100-fold higher concentrations of carryover contaminant DNA (Figure 5.2B, bottom row), and calcein fluorescence was only observed in the sample containing the highest tested dose of contaminants

(1 femtogram DNA).

5.2.4   UDG prevents false-positive amplifications

Finally, we show that UDG-LAMP can significantly reduce false-positive results due to carryover contaminants. To do so, we set up UDG-free LAMP reactions and UDG-LAMP reactions with and without target DNA, and deliberately doped these samples with ~ 10 attograms of carryover contaminant amplicons, simulating a moderate level of contamination (*e.g.*, resulting from multiple aerosol droplets too small to be sequestered by pipette tip filters). Without UDG, we observed fluorescence in the no-target negative control sample (Figure 5.3A, left), yielding a false-positive signal indistinguishable from true positive signals obtained in the presence of target DNA. In contrast, UDG-LAMP eliminated these false positives, and we could clearly distinguish the negative control from samples containing as little as 4×10^3 copies of target DNA (Figure 5.3A, right). This difference is even more striking in gel electrophoresis results, where the strong false-positive amplicon bands arising from contaminant amplification products in the no-UDG sample (Figure 5.3B, lane 1) is virtually eliminated with UDG-LAMP (lane 4).

5.2.5   Extending UDG-LAMP to achieve contamination-resistant real-time LAMP

Recent advancements in real-time LAMP assays [201, 209–214] offer quantitative target copy-number information that is useful for accurate disease diagnoses. Unfortunately, carryover contamination produces false products that can overwhelm the true products generated from the target DNA, giving rise to inaccurate results in copy number. At present, there is no effective means for eliminating LAMP carryover contamination in real-time LAMP assays. We therefore sought to extend our UDG-LAMP strategy to con-
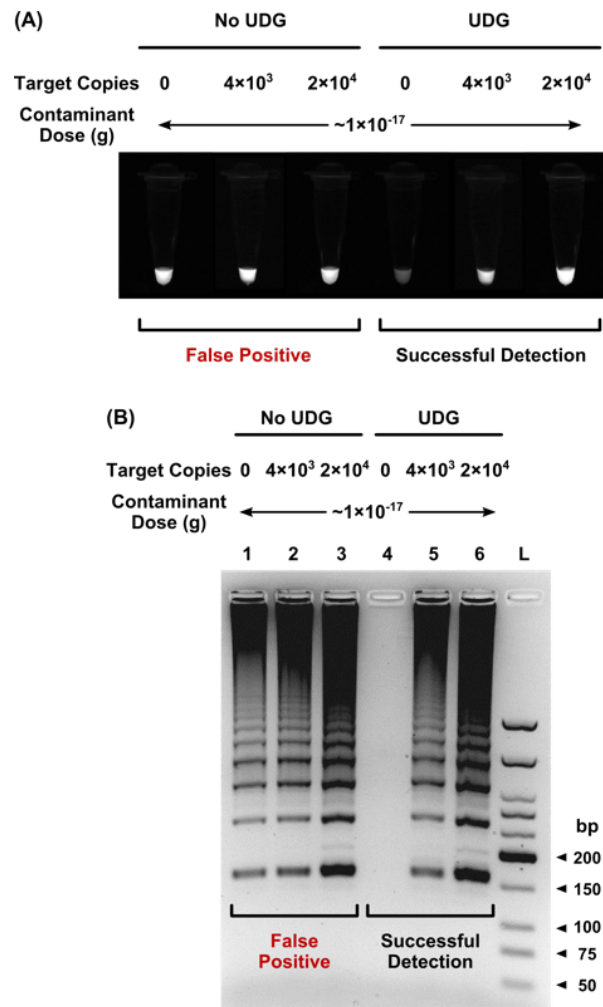
Figure 5.3: UDG-LAMP reduces false-positive detection due to carryover contamination. (**A**) In the presence of 10 attograms of contaminant DNA, a target-free standard LAMP reaction (left) generates a fluorescent signal indistinguishable from that generated by samples containing 4×10^3 or 2×10^4 copies of target DNA. In contrast, UDG treatment (right) eliminates this false-positive signal, restoring the accuracy of the assay. (**B**) Gel electrophoresis clearly demonstrates the effectiveness of UDG-LAMP in eliminating false-positives, with virtually no amplification detected in a contaminant DNA-only sample (lane 4).

fer contamination resistance to real-time LAMP assays. Our Contamination-Resistant Real-time LAMP (CORR-LAMP), the first real-time LAMP assay that is immune to carryover contamination, combines UDG-LAMP with real-time amplification monitoring based on DNA-intercalating reporters, leveraging a detection approach that has been widely-adopted in both fluorescent [215] and electrochemical [216] real-time monitoring of LAMP reactions. In doing so, CORR-LAMP can discriminate DNA samples with different copy numbers even in the presence of substantial amounts of carryover contamination (Figure 5.4A). As a further benefit, we have integrated the entire CORR-LAMP assay onto a multiplexed microfluidic device such that multiple samples can be processed simultaneously with excellent reproducibility.

Our CORR-LAMP integrates electrochemical real-time LAMP [217–222] with UDG treatment (Figure 5.4B). As in UDG-LAMP, CORR-LAMP incorporates dUTP into the LAMP reaction so that all amplification products contain uracil bases, and at the beginning of each reaction, any uracil-tagged carryover contaminants from previous reactions are digested away by the UDG enzyme (Figure 5.4B, left). We then initiate the LAMP reaction with a DNA-intercalating electrochemical reporter (methylene blue, MB) added to the sample. In the initial phase of the amplification, MB molecules freely diffuse and transfer electrons to the gold working electrode in the device, producing a high redox current. Importantly, because the reaction is performed at 66 °C, the thermally labile UDG enzyme is automatically deactivated, which prevents digestion of dUTP-containing amplicons produced from the target DNA. As the amplification progresses, more MB molecules intercalate into the double-stranded LAMP amplicons, thereby decreasing the electrochemical current at the working electrode (Figure 5.4B, right). We continuously monitor the MB redox current throughout the reaction; when this current is plotted as a function of time, a successful amplification is indicated by a sigmoidal decrease in current [218].
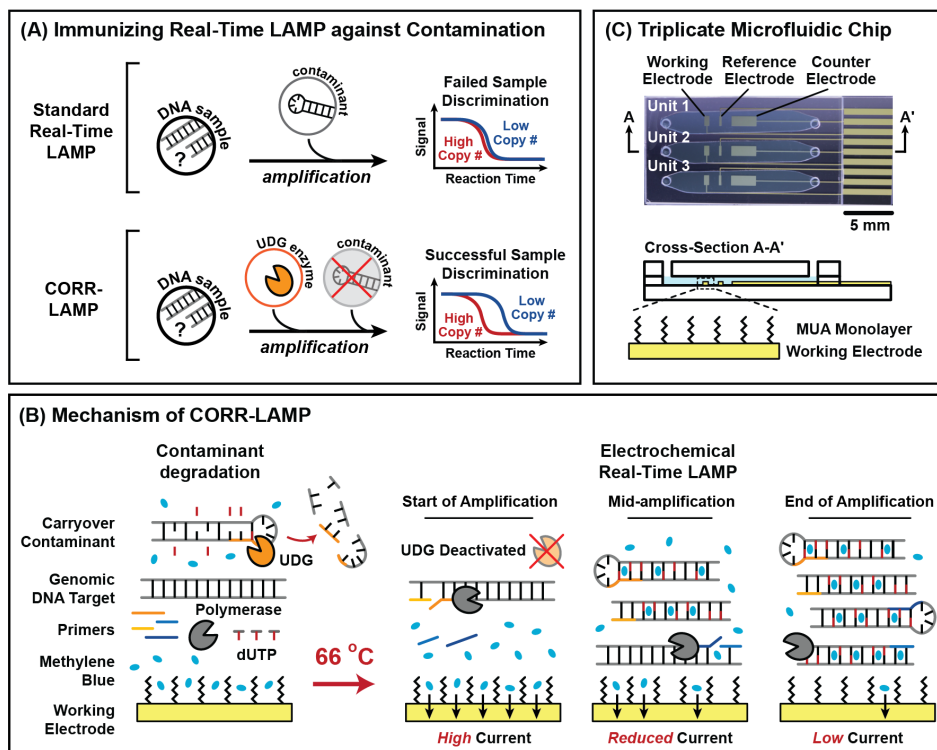
Figure 5.4: (**A**) Carryover contamination prevents accurate discrimination between samples with different copy numbers of target DNA (top). CORR-LAMP can accurately discriminate samples containing different copy numbers of target DNA, even with carryover contamination (bottom). (**B**) CORR-LAMP integrates electrochemical real-time LAMP with enzymatic digestion of carryover contaminants in a "one-pot" assay. As in UDG-LAMP, the assay incorporates dUTP into the LAMP reaction to chemically differentiate amplicons from natural target DNA. At the beginning of the reaction, the UDG enzyme digests uracil-containing amplicons while leaving natural target DNA untouched. The reaction mixture is then heated to the LAMP reaction temperature (i.e., 66 °C), at which point the heat-labile UDG is automatically deactivated and LAMP amplification commences. As amplification progresses, more MB molecules intercalate into the double-stranded LAMP amplicons and become less efficient at transferring electrons at the working electrode in the device. Amplification is indicated by a sigmoidal decrease in current when plotted as a function of time. (**C**) CORR-LAMP is performed in a sealed microfluidic device with three identical but independent reaction chambers to enable simultaneous triplicated measurements. The electrodes are coated with a thermally-stable monolayer of 11-mercaptoundecanoic acid (MUA) that facilitates stable MB current measurements.

In addition to digestion of contaminants, the CORR-LAMP assay is designed as a "one-pot" reaction and is performed in a sealed microfluidic device, which further avoids re-exposing the sample to contaminants during the reaction. Our device integrates three reaction chambers, each equipped with a set of microfabricated electrodes (Figure 5.4C). This design allows us to obtain triplicate measurements from a sample in a single run (or to include internal positive and negative controls, though not used as such in the current work). To protect the electrodes from potential non-specific adsorption of MB [223], we coat the electrodes with a monolayer of 11-mercaptoundecanoic acid (MUA). Notably, this thermally stable monolayer [224, 225] remains intact even at high temperatures, thus enabling accurate and reproducible electrochemical real-time measurements. After loading the sample, primers, and reagents into the device, we incubate the mixture at room temperature for 5 minutes to allow complete UDG digestion of carryover contaminants. We then heat the device to 66 °C to commence the LAMP reaction while simultaneously initiating a series of electrochemical measurements to achieve real-time detection.

5.2.6   CORR-LAMP assay validation

We first demonstrated robust target amplification and electrochemical real-time monitoring in CORR-LAMP by analyzing a contamination-free sample containing 2×10^4 copies of the S. Typhimurium genomic DNA. This reaction yielded a sigmoidal decrease in the time-course current trace over the course of amplification as expected (Figure 5.5a, red), signaling successful production of LAMP amplicons that led to intercalation of MB into the amplicons, as previously observed [218]. In contrast, a no-target control yielded no such decrease in current (Figure 5.5a, black), and produced a small background drift, presumably due to weak interaction between MB and single-stranded LAMP primers [226–228] and/or gradual dissociation of MB initially entrapped in MUA

(a) The CORR-LAMP sample with 2×10^4 copies of S. Typhimurium genomic DNA produces a sigmoidal-shaped decrease in the time-course current trace (red). This indicates successful production and detection of uracil-tagged LAMP amplicons. In contrast, the no-target control produces no amplicons and thus yields a small, background drift (black).

(b) Real-time LAMP reactions containing S. Typhimurium genomic DNA target without (black current trace) and with UDG (red current trace) show comparable target amplification, as both reactions yield similar amplification-specific, sigmoidal decrease in the MB redox current traces. The similar current traces indicate that UDG does not affect the LAMP reaction efficiency and that UDG is effectively de-activated during the LAMP reaction.
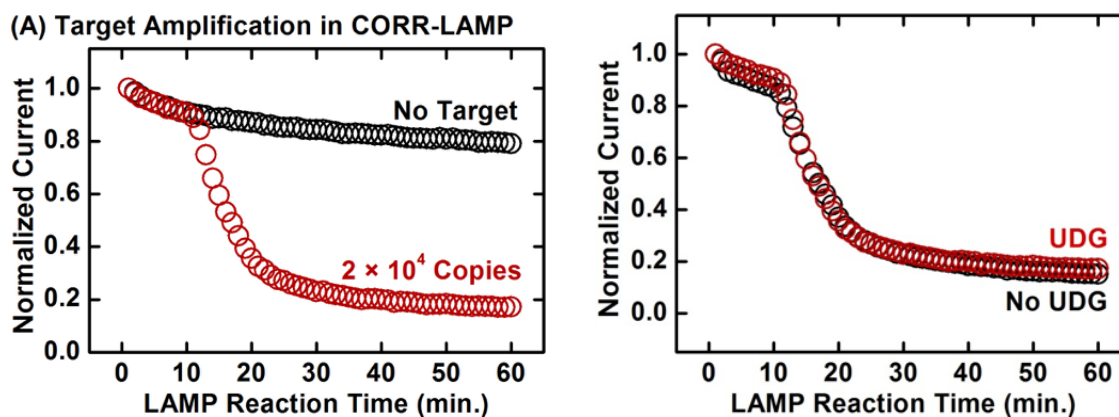
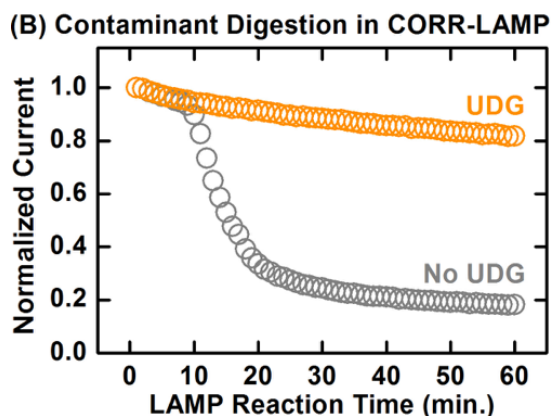Figure 5.5: Target amplification in CORR-LAMP

Figure 5.6: The UDG enzyme in the CORR-LAMP reaction effectively digests carryover contaminants that deliberately doped into the reaction mixture, preventing false-positive amplification (orange). This is evident by the current trace that is virtually indistinguishable from a reaction performed without contaminants or targets. In contrast, the reaction without UDG results in a false-positive as shown by the current decrease due to amplification of contaminants (gray).

monolayer [223, 229]. Importantly, we confirmed that the addition of UDG did not affect the efficiency of LAMP, as the reactions containing the same copy number of DNA target performed with and without UDG yielded similar current traces (Figure 5.5b). This result also indicates that the UDG is effectively de-activated during the LAMP reaction if this were not the case, UDG would digest the amplicons and there would be no sigmoidal decrease in the current trace.

The UDG enzyme can efficiently digest the carryover contaminants, preventing false-positive amplifications. To demonstrate this, we compared two "contaminated," no-target control reactions either with or without UDG treatment. Specifically, we deliberately doped ~ 10 attograms of carryover contaminants to both reaction mixtures, again representing a moderate level of contamination typically carried by aerosol droplets. The reaction without UDG resulted in false-positive results as shown by the current decrease caused by the amplification of the contaminants (Figure 5.6, gray), which is similar to the results obtained with target DNA. In contrast, the incorporation of UDG effectively prevented false positive amplification (Figure 5.6, orange), resulting in current traces

that were virtually indistinguishable from a reaction performed without any templates (i.e., either contaminants or targets).

5.2.7   CORR-LAMP enables copy number discrimination in contaminated samples

Towards a fully quantitative, contamination-resistant LAMP assay, we performed a proof-of-concept experiment to test whether CORR-LAMP can discriminate samples with different amounts of target DNA in the presence of carryover contamination. Specifically, we prepared two contaminated samples containing either a low dose (4×10^3 copies) or high dose (2×10^4 copies) of target DNA. We then compared CORR-LAMP with standard real-time LAMP (without UDG). Without UDG, it was not possible to distinguish between the two samples containing different copy numbers of target DNA, as they yielded essentially indistinguishable current traces (Figure 5.7A, left). In contrast, CORR-LAMP yielded two distinct current traces from the two contaminated samples (Figure 5.7A, right); the sample containing the higher dose of target DNA (Figure 5.7A, right, red) took shorter time to accumulate sufficient amplicons and cause the sigmoidal decrease in current than the sample containing the lower dose of target DNA (Figure 5.7A, right, blue), as expected.

Finally, we utilized the "time-to-threshold" (t_{TH}) metric [218] to discriminate the relative amount of target DNA in the contaminated samples. The t_{TH} is defined as the time point at which amplification is most efficient in a reaction, and it is obtained by locating the local minimum in the current derivative trace (dI/dt), where the MB current decreases most rapidly. Furthermore, we obtained triplicate measurements from our microfluidic device for each of the four samples (low or high target dose, with or without UDG), and calculated the mean and standard deviation of the t_{TH} values (Figure

5.7B). The two samples amplified without UDG yielded statistically indistinguishable t_{TH} values of 12.3 ± 0.6 min for the high-dose sample and 11.7 ± 0.6 min for the low-dose sample (Figure 5.7B, left), confirming that quantitative discrimination of contaminated samples is not possible due to the carryover contamination (likely because the carryover contaminant had become the more "dominant" amplification template relative to the target). In contrast, CORR-LAMP resulted in a large, statistically significant difference in t_{TH} values: 14.3 ± 2.5 min for the high dose sample and 25.3 ± 2.3 min for the low dose samples (Figure 5.7B, left), demonstrating the potential of CORR-LAMP to discriminate between samples with different copy numbers of target DNA even when contaminated.

5.3   Conclusion

In sum, we report the first integration of LAMP amplification with UDG digestion in a one-pot, closed-vessel reaction to greatly reduce false-positives from carryover contaminants. As a demonstration, we used UDG-LAMP to detect genomic DNA from the pathogen S. Typhimurium, and showed that we can readily eliminate false-positives arising from volumes of contaminant DNA equivalent to the aerosol droplets that may be encountered in a typical diagnostic or experimental setting. Currently, our limit of detection is approximately $\sim$4000 copies of target DNA in the presence of 10 attograms of carryover contaminants. Although this is a useful limit of detection, it nevertheless suggests some inhibition of LAMP by the UDG enzyme. We believe we can further improve the limit of detection by taking measures to reduce UDG inhibition of amplification. This could be achieved by adjusting the dose of UDG, adding a UDG-inactivation step at an intermediate temperature prior to initiating the LAMP reaction, or exploring alternative UDG enzymes that may be more susceptible to thermal deactivation. With these improvements to detection sensitivity, and with the demonstrated contamination elimina-
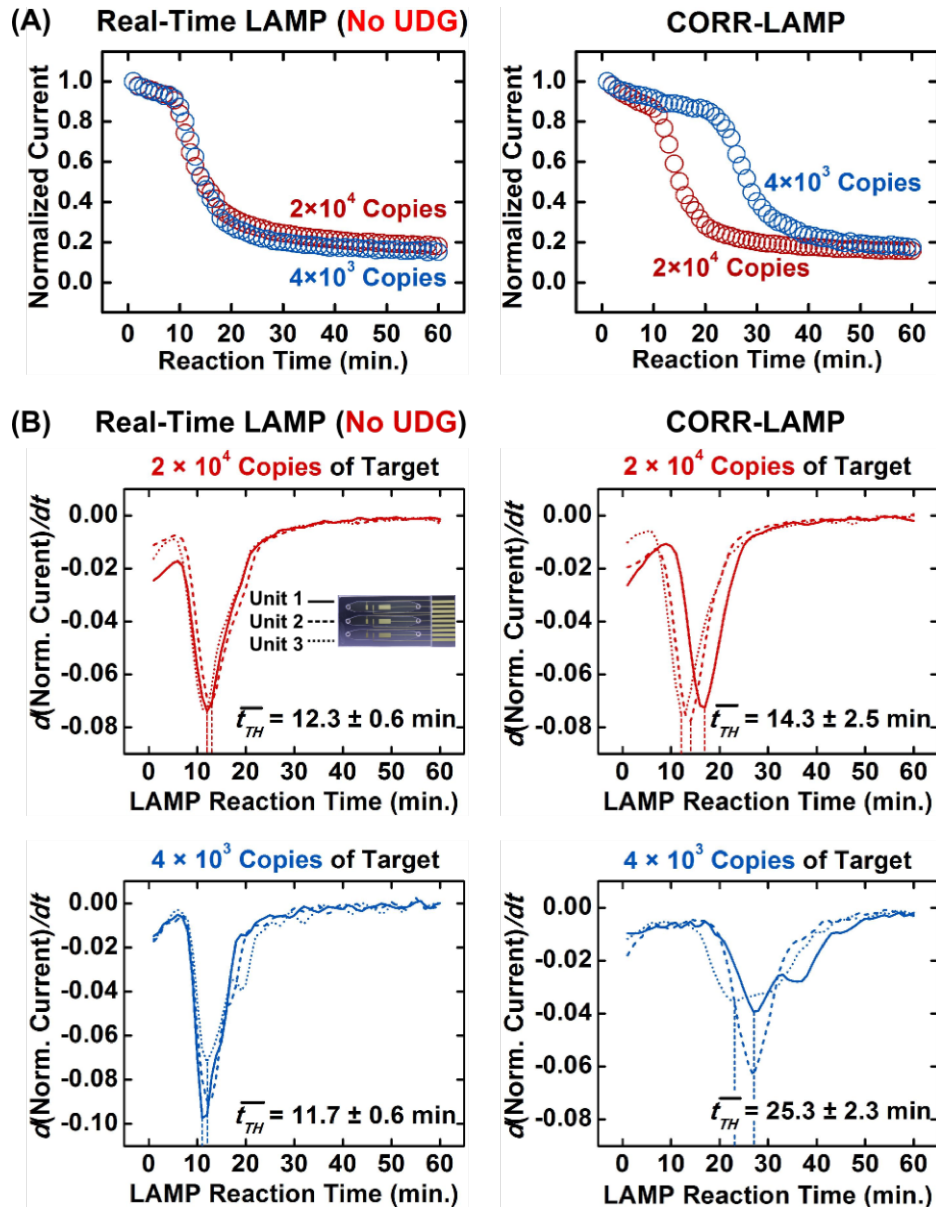
Figure 5.7: CORR-LAMP can discriminate samples with different amounts of target DNA in the presence of carryover contamination (**A**) Without UDG treatment, carryover contamination prevents real-time LAMP from discriminating between samples with different amounts of target DNA. In contrast, CORR-LAMP successfully discriminates these two samples, resulting in clearly distinct current traces for the samples with high and low doses of target DNA (right). (**B**) When analyzed by real-time LAMP without UDG treatment, contaminated samples with different target copy numbers yielded statistically indistinguishable t_{TH} values, confirming that quantitative detection of target in contaminated samples is impossible without UDG (left column). In contrast, CORR-LAMP enables statistically significant discrimination of contaminated samples with different target copy numbers (right column). t_{TH} for each current derivative trace is indicated by a vertical line, and overall t_{TH} for each sample is reported as mean $\pm$ S.D.   109

tion capability of our assay, we believe UDG-LAMP has the potential to greatly expand the utility of LAMP-based target detection in a wide variety of laboratory and point-of-care settings. We further demonstrated a strategy to address the unsolved problem of obtaining copy-number information for target DNA in a sample laced with carryover contamination. We achieved this by integrating real-time electrochemical detection with UDG treatment in a "one-pot" reaction, which can be performed in a sealed microfluidic device that offers highly reproducible, triplicate results in a single experiment. As a demonstration, we used our system to quantitatively discriminate samples that contain 2×10^4 and 4×10^3 copies of genomic DNA of a bacterial pathogen, which were laced with a substantial amount (10 attograms) of carryover contaminants.

This ability to discriminate between contaminated samples with varying amounts of target DNA is a crucial first step toward contamination-resistant DNA quantitation, but a number of improvements must be made to develop CORR-LAMP into a reliable, fully quantitative real-time assay. First, a calibration curve needs to be developed by measuring the t_{TH} for a number of samples containing a broader range of known initial target DNA copy numbers (as reported by Mori *et al.* [209]), enabling the determination of target copy number for samples with unknown quantities of target DNA based solely on t_{TH} measurement. Second, the calibrated CORR-LAMP assay should be validated by analyzing samples using a well-characterized secondary measurement technique such as real-time quantitative PCR. Finally, the impact of varying amounts of contaminant should be evaluated to ensure robust assay performance under a variety of environmental conditions. The success of these improvements could pave the way for robust and quantitative genomic detection methodology, which is "immune" to carryover contamination, and they are topics of current investigations.

5.4   Experimental Methods

5.4.1   Materials and Reagents.

LAMP reaction reagents, including Loopamp DNA Amplification Kit and Loopamp Fluorescent Detection (FD) Reagent, were purchased from SA Scientific (San Antonio, TX). LAMP DNA primers were ordered from Integrated DNA Technologies (Coralville, IA). Bst 2.0 DNA polymerase and low molecular weight DNA ladder were obtained from New England Biolabs (Ipswich, MA). Cod uracil-DNA-glycosylase (UDG) was purchased from ArcticZymes (Plymouth Meeting, PA). 2'-deoxyuridine-5'-triphosphate (dUTP) sodium salt was acquired in the form of a 100 mM solution from Affymetrix (Santa Clara, CA). Nuclease-free water (not DEPC-treated) and TE buffer (10 mM Tris and 1 mM EDTA, pH 8.0) were purchased from Life Technologies (Carlsbad, CA). Purified Salmonella enterica serovar Typhimurium genomic DNA was acquired from ATCC (Manassas, VA) and reconstituted in-house in TE buffer at 20 ng/L, as measured by a NanoDrop 1000 Spectrophotometer (Thermo Fisher Scientific, Wilmington, DE). Agarose (Low-EEO/Multi-Purpose/Molecular Biology Grade) was purchased from Fisher BioReagents (Fair Lawn, NJ) and TBE buffer (0.089 M Tris base, 0.089 M boric acid (pH 8.3) and 2 mM Na$_2$EDTA) was purchased from National Diagnostics (Atlanta, GA). GelStar nucleic acid gel stain was obtained from Lonza (Basel, Switzerland). Reagent-grade chemicals, including 11-mercaptoundecanoic acid (MUA), sulfuric acid (H2SO4), and methylene blue (MB) were purchased from Sigma-Aldrich (St. Louis, MO) and used without further purification.

5.4.2   Primer sequences for S. Typhimurium

Each primer is shown with its sequence (5' to 3'):

FIP: GACGACTGGTACTGATCGATAGTTTTTCAACGTTTCCTGCGG

BIP: CCGGTGAAATTATCGCCACACAAAACCCACCGCCAGG

F3: GGCGATATTGGTGTTTATGGGG

B3: AACGATAAACTGGACCACGG

FL: GACGAAAGAGCGTGGTAATTAAC

BL: GGGCAATTCGTTATTGGCGATAG

5.4.3   UDG-LAMP Reaction Assembly.

The reaction mix was assembled in a laminar flow hood in a laboratory separate from where the amplification and the detection steps were performed to prevent unwanted carryover contamination. A typical UDG-LAMP reaction mix (9 L) contained the following: 1 Loopamp DNA Amplification Reaction Mix (20 mM Tris-HCl, 10 mM KCl, 8 mM MgSO4, 10 mM (NH4)2SO4, 0.1% Tween20, 0.8 M betaine, and 1.4 mM dNTP), 1.4 mM dUTP (1:1 dUTP-to-dTTP ratio), 0.2% BSA, 3.2 M each of FIP and BIP primers, 0.4 M each of F3 and B3 primers, 0.8 M each of LF and LB primers (see Supporting Information Table S1 for sequences), 0.36 L FD reagent, 0.64 U/L Bst 2.0 DNA polymerase, 0.005 U/L UDG, 0.5 L genomic target DNA diluted from the stock with TE buffer to obtain the desired concentration, and 0.4 L contaminant DNA diluted from previous LAMP reactions with TE buffer to obtain the desired concentration. Of note, during the reaction assembly, the reagents were kept cold with a 96-well PCR cold block (Eppendorf, Hauppauge, NY). Also, the two enzymes were added only after the other reagents had been assembled and well mixed (except for targets and contaminants) in order to ensure the activity of these enzymes. Finally, contaminant DNA was added in a

fume hood in a separate laboratory to prevent exposing the reaction preparation facility with unwanted carryover contamination.

5.4.4   Fabrication of CORR-LAMP Microfluidic Chips

CORR-LAMP chips were assembled from three modular, separately fabricated layers —the gold electrode substrate, the chamber layer, and the fluidic via substrate —similar to previously described methods [218]. For the gold electrode substrate, working, reference, and counter electrodes were microfabricated on a 4-inch-diameter, 650-μm-thick Borofloat glass wafer (Mark Optics, Santa Ana, CA) through a standard lift-off process. The lift-off process began with transparency mask (CAD/Art Services, Bandon, OR) based contact photolithography, followed by electron-beam evaporation-based metal deposition (180 nm of gold on 20 nm titanium for adhesion) in a VES 2550 evaporation chamber (Temescal, Livermore, CA), and concluded with immersion and gentle sonication in acetone. The chamber layer was formed from a 0.01-inch-thick PDMS sheet (BISCO Silicones, Rogers Corporation, Carol Stream, IL) with the channel design cut using a programmable sign-cutting tool (CE5000-60, Graphtec, Santa Ana, CA). For the fluidic via substrate, eyelet holes were drilled through a second Borofloat glass wafer with a 0.75-mm-diameter diamond drill bit (Triple Ripple, Abrasive Technology, Lewis Center, OH) using a programmable CNC milling machine (Flashcut CNC, San Carlos, CA). The electrode wafer and fluidic via substrate were diced (7100, Advanced Dicing Technologies, Horsham, PA) into individual chips prior to assembly. The three modular layers were manually assembled in a fume hood. During the assembly, one side of the PDMS chamber layer was corona treated with a hand-held high-frequency emitter (BD-20AC, Electro-Technic Products, Chicago, IL) for approximately 3 seconds before bonding to the fluidic via substrate. This assembly was allowed to rest for several min-

utes to ensure strong bonding between PDMS and glass. Subsequently, the other side of the PDMS was corona treated and bonded to the electrode substrate to finish device assembly. The complete chip measured 25 mm 11 mm and harbored three individual chambers, each with an approximate volume of 9 μL and housed an independent set of working, reference, and counter electrodes.

The gold working electrode in each chamber of the chip was cleaned with 50 mM H_2SO_4 via cyclic voltammetry, with twelve potential sweeps ranging from -0.5 to 1.3 V (with respect to the gold reference electrode in the chamber) applied at 0.1 V s^{-1} with a sample interval of 0.001 V and 10 μA sensitivity, readying it for surface passivation. After a brief rinse with deionized (DI) water to wash away H_2SO_4, the gold electrodes were passivated with 10 mM MUA (dissolved in absolute ethanol) for 2 hr. After this passivation step, each chamber was immediately rinsed three times with DI water before the CORR-LAMP reaction mix was loaded. Of note, in contrast to the 6-mercapto-1-hexanol (MCH) monolayer employed in the Soh Lab's previous work [218], the MUA monolayer obviates the high-temperature annealing step to remove defects in the monolayer, thus simplifying the chip preparation process.

5.4.5   Assembly of CORR-LAMP Reactions

The reaction was assembled within a laminar flow hood in a separate laboratory to prevent unwanted carryover contamination. Typical reaction mix (9 μL) contained the following: 1x Loopamp DNA Amplification Reaction Mix (20 mM Tris-HCl, 10 mM KCl, 8 mM $MgSO_4$, 10 mM $(NH_4)_2SO_4$, 0.1% Tween20, 0.8 M betaine, and 1.4 mM dNTP), 1.4 mM dUTP, 0.2% BSA, 3.2 μM of each FIP and BIP primers, 0.4 μM of each F3 and B3 primers, 0.8 μM of each LF and LB primers (see Table S1 for primer sequences), 10 μM MB, 0.64 U/μL Bst2.0 DNA polymerase, 0.005 U/μL UDG, 0.5 μL genomic

target DNA diluted from the stock with TE buffer to obtain the desired concentration, and 0.4 μL simulated contaminant DNA diluted from previous LAMP reactions with TE buffer to obtain the desired concentration. Of note, during the reaction assembly, the reagents were kept cold with a 96-well PCR cold block (Eppendorf, Hauppauge, NY). Also, the two enzymes were only added after other reagents have been assembled and well mixed (except for targets and contaminants) in order to ensure their optimal activities. Finally, simulated contaminant DNA was added in a fume hood in a separate laboratory to prevent exposing the reaction preparation facility with unwanted carryover contamination.

5.4.6   Dose Estimation for Carryover Contamination.

The mass yield of the LAMP reaction generated from 1×10^3 copies of target in the absence of UDG, which served as the source of carryover contaminants, was conservatively estimated to be 0.25 g/L, as typical LAMP reactions can generate up to 0.4 to 0.8 g/L of DNA amplicons. This source reaction was diluted by 1×10^8 to 1×10^{12}-fold and 0.4 L of the diluted product was spiked in each UDG-LAMP reaction. The mass of carryover contaminant therefore corresponds to approximately 1×10^{-15} to 1×10^{-19} g.

5.4.7   UDG-LAMP Reaction Conditions and Detection.

UDG-LAMP reactions were conducted in standard Eppendorf PCR tubes and in a bench-top thermocycler (DYAD 220 Peltier Thermal Cycler, MJ Research, Inc., Waltham, MA), first at 25 °C for 5 min and then at 65 °C for 60 min. Upon completion of the reaction, each sample was immediately evaluated without opening the reaction tube. Although calcein fluorescence can be clearly observed by naked eye under ambient light, images acquired under UV illumination within an imaging system can be more consistent

due to the suppression of uneven background lighting. We therefore imaged each tube with a Kodak Gel Logic 200 imaging system equipped with Kodak molecular imaging software (Carestream Health, Rochester, NY) with a single exposure at 0.01 s exposure time.

5.4.8 Gel Electrophoresis.

Amplified UDG-LAMP products were analyzed via gel electrophoresis using a 2% agarose gel pre-stained with 1 GelStar (Lonza). Each sample consisted of 1 μL LAMP reaction product, 2 μL 10 bromophenol blue loading dye, and 7 μL 1 TBE. In parallel, each lane of ladder contains 1 μL low molecular weight DNA ladder, 2 μL loading dye, and 7 μL 1 TBE. Electrophoresis was performed in 1 TBE buffer at 140 V for 40 min. Gel images were taken with Kodak Gel Logic 200 imaging system.

5.4.9 Experimental Procedure of CORR-LAMP

Assembled reaction mix was pipette-loaded into MUA-passivated and DI-water-rinsed microfluidic chip. The chip fluid ports were sealed with PCR film (Microseal 'B' Adhesive Seals, Bio-Rad, Hercules, CA) to prevent reaction contamination and reagent evaporation. The chips were connected to a potentiostat (CHI 660D, CH Instruments, Austin, TX) for electrochemical measurements via custom card-edge connectors. After the 5-min UDG treatment step at room temperature, the chip was placed on a digital block heater (VWR International, Radnor, PA) maintained at 66 °C to perform the LAMP reaction. The thermal contact between the chip and the heater was established by a thermal compound (Arctic Alumina, Arctic Silver, Inc., Visalia, CA), which also served as an adhesive to keep chips attached to the heater during the reaction. We simultaneously initiated a series of time-course electrochemical measurements, measuring the redox current in each

chip every minute for 60 min. Up to six samples (two chips) could be tested in a single experiment.

5.4.10   Electrochemical Measurements

Square wave voltammetry (SWV) was selected for monitoring the MB redox current during LAMP reactions due to its fast measurement time (approximately 4 seconds per measurement). The SWV parameters were as followed: 0.2 V initial voltage, -0.4 V final voltage, 0.004 V increment, 0.025 V amplitude, 100 Hz frequency, 1 second quiet time and 100 nA sensitivity. A custom potentiostat macro command was written to enable the simultaneous monitoring of two chips (six samples).

5.4.11   Electrochemical Data Processing

The time-course current measurements were normalized to the current value at the end of the first minute of the LAMP reaction (i.e., $t = 1$ min). The normalized current trace was plotted and further processed with Origin 8.0 data analysis and graphing software (OriginLab, Northampton, MA). The normalized current trace was smoothed by the Origin built-in five-point adjacent averaging function. The derivative curve was subsequently calculated from the smoothed current trace using the Origin built-in derivative function. The derivative trace facilitated the reliable identification of the signal threshold —designated as the local minimum of the current derivative trace —and the corresponding time-to-threshold —defined as the reaction time required for a particular sample reaction to reach the signal threshold.

Appendix A

Supplementary Data for Closed-Loop Infusion Control
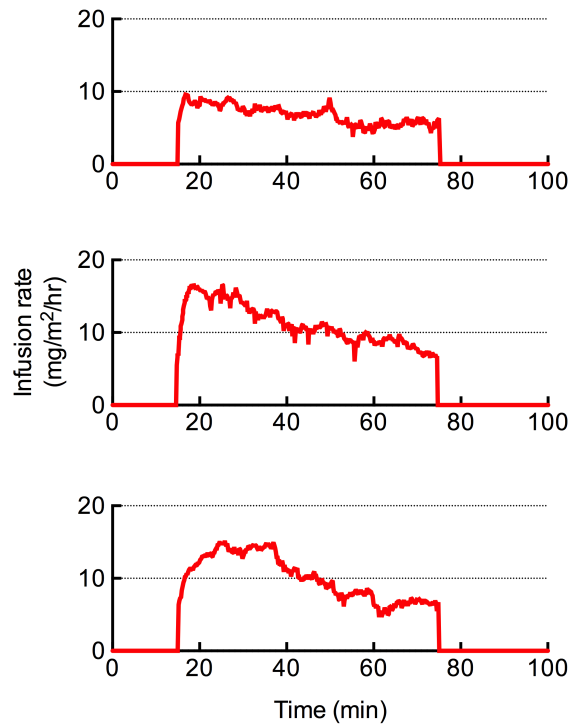
A.1 Pump output during controlled single-set-point targeting

Figure A.1: Infusion rate of DOX for three rabbits undergoing feedback-controlled infusion targeting an identical set-point (0.5 μM for 1 hr). These infusion profiles correspond to the control results shown for (top) Rabbit 2 in Figure 2.9B, (center) Rabbit 1 in Figure 2.9B, and (bottom) the right-hand plot for Rabbit 5 in Figure 2.10B.

Appendix B

Supplementary Data for

Shape-Based Sorting with FACS
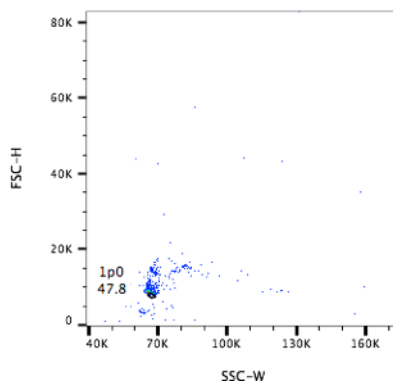
B.1   4-D Gates for particle sort
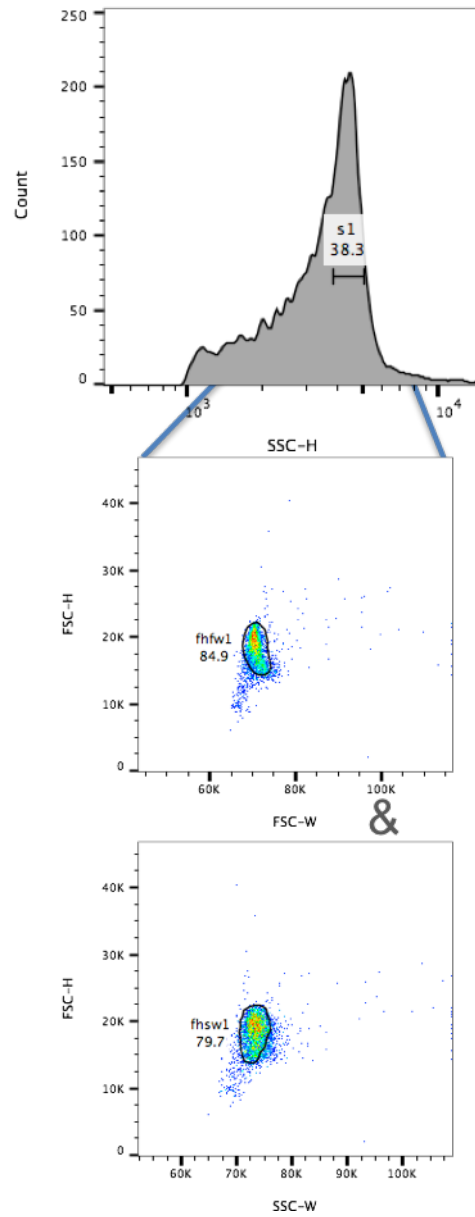

Figure B.1: 4-D gate AR 1.0
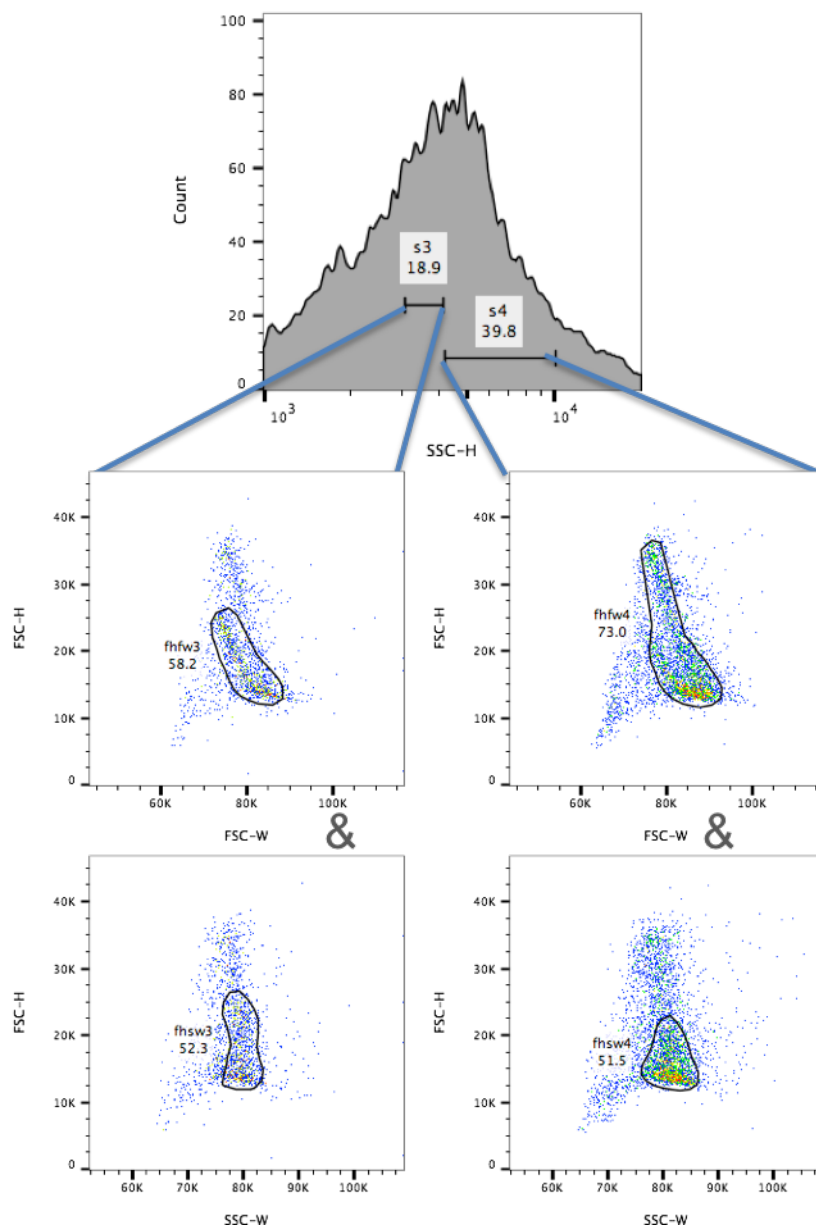
Figure B.2: 4-D gate AR 2.0
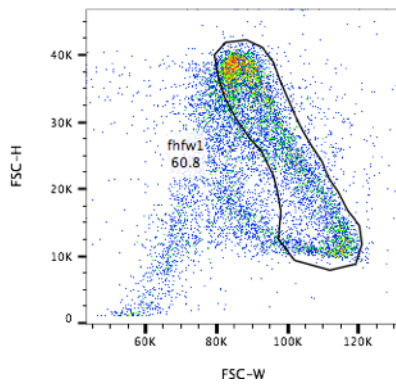
Figure B.3: 4-D gate AR 3.0

Figure B.4: 4-D gate AR 4.5

Bibliography

[1] Gao, B, Klumpen, H.-J, & Gurney, H. (2008) *Expert Opinion on Drug Metabolism & Toxicology* **4**, 1307–19.

[2] Undevia, S. D, Gomez-Abuin, G, & Ratain, M. J. (2005) *Nature Reviews. Cancer* **5**, 447–58.

[3] Mohammadpour, N, Elyasi, S, Vahdati, N, Mohammadpour, A. H, & Shamsara, J. (2011) *Iranian Journal of Basic Medical Sciences* **14**, 485–98.

[4] Gabardi, S, Martin, S. T, Roberts, K. L, & Grafals, M. (2011) *American Journal of Health-System Pharmacy* **68**, 211–218.

[5] Blix, H. S, Viktil, K. K, Moger, T. A, & Reikvam, A. (2010) *Pharmacy Practice* **8**, 50–5.

[6] Burns, M. (1999) *Journal of Thrombosis and Thrombolysis* **7**, 137–43.

[7] Scripture, C. D & Figg, W. D. (2006) *Nature Reviews. Cancer* **6**, 546–58.

[8] Ionescu, C & Caira, M. R. (2005) *Drug Metabolism: Current Concepts.* pp. 1–431.

[9] Baker, S. D, Verweij, J, Rowinsky, E. K, Donehower, R. C, Schellens, J. H. M, Grochow, L. B, & Sparreboom, A. (2002) *Journal of the National Cancer Institute* **94**, 1883–8.

[10] Khalil, F & Läer, S. (2011) *Journal of Biomedicine & Biotechnology* **2011**, 907461.

[11] Gurney, H. (2002) *British Journal of Cancer* **86**, 1297–302.

[12] Evans, W. E & Relling, M. V. (1999) *Science* **286**, 487–491.

[13] Wang, B, Canestaro, W. J, & Choudhry, N. K. (2014) *JAMA Internal Medicine* **174**, 1938–44.

[14] Zanger, U. M. (2010) *Frontiers in Pharmacology* **AUG**, 1–2.

[15] Kang, J. S & Lee, M. H. (2009) *The Korean Journal of Internal Medicine* **24**, 1–10.

[16] Ghiculescu, R. (2008) *Australian Prescriber* **31**, 42.

[17] Dumont, G. A & Ansermino, J. M. (2013) *Anesthesia and Analgesia* **117**, 1130–8.

[18] Hemmerling, T. M, Arbeid, E, Wehbe, M, Cyr, S, Taddei, R, & Zaouter, C. (2013) *British Journal of Anaesthesia* **110**, 1031–9.

[19] Absalom, A. R, De Keyser, R, & Struys, M. M. R. F. (2011) *Anesthesia and analgesia* **112**, 516–8.

[20] Uemura, K, Kamiya, A, Hidaka, I, Kawada, T, Shimizu, S, Shishido, T, Yoshizawa, M, Sugimachi, M, & Sunagawa, K. (2006) *Journal of Applied Physiology (Bethesda, Md. : 1985)* **100**, 1278–86.

[21] Uemura, K & Sugimachi, M. (2013) *Advanced Biomedical Engineering* **2**, 32–37.

[22] Mohamed E. Karar, Mohamed A. El-Brawany. (2011) *Biomedical Engineering and Computational Biology* **2011**, 1.

[23] Doyle, F. J, Huyett, L. M, Lee, J. B, Zisser, H. C, & Dassau, E. (2014) *Diabetes Care* **37**, 1191–7.

[24] Liu, Y, Li, M, Yang, D, Zhang, X, Wu, A, Yao, S, Xue, Z, & Yue, Y. (2015) *PLoS ONE* **10**, e0123862.

[25] El-Khatib, F. H, Russell, S. J, Nathan, D. M, Sutherlin, R. G, & Damiano, E. R. (2010) *Science Translational Medicine* **2**, 27ra27.

[26] Ferguson, B. S, Hoggarth, D. A, Maliniak, D, Ploense, K, White, R. J, Woodward, N, Hsieh, K, Bonham, A. J, Eisenstein, M, Kippin, T. E, Plaxco, K. W, & Soh, H. T. (2013) *Science Translational Medicine* **5**, 213ra165.

[27] Elis, A, Lishner, M, Walker, S, Atias, D, Korenberg, A, & Koren, G. (2010) *Therapeutic drug monitoring* **32**, 50–2.

[28] VON HOFF, D. D. (1979) *Annals of Internal Medicine* **91**, 710.

[29] Legha, S. S, Benjamin, R. S, Mackay, B, Ewer, M, Wallace, S, Valdivieso, M, Rasmussen, S. L, Blumenschein, G. R, & Freireich, E. J. (1982) *Annals of Internal Medicine* **96**, 133–9.

[30] Hortobagyi, G. N, Frye, D, Buzdar, A. U, Ewer, M. S, Fraschini, G, Hug, V, Ames, F, Montague, E, Carrasco, C. H, Mackay, B, & Benjamin, R. S. (1989) *Cancer* **63**, 37–45.

[31] van Dalen, E. C, van der Pal, H. J. H, Caron, H. N, & Kremer, L. C. (2009) *The Cochrane Database of Systematic Reviews* p. CD005008.

[32] Chatelut, E, White-Koning, M. L, Mathijssen, R. H, Puisset, F, Baker, S. D, & Sparreboom, A. (2012) *British journal of cancer* **107**, 1100–6.

[33] Eksborg, S, Strandler, H. S, Edsmyr, F, Näslund, I, & Tahvanainen, P. (1985) *European Journal of Clinical Pharmacology* **28**, 205–212.

[34] Dobbs, N. A, Twelves, C. J, Gillies, H, James, C. A, Harper, P. G, & Rubens, R. D. (1995) *Cancer chemotherapy and pharmacology* **36**, 473–6.

[35] Barpe, D. R, Rosa, D. D, & Froehlich, P. E. (2010) *European Journal of Pharmaceutical Sciences : official journal of the European Federation for Pharmaceutical Sciences* **41**, 458–63.

[36] Budman, D. R, Berry, D. A, Cirrincione, C. T, Henderson, I. C, Wood, W. C, Weiss, R. B, Ferree, C. R, Muss, H. B, Green, M. R, Norton, L, & Frei, E. (1998) *JNCI Journal of the National Cancer Institute* **90**, 1205–1211.

[37] Plaxco, K. W & Soh, H. T. (2011) *Trends in biotechnology* **29**, 1–5.

[38] White, R. J & Plaxco, K. W. (2010) *Analytical chemistry* **82**, 73–6.

[39] Xiao, Y, Lubin, A. A, Heeger, A. J, & Plaxco, K. W. (2005) *Angewandte Chemie (International ed. in English)* **44**, 5456–9.

[40] Swensen, J. S, Xiao, Y, Ferguson, B. S, Lubin, A. A, Lai, R. Y, Heeger, A. J, Plaxco, K. W, & Soh, H. T. (2009) *Journal of the American Chemical Society* **131**, 4262–6.

[41] Rowe, A. A, Miller, E. A, & Plaxco, K. W. (2010) *Analytical chemistry* **82**, 7090–5.

[42] Wochner, A, Menger, M, Orgel, D, Cech, B, Rimmele, M, Erdmann, V. A, & Glökler, J. (2008) *Analytical biochemistry* **373**, 34–42.

[43] Greene, R. F, Collins, J. M, Jenkins, J. F, Speyer, J. L, & Myers, C. E. (1983) *Cancer research* **43**, 3417–21.

[44] Joon Bok Lee, Dassau, E, Seborg, D, & Doyle, F. (2013) Model-based personalization scheme of an artificial pancreas for Type 1 diabetes applications.

[45] Maniez-Devos, D. M, Baurain, R, Trouet, A, & Lesne, M. (1985) *Journal de pharmacologie* **16**, 159–69.

[46] Camaggi, C. M, Comparsi, R, Strocchi, E, Testoni, F, Angelelli, B, & Pannuti, F. (1988) *Cancer Chemotherapy and Pharmacology* **21**, 221–8.

[47] Rahman, A, Carmichael, D, Harris, M, & Roh, J. K. (1986) *Cancer research* **46**, 2295–9.

[48] Ueda, Y, Munechika, K, Kikukawa, A, Kanoh, Y, Yamanouchi, K, & Yokoyama, K. (1989) *Chemical & pharmaceutical bulletin* **37**, 1639–41.

[49] Barrett, R. J, Blessing, J. A, Homesley, H. D, Twiggs, L, & Webster, K. D. (1993) *American Journal of Clinical Oncology* **16**, 494–6.

[50] Najjar, T. A. O & Saad, S. Y. (2000) *Journal of the Egyptian Nat. Cancer Inst.* **12**, 259–265.

[51] Anderson, J. A. (1988) *Anesthesia Progress* **35**, 43–47.

[52] Nitzki-George, D, Wozniak, I, & Caprini, J. A. (2013) *The Annals of Pharmacotherapy* **47**, 841–55.

[53] Phares, N, White, R. J, & Plaxco, K. W. (2009) *Analytical Chemistry* **81**, 1095–100.

[54] Kanto, J & Gepts, E. (1989) *Clinical Pharmacokinetics* **17**, 308–26.

[55] Ho, J. S, Yeh, A. J, Neofytou, E, Kim, S, Tanabe, Y, Patlolla, B, Beygui, R. E, & Poon, A. S. Y. (2014) *Proceedings of the National Academy of Sciences of the United States of America* **111**, 7974–9.

[56] Farra, R, Sheppard, N. F, McCabe, L, Neer, R. M, Anderson, J. M, Santini, J. T, Cima, M. J, & Langer, R. (2012) *Science Translational Medicine* **4**, 122ra21.

[57] Thorslund, S, Sanchez, J, Larsson, R, Nikolajeff, F, & Bergquist, J. (2005) *Colloids and Surfaces. B, Biointerfaces* **45**, 76–81.

[58] Thorslund, S, Sanchez, J, Larsson, R, Nikolajeff, F, & Bergquist, J. (2005) *Colloids and Surfaces. B, Biointerfaces* **46**, 240–7.

[59] Herbert, J. M, Dol, F, Bernat, A, Falotico, R, Lalé, A, & Savi, P. (1998) *Thrombosis and Haemostasis* **80**, 512–8.

[60] Zehnder, A. M, Hawkins, M. G, Trestrail, E. A, Holt, R. W, & Kent, M. S. (2012) *American Journal of Veterinary Research* **73**, 1859–63.

[61] Campos, E, Branquinho, J, Carreira, A. S, Carvalho, A, Coimbra, P, Ferreira, P, & Gil, M. (2013) *European Polymer Journal* **49**, 2005–2021.

[62] Champion, J. A, Katare, Y. K, & Mitragotri, S. (2007) *Proceedings of the National Academy of Sciences of the United States of America* **104**, 11901–4.

[63] Mitragotri, S & Lahann, J. (2009) *Nature Materials* **8**, 15–23.

[64] Mitragotri, S, Burke, P. A, & Langer, R. (2014) *Nature Reviews Drug Discovery* **13**, 655–672.

[65] Chen, H. H, Le Visage, C, Qiu, B, Du, X, Ouwerkerk, R, Leong, K. W, & Yang, X. (2005) *Magnetic Resonance in Medicine* **53**, 614–20.

[66] Subramanian, G, Manoharan, V. N, Thorne, J. D, & Pine, D. J. (1999) *Advanced Materials* **11**, 1261–1265.

[67] Yin, Y & Xia, Y. (2001) *Advanced Materials* **13**, 267–271.

[68] Conrad, J. C, Ferreira, S. R, Yoshikawa, J, Shepherd, R. F, Ahn, B. Y, & Lewis, J. A. (2011) *Current Opinion in Colloid & Interface Science* **16**, 71–79.

[69] Phillips, C. L, Jankowski, E, Krishnatreya, B. J, Edmond, K. V, Sacanna, S, Grier, D. G, Pine, D. J, & Glotzer, S. C. (2014) *Soft Matter* **10**, 7468–79.

[70] Kong, T, Wu, J, To, M, Wai Kwok Yeung, K, Cheung Shum, H, & Wang, L. (2012) *Biomicrofluidics* **6**, 34104.

[71] Dendukuri, D & Doyle, P. S. (2009) *Advanced Materials* **21**, 4071–4086.

[72] Xu, Q, Hashimoto, M, Dang, T. T, Hoare, T, Kohane, D. S, Whitesides, G. M, Langer, R, Anderson, D. G, & David, H. (2009) *Small* **5**, 1575–1581.

[73] Min, N. G, Kim, B, Lee, T. Y, Kim, D, Lee, D. C, & Kim, S.-H. (2015) *Langmuir* **31**, 937–943.

[74] Dendukuri, D, Pregibon, D. C, Collins, J, Hatton, T. A, & Doyle, P. S. (2006) *Nature Materials* **5**, 365–369.

[75] Wu, C.-Y, Owsley, K, & Di Carlo, D. (2015) *Advanced Materials* pp. n/a–n/a.

[76] Bhaskar, S, Pollock, K. M, Yoshida, M, & Lahann, J. (2010) *Small (Weinheim an der Bergstrasse, Germany)* **6**, 404–11.

[77] Matijevic, E. (1993) *Chemistry of Materials* **5**, 412–426.

[78] Sansdrap, P & Moës, A. (1993) *International Journal of Pharmaceutics* **98**, 157–164.

[79] Manoharan, V. N, Elsesser, M. T, & Pine, D. J. (2003) *Science (New York, N.Y.)* **301**, 483–7.

[80] Kowalczyk, B, Lagzi, I, & Grzybowski, B. a. (2011) *Current Opinion in Colloid and Interface Science* **16**, 135–148.

[81] Sharma, V, Park, K, & Srinivasarao, M. (2009) *Proceedings of the National Academy of Sciences of the United States of America* **106**, 4981–5.

[82] Akbulut, O, MacE, C. R, Martinez, R. V, Kumar, A. a, Nie, Z, Patton, M. R, & Whitesides, G. M. (2012) *Nano Letters* **12**, 4060–4064.

[83] Hanauer, M, Pierrat, S, Zins, I, Lotz, A, & Sönnichsen, C. (2007) *Nano Letters* **7**, 2881–5.

[84] Sugaya, S, Yamada, M, & Seki, M. (2011) *Biomicrofluidics* **5**, 024103.

[85] Ranjan, S, Zeming, K. K, Jureen, R, Fisher, D, & Zhang, Y. (2014) *Lab on a Chip* **14**, 4250–62.

[86] Dubose, J, Lu, X, Patel, S, Qian, S, Woo Joo, S, & Xuan, X. (2014) *Biomicrofluidics* **8**, 014101.

[87] Masaeli, M, Sollier, E, Amini, H, Mao, W, Camacho, K, Doshi, N, Mitragotri, S, Alexeev, A, & Di Carlo, D. (2012) *Physical Review X* **2**, 031017.

[88] Black, D. L, McQuay, M. Q, & Bonin, M. P. (1996) *Progress in Energy and Combustion Science* **22**, 267–306.

[89] Kaye, P. H. (1998) *Measurement Science and Technology* **9**, 141–149.

[90] Jones, a. R. (1999) *Progress in Energy and Combustion Science* **25**, 1–53.

[91] Hoffman, R. A. (2008) *Springer Series Fluorescence* pp. 307–342.

[92] Salzman, G. C, Wilder, M. E, & Jett, J. H. (1979) *Journal of Histochemistry & Cytochemistry* **27**, 264–7.

[93] Sloot, P. M, Hoekstra, A. G, van der Liet, H, & Figdor, C. G. (1989) *Applied optics* **28**, 1752–62.

[94] Kerker, M. (1983) *Cytometry* **4**, 1–10.

[95] Benson, M. C, McDougal, D. C, & Coffey, D. S. (1984) *Cytometry* **5**, 515–22.

[96] Sloot, P. M. A & Figdor, C. G. (1986) *Applied Optics* **25**, 3559.

[97] Boll, B, Folzer, E, Finkler, C, Huwyler, J, Mahler, H.-C, Schmidt, R, & Koulov, A. V. (2015) *Pharmaceutical Research* **32**, 3952–3964.

[98] van der Pol, E, Coumans, F, Varga, Z, Krumrey, M, & Nieuwland, R. (2013) *Journal of Thrombosis and Haemostasis* **11**, 36–45.

[99] van der Pol, E, Coumans, F. a. W, Grootemaat, a. E, Gardiner, C, Sargent, I. L, Harrison, P, Sturk, a, van Leeuwen, T. G, & Nieuwland, R. (2014) *Journal of Thrombosis and Haemostasis* **12**, 1182–1192.

[100] Varga, Z, Yuana, Y, Grootemaat, A. E, van der Pol, E, Gollwitzer, C, Krumrey, M, & Nieuwland, R. (2014) *Journal of Extracellular Vesicles* **3**, 1–10.

[101] Kinnunen, M & Karmenyan, A. (2015) *Journal of Biomedical Optics* **20**, 051040.

[102] Hoffman, R. A. (2009) *Current Protocols in Cytometry* pp. 1–17.

[103] Sharpless, T. K & Melamed, M. R. (1976) *Journal of Histochemistry & Cytochemistry* **24**, 257–64.

[104] Sharpless, T. K, Bartholdi, M, & Melamed, M. R. (1977) *Journal of Histochemistry & Cytochemistry* **25**, 845–856.

[105] Leary, J. F, Todd, P, Wood, J. C, & Jett, J. H. (1979) *Journal of Histochemistry & Cytochemistry* **27**, 315–320.

[106] Hammond, T. G, Majewski, R. R, Morré, D. J, Schell, K, & Morrissey, L. W. (1993) *Cytometry* **14**, 411–20.

[107] Hammond, T. G, Morré, D. J, Harris, H. W, & Zeidel, M. L. (1993) *Biochemical Journal* **295**, 471–476.

[108] Manogaran, P. S, Kausalya, S, & Pande, G. (1995) *Cytometry* **19**, 320–5.

[109] Chioccioli, M, Hankamer, B, & Ross, I. L. (2014) *PLoS ONE* **9**, e97269.

[110] Shapiro, H. M. (2005) *Practical Flow Cytometry.* (John Wiley & Sons), p. 736.

[111] Terstappen, L. W, de Grooth, B. G, Visscher, K, van Kouterik, F. A, & Greve, J. (1988) *Cytometry* **9**, 39–43.

[112] Terstappen, L. W, Mickaels, R. A, Dost, R, & Loken, M. R. (1990) *Cytometry* **11**, 506–12.

[113] Tzur, A, Moore, J. K, Jorgensen, P, Shapiro, H. M, & Kirschner, M. W. (2011) *PLoS ONE* **6**, e16053.

[114] Watson, D, Hagen, N, Diver, J, Marchand, P, & Chachisvilis, M. (2004) *Biophysical Journal* **87**, 1298–1306.

[115] Umhauer, H & Bottlinger, M. (1991) *Applied Optics* **30**, 4980–4986.

[116] Leary, J. F & Todd, P. (1981) Pulse edge measurement for determining particle dimensional characteristics.

[117] Salzman, G. C, Crowell, J. M, Martin, J. C, Trujillo, T. T, Romero, A, Mullaney, P. F, & LaBauve, P. M. (1975) *Acta cytologica* **19**, 374–7.

[118] Bohren, C. F & Huffman, D. R. (1983) *Absorption and Scattering of Light by Small Particles.* (John Wiley & Sons, New York).

[119] Latimer, P, Brunsting, A, Pyle, B. E, & Moore, C. (1978) *Applied Optics* **17**, 3152–8.

[120] Waterman, P. (1965) *Proceedings of the IEEE* **53**, 805–812.

[121] Farafonov, V. G. (2000) *Physical and Quantum Optics* **88**, 70–77.

[122] Schneider, J & Peden, I. (1988) *IEEE Transactions on Antennas and Propagation* **36**, 1317–1321.

[123] Mishchenko, M. I, Travis, L. D, & Mackowski, D. W. (1996) *Journal of Quantitative Spectroscopy and Radiative Transfer* **55**, 535–575.

[124] Nousiainen, T & Vermeulen, K. (2003) *Journal of Quantitative Spectroscopy and Radiative Transfer* **79-80**, 1031–1042.

[125] Melamed, M. R, Lindmo, T, & Mendelsohn, M. L. (1990) *Flow Cytometry and Sorting.* (Wiley-Liss, New York), Second edition.

[126] Loken, M. R, Parks, D. R, & Herzenberg, L. A. (1977) *Journal of Histochemistry & Cytochemistry* **25**, 790–795.

[127] Bloch, D, Beaty, N, Fu, C. T, Chin, E, Smith, J, & Pipkin, J. L. (1978) *Journal of Histochemistry & Cytochemistry* **26**, 170–186.

[128] Mishchenko, M. I. (2000) *Applied Optics* **39**, 1026.

[129] Leinonen, J. (2014) *Optics Express* **22**, 1655–60.

[130] Mishchenko, M. I & Travis, L. D. (1998) *Journal of Quantitative Spectroscopy and Radiative Transfer* **60**, 309–324.

[131] Lo, K, Hahne, F, Brinkman, R. R, & Gottardo, R. (2009) *BMC Bioinformatics* **10**, 145.

[132] Pyne, S, Hu, X, Wang, K, Rossin, E, Lin, T.-I, Maier, L. M, Baecher-Allan, C, McLachlan, G. J, Tamayo, P, Hafler, D. A, De Jager, P. L, & Mesirov, J. P. (2009) *Proceedings of the National Academy of Sciences* **106**, 8519–8524.

[133] Qian, Y, Wei, C, Eun-Hyung Lee, F, Campbell, J, Halliley, J, Lee, J. A, Cai, J, Kong, Y. M, Sadat, E, Thomson, E, Dunn, P, Seegmiller, A. C, Karandikar, N. J, Tipton, C. M, Mosmann, T, Sanz, I, & Scheuermann, R. H. (2010) *Cytometry. Part B, Clinical cytometry* **78 Suppl 1**, S69–82.

[134] Zare, H, Shooshtari, P, Gupta, A, & Brinkman, R. R. (2010) *BMC Bioinformatics* **11**, 403.

[135] Costa, E. S, Pedreira, C. E, Barrena, S, Lecrevisse, Q, Flores, J, Quijano, S, Almeida, J, del Carmen García- Macias, M, Bottcher, S, Van Dongen, J. J. M, & Orfao, A. (2010) *Leukemia* **24**, 1927–1933.

[136] Qiu, P, Simonds, E. F, Bendall, S. C, Gibbs, K. D, Bruggner, R. V, Linderman, M. D, Sachs, K, Nolan, G. P, & Plevritis, S. K. (2011) *Nature Biotechnology* **29**, 886–891.

[137] Aghaeepour, N, Nikolic, R, Hoos, H. H, & Brinkman, R. R. (2011) *Cytometry Part A* **79A**, 6–13.

[138] Lee, G. (2011).

[139] Ge, Y & Sealfon, S. C. (2012) *Bioinformatics (Oxford, England)* **28**, 2052–8.

[140] Aghaeepour, N, Chattopadhyay, P. K, Ganesan, A, O'Neill, K, Zare, H, Jalali, A, Hoos, H. H, Roederer, M, & Brinkman, R. R. (2012) *Bioinformatics (Oxford, England)* **28**, 1009–16.

[141] Aghaeepour, N, Jalali, A, O'Neill, K, Chattopadhyay, P. K, Roederer, M, Hoos, H. H, & Brinkman, R. R. (2012) *Cytometry. Part A : the journal of the International Society for Analytical Cytology* **81**, 1022–30.

[142] Simon, S, Guthke, R, Kamradt, T, & Frey, O. (2012) *Frontiers in Microbiology* **3**.

[143] Barber, P & Yeh, C. (1975) *Applied Optics* **14**, 2864–72.

[144] Wriedt, T. (2002) *Particle & Particle Systems Characterization* **19**, 256–268.

[145] Mätzler, C. (2002) MATLAB Functions for Mie Scattering and Absorption. IAP Research Report, Technical Report No. 2002-11.

[146] Xie, Y. X. Y & Ji, Q. J. Q. (2002) *Proceedings. 16th International Conference on Pattern Recognition, 2002.* **2**, 957 – 960.

[147] Blasi, T, Hennig, H, Summers, H. D, Theis, F. J, Cerveira, J, Patterson, J. O, Davies, D, Filby, A, Carpenter, A. E, & Rees, P. (2016) *Nature Communications* **7**, 10256.

[148] McKenna, B. K, Evans, J. G, Cheung, M. C, & Ehrlich, D. J. (2011) *Nature methods* **8**, 401–3.

[149] George, T. C, Fanning, S. L, Fitzgerald-Bocarsly, P, Fitzgeral-Bocarsly, P, Medeiros, R. B, Highfill, S, Shimizu, Y, Hall, B. E, Frost, K, Basiji, D, Ortyn, W. E, Morrissey, P. J, & Lynch, D. H. (2006) *Journal of immunological methods* **311**, 117–29.

[150] Friend, S, Venkatachalam, V, George, T. C, Hall, B. E, & Morrissey, P. J. (2007) *The Journal of Immunology* **178**, S246.

[151] Boutros, M, Heigwer, F, & Laufer, C. (2015) *Cell* **163**, 1314–1325.

[152] Basiji, D. A, Ortyn, W. E, Liang, L, Venkatachalam, V, & Morrissey, P. (2007) *Clinics in laboratory medicine* **27**, 653–70, viii.

[153] Basiji, D & Ortyn, W. E. (2001) Patent US6249341 - Imaging and analyzing parameters of small moving objects such as cells.

[154] Hayashi, M, Hattori, A, Kim, H, Terazono, H, Kaneko, T, & Yasuda, K. (2011) *International Journal of Molecular Sciences* **12**, 3618–34.

[155] Zang, E, Brandes, S, Tovar, M, Martin, K, Mech, F, Horbert, P, Henkel, T, Figge, M. T, & Roth, M. (2013) *Lab on a Chip* **13**, 3707–13.

[156] Rajauria, S, Axline, C, Gottstein, C, & Cleland, A. N. (2014) *Nano Letters* **15**, 469–475.

[157] Wang, X, Chen, S, Kong, M, Wang, Z, Costa, K. D, Li, R. A, & Sun, D. (2011) *Lab on a Chip* **11**, 3656–62.

[158] Otto, O, Rosendahl, P, Mietke, A, Golfier, S, Herold, C, Klaue, D, Girardo, S, Pagliara, S, Ekpenyong, A, Jacobi, A, Wobus, M, Töpfner, N, Keyser, U. F, Mansfeld, J, Fischer-Friedrich, E, & Guck, J. (2015) *Nature Methods* **12**, 199–202, 4 p following 202.

[159] Oh, K. W, Lee, K, Ahn, B, & Furlani, E. P. (2012) *Lab Chip* **12**, 515–545.

[160] Cornish, R. J. (1928) *Proceedings of the Royal Society A: Mathematical, Physical and Engineering Sciences* **120**, 691–700.

[161] Shields, C. W, Reyes, C. D, & López, G. P. (2015) *Lab on a chip* **15**, 1230–49.

[162] Pethig, R. (2010) *Biomicrofluidics* **4**.

[163] Sun, T, Holmes, D, Gawad, S, Green, N. G, & Morgan, H. (2007) *Lab on a chip* **7**, 1034–40.

[164] Ahn, K, Kerbage, C, Hunt, T. P, Westervelt, R. M, Link, D. R, & Weitz, D. a. (2006) *Applied Physics Letters* **88**, 024104.

[165] Baret, J.-C, Miller, O. J, Taly, V, Ryckelynck, M, El-Harrak, A, Frenz, L, Rick, C, Samuels, M. L, Hutchison, J. B, Agresti, J. J, Link, D. R, Weitz, D. a, & Griffiths, A. D. (2009) *Lab on a chip* **9**, 1850–8.

[166] Fiedler, S, Shirley, S. G, Schnelle, T, & Fuhr, G. (1998) *Analytical Chemistry* **70**, 1909–1915.

[167] Gagnon, Z. R. (2011) *Electrophoresis* **32**, 2466–87.

[168] Khoshmanesh, K, Nahavandi, S, Baratchi, S, Mitchell, A, & Kalantar-zadeh, K. (2011) *Biosensors & bioelectronics* **26**, 1800–14.

[169] Yun, H, Kim, K, & Lee, W. G. (2014) *Biomicrofluidics* **8**, 066501.

[170] Sajeesh, P, Manasi, S, Doble, M, & Sen, A. K. (2015) *Lab on a chip* **15**, 3738–48.

[171] Park, S, Zhang, Y, Wang, T.-H, & Yang, S. (2011) *Lab on a chip* **11**, 2893–900.

[172] Weng, P.-Y, Chen, I.-A, Yeh, C.-K, Chen, P.-Y, & Juang, J.-Y. (2016) *Biomicrofluidics* **10**, 011909.

[173] Mittal, N, Rosenthal, A, & Voldman, J. (2007) *Lab on a chip* **7**, 1146–53.

[174] Ballard, D. (1981) *Pattern Recognition* **13**, 111–122.

[175] Fitzgibbon, A. W & Fisher, R. B. (1995) *A buyer's guide to conic fitting.* (BMVA Press), pp. 513–522.

[176] Buchholz, D. E, Hikita, S. T, Rowland, T. J, Friedrich, A. M, Hinman, C. R, Johnson, L. V, & Clegg, D. O. (2009) *Stem cells (Dayton, Ohio)* **27**, 2427–34.

[177] Rowland, T. J, Buchholz, D. E, & Clegg, D. O. (2012) *Journal of cellular physiology* **227**, 457–66.

[178] Tse, H. T. K, Meng, P, Gossett, D. R, Irturk, A, Kastner, R, & Di Carlo, D. (2011) *Journal of laboratory automation* **16**, 422–30.

[179] Franke, T, Braunmüller, S, Schmid, L, Wixforth, A, & Weitz, D. A. (2010) *Lab on a chip* **10**, 789–94.

[180] Ren, L, Chen, Y, Li, P, Mao, Z, Huang, P.-H, Rufo, J, Guo, F, Wang, L, McCoy, J. P, Levine, S. J, & Huang, T. J. (2015) *Lab on a Chip.*

[181] Schonbrun, E, Gorthi, S. S, & Schaak, D. (2012) *Lab on a chip* **12**, 268–73.

[182] Goda, K, Ayazi, A, Gossett, D. R, Sadasivam, J, Lonappan, C. K, Sollier, E, Fard, A. M, Hur, S. C, Adam, J, Murray, C, Wang, C, Brackbill, N, Di Carlo, D, & Jalali, B. (2012) *Proceedings of the National Academy of Sciences of the United States of America* **109**, 11630–5.

[183] Yang, S & Rothman, R. E. (2004) *The Lancet. Infectious diseases* **4**, 337–48.

[184] Ivnitski, D, O'Neil, D. J, Gattuso, A, Schlicht, R, Calidonna, M, & Fisher, R. (2003) *BioTechniques* **35**, 862–9.

[185] Niemz, A, Ferguson, T. M, & Boyle, D. S. (2011) *Trends in Biotechnology* **29**, 240–50.

[186] Elmerdahl Olsen, J. (2000) *Food Research International* **33**, 257–266.

[187] Malorny, B, Tassios, P. T, Rådström, P, Cook, N, Wagner, M, & Hoorfar, J. (2003) *International Journal of Food Microbiology* **83**, 39–48.

[188] McKillip, J. L & Drake, M. (2004) *Journal of Food Protection* **67**, 823–32.

[189] Toze, S. (1999) *Water Research* **33**, 3545–3556.

[190] Call, D. R, Borucki, M. K, & Loge, F. J. (2003) *Journal of Microbiological Methods* **53**, 235–243.

[191] Notomi, T. (2000) *Nucleic Acids Research* **28**, 63e–63.

[192] Nagamine, K, Watanabe, K, Ohtsuka, K, Hase, T, & Notomi, T. (2001) *Clinical Chemistry* **47**, 1742–3.

[193] Tomita, N, Mori, Y, Kanda, H, & Notomi, T. (2008) *Nature Protocols* **3**, 877–82.

[194] Borst, A, Box, A. T. A, & Fluit, A. C. (2004) *European Journal of Clinical Microbiology & Infectious Diseases : official publication of the European Society of Clinical Microbiology* **23**, 289–99.

[195] Aslanzadeh, J. (2004) *Annals of Clinical and Laboratory Science* **34**, 389–96.

[196] Longo, M. C, Berninger, M. S, & Hartley, J. L. (1990) *Gene* **93**, 125–128.

[197] Lindahl, T. (1974) *Proceedings of the National Academy of Sciences* **71**, 3649–3653.

[198] Lindahl, T, Ljungquist, S, Siegert, W, Nyberg, B, & Sperens, B. (1977) *J. Biol. Chem.* **252**, 3286–3294.

[199] He, L, Xu, H.-S, Wang, M.-Z, & Rong, H.-N. (2010) *Bing du xue bao = Chinese journal of virology / [bian ji, Bing du xue bao bian ji wei yuan hui]* **26**, 490–5.

[200] He, L & Xu, H.-s. (2011) *Aquaculture* **311**, 94–99.

[201] Tanner, N. A, Zhang, Y, & Evans, T. C. (2012) *BioTechniques* **53**, 81–9.

[202] Lanes, O, Guddal, P. H, Gjellesvik, D. R, & Willassen, N. P. (2000) *Comparative Biochemistry and Physiology Part B: Biochemistry and Molecular Biology* **127**, 399–410.

[203] Leiros, I, Moe, E, Lanes, O, Smalås, A. O, & Willassen, N. P. (2003) *Acta Crystallographica Section D Biological Crystallography* **59**, 1357–1365.

[204] Lhomme, J, Constant, J. F, & Demeunynck, M. (1999) *Biopolymers* **52**, 65–83.

[205] Sugiyama, H, Fujiwara, T, Ura, A, Tashiro, T, Yamamoto, K, Kawanishi, S, & Saito, I. (1994) *Chemical Research in Toxicology* **7**, 673–683.

[206] Hara-Kudo, Y, Yoshino, M, Kojima, T, & Ikedo, M. (2005) *FEMS Microbiology Letters* **253**, 155–61.

[207] Stafford, R. G & Ettinger, H. J. (1972) *Atmospheric Environment (1967)* **6**, 353–362.

[208] Wang, H.-C & Kasper, G. (1991) *Journal of Aerosol Science* **22**, 31–41.

[209] Mori, Y, Kitao, M, Tomita, N, & Notomi, T. (2004) *Journal of biochemical and biophysical methods* **59**, 145–57.

[210] Fang, X, Liu, Y, Kong, J, & Jiang, X. (2010) *Analytical chemistry* **82**, 3002–6.

[211] Fang, X, Chen, H, Yu, S, Jiang, X, & Kong, J. (2011) *Analytical chemistry* **83**, 690–5.

[212] Gandelman, O. A, Church, V. L, Moore, C. A, Kiddle, G, Carne, C. A, Parmar, S, Jalal, H, Tisi, L. C, & Murray, J. A. H. (2010) *PloS one* **5**, e14155.

[213] Lucchi, N. W, Demas, A, Narayanan, J, Sumari, D, Kabanywanyi, A, Kachur, S. P, Barnwell, J. W, & Udhayakumar, V. (2010) *PloS one* **5**, e13733.

[214] Ahmad, F, Seyrig, G, Tourlousse, D. M, Stedtfeld, R. D, Tiedje, J. M, & Hashsham, S. A. (2011) *Biomedical Microdevices* **13**, 929–937.

[215] Zhang, X, Lowe, S. B, & Gooding, J. J. (2014) *Biosensors & bioelectronics* **61**, 491–9.

[216] Patterson, A. S, Hsieh, K, Soh, H. T, & Plaxco, K. W. (2013) *Trends in biotechnology* **31**, 704–12.

[217] Nagatani, N, Yamanaka, K, Saito, M, Koketsu, R, Sasaki, T, Ikuta, K, Miyahara, T, & Tamiya, E. (2011) *The Analyst* **136**, 5143–50.

[218] Hsieh, K, Patterson, A. S, Ferguson, B. S, Plaxco, K. W, & Soh, H. T. (2012) *Angewandte Chemie (International ed. in English)* **51**, 4896–900.

[219] Jiang, D, Xiang, G, Liu, C, Yu, J, Liu, L, & Pu, X. (2012) *International Journal of Electrochemical Science* **7**, 10607–10619.

[220] Ahmed, M. U, Nahar, S, Safavieh, M, & Zourob, M. (2013) *The Analyst* **138**, 907–15.

[221] Safavieh, M, Ahmed, M. U, Ng, A, & Zourob, M. (2014) *Biosensors & bioelectronics* **58**, 101–6.

[222] Luo, J, Fang, X, Ye, D, Li, H, Chen, H, Zhang, S, & Kong, J. (2014) *Biosensors & bioelectronics* **60**, 84–91.

[223] Sagara, T, Kawamura, H, & Nakashima, N. (1996) *Langmuir* **12**, 4253–4259.

[224] Bain, C. D, Troughton, E. B, Tao, Y. T, Evall, J, Whitesides, G. M, & Nuzzo, R. G. (1989) *Journal of the American Chemical Society* **111**, 321–335.

[225] Lai, R. Y, Seferos, D. S, Heeger, A. J, Bazan, G. C, & Plaxco, K. W. (2006) *Langmuir : the ACS journal of surfaces and colloids* **22**, 10796–800.

[226] Ortiz, M, Fragoso, A, Ortiz, P. J, & O'Sullivan, C. K. (2011) *Journal of Photochemistry and Photobiology A: Chemistry* **218**, 26–32.

[227] Pan, D, Zuo, X, Wan, Y, Wang, L, Zhang, J, Song, S, & Fan, C. (2007) *Sensors* **7**, 2671–2680.

[228] Yang, W, Ozsoz, M, Hibbert, D, & Gooding, J. (2002) *Electroanalysis* **14**, 1299–1302.

[229] Grumelli, D, Méndez De Leo, L. P, Bonazzola, C, Zamlynny, V, Calvo, E. J, & Salvarezza, R. C. (2010) *Langmuir : the ACS journal of surfaces and colloids* **26**, 8226–32.